Investigating Adhesion and Degradation of Polymer Materials for Industrial Applications

by

Shuqing Zhang

A dissertation submitted in partial fulfillment
of the requirements for the degree of
Doctor of Philosophy
(Macromolecular Science and Engineering)
in the University of Michigan
2024

Doctoral Committee:

Professor Zhan Chen, Chair
Professor Adam J. Matzger
Professor Charles C. L. McCrory
Professor Anne J. McNeil

Shuqing Zhang

zhangsq@umich.edu

ORCID iD: 0000-0001-8379-355X

© Shuqing Zhang 2024

Dedication

To my family and friends.

Acknowledgements

In my doctoral journey over the past few years, I have gained valuable experience and achieved significant personal growth. I recognize that none of this would have been possible without the help of those around me. I am very grateful as their support has been indispensable in guiding me to where I am today.

First, I extend my deepest gratitude to my supervisor, Prof. Zhan Chen. I feel fortunate to have been able to conduct research in Chen Lab, where I can pursue my passion for applying scientific methods to address real-world challenges in polymer applications. Prof. Chen guided me towards a deeper understanding of this field, fostering my skills in data analysis and problem solving. He helped me develop the ability to think independently while also teaching me how to collaborate effectively within a team. His consistent support has provided me with numerous opportunities for personal and professional development, such as learning to deliver reports efficiently at industry meetings and present fluently at conferences. I am both delighted and thankful to have spent these years under his mentorship.

I appreciate Prof. Matzger, Prof. McNeil, and Prof. McCrory for serving on my committee in the past years. Prof. Matzger's Macromolecules course was enlightening and memorable for his adeptness at simplifying complex concepts and his thorough preparation of sample demonstrations. During several doctoral meetings, he provided numerous valuable questions and suggestions, and I am grateful to have him on my committee. Similarly, I first encountered Prof. McCrory in his Materials Chemistry course. I still remember I reached out to him before the first

class when I was waitlisted, and his caring approach and willingness to help students left a lasting impression on me. I appreciate his willingness to serve on my committee and for his assistance throughout the years. I have actively joined Huron River cleanups, organized by Prof. McNeil over the past years, finding them truly inspiring. Prof. McNeil's commitment to environmental awareness and her expertise in plastics recycling have offered valuable insights for my research on plastic degradation. I am truly thankful for her help.

I would like to thank the mentorship and support of my lab fellow colleagues. When I first joined the group as a novice, Dr. Bolin Li patiently taught me numerous experimental skills and provided guidance. Dr. John Andre warmly acquainted me with the laboratory and offered guidance on my projects from day one. Dr. Chengcheng Zhang helped me understand various research directions when I first arrived. Besides, over the past few years, many people in the group have worked alongside me, and I am grateful for their collaboration and support. I extend my gratitude to Najae Escoffery, Fernando Gomez, Jayani Mawela, Glad Labrague, Dr. Ting Lin, and Dr. Daniel Rossi for the collaborations. I also appreciate the support from Dr. Wen Guo, Dr. Tieyi Lu, Dr. Ralph Crisci, Yuchen Wu, Tianle Wang, Zahra Gandhi, Jinpeng Gao, Xuhong Chen, Guangyao Wu, Dr. Rubel Khan, Eric Chung-Yu Liu, Lirong Shi, Trace Johnson, Dr. Tatsuki Abe, Dr. Ruiying Guo, Dr. Jun Zhao, Dr. Wu Liu, Yuchen Xing, Jingwen Luo, Chuang Feng, Jack Kelleher-Ferguson, Ngan Vo, and Anna DiFelice. Additionally, through collaboration, I have also met some great people from other groups and institutes, who have become both my collaborators and friends. They include Prof. Melissa Duhaime, Rachel Cable, Dr. Jessica Choi, and Lizy Michaelson, Dr. Haiping Sun, Dr. Kai Sun and Dr. Jerry Li.

In the past few years, I've had the privilege of working with many individuals from various industries. I appreciate their generous assistance, without which these achievements would not

have been possible. I extend my heartfelt thanks to Lorraine Hsu, Yuming Lai, Yujing Tan, Nagarajan Srivatsan, Amy Toolis, Samuel Esarey, Shane Peng, Na Fu, Weibin Cui, Piyush Thakre, Cristina Serrat, Jing Hu, David Meunier, Wenzhao Yang, and Xingyu Zhou.

Finally, I express my gratitude to my family and friends for their unconditional support and encouragement throughout this journey. It is their belief in me that has fueled my determination. I appreciate their companionship.

Table of Contents

Dedication ii

Acknowledgements iii

List of Tables ix

List of Figures x

Abstract xv

Chapter 1 Introduction 1

1.1 Overview: Goal and Motivation 1

1.2 Adhesion at the Interface 2

1.3 Sum Frequency Generation (SFG) Vibrational Spectroscopy 5

1.4 Degradation of Polyethylene Plastic 9

1.5 Presented Research 12

1.6 References 15

Chapter 2 Nondestructive in Situ Detection of Chemical Reactions at the Buried Interface between Polyurethane and Isocyanate-Based Primer 21

2.1 Introduction 21

2.2 Materials and Methods 24

2.2.1 Materials 24

2.2.2 Sample Preparation 24

2.2.3 ATR-FTIR Experiments 26

2.2.4 Peel Tests (180°) 26

2.3 Results and Discussion 27

2.4 Conclusion 36

2.5 References 37

Chapter 3 Investigation of Atmospheric Moisture Effect on the Molecular Behavior of Isocyanate-Based Primer Surface 40

3.1 Introduction 40

3.2 Materials and Methods 43

3.2.1 Materials 43

3.2.2 Sample Preparation 43

3.3 Results and Discussion 43

3.3.1 180° Peel Strength Test 43

3.3.2 SFG Experiments 46

3.4 Conclusion 55

3.5 References 56

Chapter 4 Probing Saltwater Immersion Effect on Buried Interfacial Structures between Sealant and Adhesion Promoter at the Molecular Level 58

4.1 Introduction 58

4.2 Materials and Methods 60

4.2.1 Materials 60

4.2.2 Sample Preparation 61

4.3 Results and Discussion 62

4.3.1 Two-layer Sample Geometry 63

4.3.2 Spin-coated Thin Layer Samples on Prism Substrate 65

4.3.3 Three-layer Sample Geometry 66

4.4 Conclusion 74

4.5 References 75

Chapter 5 Evaluating Polyethylene Weathering Processes after Simulated Solar Exposure and in Situ Lake Deployment 77

5.1 Introduction 77

5.2 Materials and Methods 81

5.2.1 Materials 81

5.2.2 Weathering Conditions 82

5.2.3 ATR-FTIR Experiments 84

5.2.4 Water Contact Angle Measurement 85

5.2.5 Raman Spectroscopy 85

5.2.6 Grazing Incident X-ray Diffraction (GIXRD) 86

5.2.7 Nanoindentation Tests 86

5.2.8 Statistical Approach 87

5.3 Results and Discussion 88

5.3.1 Phase 1 88

5.3.2 Phase 2 104

5.4 Conclusion 115

5.5 References 117

Chapter 6 Conclusion and Outlook 122

6.1 Conclusion 122

6.2 Outlook 125

List of Tables

Table 5.1 Material parameters of polyethylene investigated in this research 82

Table 5.2 Treatment conditions on samples..... 82

Table 5.3 Summary of changes in carbonyl index and vinyl index for plaques after 4 weeks of simulated solar exposure. 92

Table 5.4 Fixed effect tests 110

Table 5.5 Fixed effects parameter estimates in the linear mixed model 111

List of Figures

Figure 1.1 Schematics showing a) an SFG energy level diagram and b) a typical SFG experiment sample geometry. 7

Figure 2.1 Schematic showing a polyurethane potting compound (PPC) on a primed substrate in a real application. 22

Figure 2.2 Schematic showing an SFG sample geometry used in this study to collect SFG spectra from the buried primer (orange layer)/PPC (green cylinder) interface. 26

Figure 2.3 (a) Schematic showing the 180° peel strength test. (b) Results of 180° peel tests. 27

Figure 2.4 ATR-FTIR spectra collected from the primer (top) and the PPC (bottom) in the frequency region of 1200-3600 cm^{-1} 28

Figure 2.5 SFG ppp (a) and ssp (b) spectra collected from the buried primer/PPC interface before annealing. SFG ppp (c) and ssp (d) spectra collected from the buried primer/PPC interface after annealing. 29

Figure 2.6 (a) Schematic showing the SFG sample preparation process used to collect SFG spectra from the primer/PPC interface after placing a cured PPC sample in contact with primer. SFG ppp (b) and ssp (c) spectra collected from the buried primer/PPC interface after the PPC was cured first and was then placed in contact with the primer. 30

Figure 2.7 Postulated chemical reaction between isocyanate and primary amino groups. 31

Figure 2.8 SFG ppp (a) and ssp (b) spectra collected from the buried primer/PPC Part B interface after annealing. 32

Figure 2.9 SFG ppp spectrum collected from the primer/PPC Part A interface after annealing. 33

Figure 2.10 The ppp (a) and ssp (b) SFG spectra collected from the PPC (on CaF_2). The ppp (c) and ssp (d) SFG spectra collected from the PPC (on CaF_2)/primer interface before annealing. The ppp (e) and ssp (f) SFG spectra collected from the PPC (on CaF_2)/primer interface after annealing. 34

Figure 2.11 SFG ppp and ssp spectra collected from the PPC (a) (b), primer (c) (d) and PPC/primer interfaces (e) (f) after annealing. 36

Figure 3.1 Schematic diagram for the reaction of isocyanates with water. 42

Figure 3.2 Results of 180° peel strength tests. Groups 1-4: the primers used for tests were exposed to nitrogen for 1 h, air with 18% RH for 4 h, air with 18% RH for 16 h, and air with 50% RH for 4 h, respectively..... 44

Figure 3.3 (a) SFG ppp and (b) ssp spectra collected from the primer (on CaF_2) at 18% RH at 0-h, 4 h, and 16 h. (c) SFG ppp and (d) ssp spectra collected from the primer (on CaF_2) at 50% RH at 0 h and 4 h. The spectra were collected in the wavenumber range from 2050 to 2400 cm^{-1}. 47

Figure 3.4 SFG ppp (left) and ssp (right) spectra collected from the primer (on CaF_2) at 18% RH at 0 h, 4 h, and 16 h in the wavenumber range from 1555 to 1700 cm^{-1}..... 48

Figure 3.5 SFG ppp (left) and ssp (right) spectra collected from the primer (on CaF_2) at 50% RH at 4 h in the wavenumber range from 1555 to 1700 cm^{-1}..... 49

Figure 3.6 The relationship between the SFG susceptibility ($|\chi^{(2)}$eff, ppp$|/|\chi^{(2)}$eff, ssp$|$) and the tilt angle (θ) of a C=O group vs. the surface normal. 50

Figure 3.7 SFG ssp spectra collected from the primer (on CaF_2) at 0 h, 18% RH at 4 h, 16 h and 50% RH at 4 h. The spectra were collected in the wavenumber range from 3100 to 3500 cm^{-1}. 51

Figure 3.8 a) Chemical structure of PMDI. b) SFG ppp (left) and ssp (right) spectra collected from PMDI (on CaF_2) at 18% RH in the wavenumber range from 2050 to 2400 cm^{-1}..... 53

Figure 3.9 SFG ppp (left) and ssp (right) spectra collected from PMDI (on CaF_2) at 18% in the wavenumber range from 1555 to 1700 cm^{-1}..... 54

Figure 4.1 Schematic showing the design of three sample geometries used in this study: (a) two-layer sample, (b) spin coated thin layer sample (either adhesion promoter or sealant), and (c) three-layer sandwiched sample. (d) Schematic of sample geometry for collecting SFG spectra. 62

Figure 4.2 a) Schematic showing the two-layer sample geometry before saltwater immersion, ssp (red) and ppp (blue) SFG spectra collected from the sample before immersion. b) Schematic showing the two-layer sample geometry after saltwater immersion at 60°C for 7 days, ssp (red) and ppp (blue) SFG spectra collected from the sample after the 7-day immersion. c) Schematic showing the two-layer sample geometry placed in air at 60°C for 7 days without saltwater immersion, ssp (red) and ppp (blue) SFG spectra collected from the sample after the treatment at 60°C for 7 days. 64

Figure 4.3 a) Schematic showing the adhesion promoter 6111 applied on prism and ssp (red) as well as ppp (blue) SFG spectra collected from the sample. b) Schematic showing the sealant applied on prism and ssp (red) as well as ppp (blue) SFG spectra collected from the sample..... 66

Figure 4.4 Schematic showing the sandwich sample geometry (a, b, c, d) applied on the prism, ssp (red) and ppp (blue) SFG spectra collected from the sample in the condition of: a) before immersion; b) after saltwater immersion at 60°C for 1 hour; c) after saltwater immersion at 60°C for 1 day; d) after saltwater immersion at 60°C for 7 days..... 68

Figure 4.5 a) Schematic showing the sandwich sample geometry placed in the air at 60°C for 1 day, ssp (red) and ppp (blue) SFG spectra collected from the sample after treatment. b) Schematic showing the sandwich sample geometry after salt water immersion at room temperature for 1 day, ssp (red) and ppp (blue) SFG spectra collected from the sample after the 1-day immersion. 70

Figure 4.6 Schematic showing the sandwich sample geometry made with the vinyl silane Y-15866, ssp (red) and ppp (blue) SFG spectra collected from the sample in the conditions of: a) before immersion; b) after saltwater immersion at 60°C for 1 day; c) after saltwater immersion at 60°C for 7 days. Schematic showing the sandwich sample geometry made with the amino silane APTES, ssp (red) and ppp (blue) SFG spectra collected from the sample in the conditions of: d) before immersion; e) after saltwater immersion at 60°C for 1 day; f) after saltwater immersion at 60°C for 7 days. 71

Figure 4.7 Schematic showing the sandwich sample geometry made with the pre-hydrolyzed vinyl silane Y-15866, ssp (red) and ppp (blue) SFG spectra collected from the sample in the conditions of: a) before immersion; b) after saltwater immersion at 60°C for 1 day; c) after saltwater immersion at 60°C for 7 days. Schematic showing the sandwich sample geometry made with the pre-hydrolyzed amino silane APTES, ssp (red) and ppp (blue) SFG spectra collected from the sample in the conditions of: d) before immersion; e) after saltwater immersion at 60°C for 1 day; f) after saltwater immersion at 60°C for 7 days. 73

Figure 4.8 Schematic of SFG sample geometry and SFG ssp (red) and ppp (blue) spectra collected from a sample with thiol-epoxy sealant alone before (a) and after (b) the 3% saltwater immersion at 60°C for 1 day. 74

Figure 5.1 Schematic of plastic samples deployed in the lake for in situ exposure..... 84

Figure 5.2 ATR-FTIR of LLDPE film #5 and HDPE film #6 in pristine condition (T0), after two and four weeks of simulated solar exposure. (a: 3100-3800 cm^{-1}, b: 1550-1900 cm^{-1}, c: 880-940 cm^{-1}). 89

Figure 5.3 Carbonyl index (a) and vinyl index (b) of LLDPE film #5 and HDPE film #6 in pristine condition (T0), after two and four weeks of simulated solar exposure. 90

Figure 5.4 ATR-FTIR spectra of LLDPE plaques J, L in pristine condition (T0), after two and four weeks of simulated solar exposure (a: 3100-3800 cm^{-1}, b: 1550-1900 cm^{-1}, c: 880-940 cm^{-1}). 90

Figure 5.5 Carbonyl index (a) and vinyl index (b) of LLDPE plaques in pristine condition, after two and four weeks of simulated solar exposure. 90

Figure 5.6 ATR-FTIR spectra of HDPE plaques G, H and LLDPE plaques J, L undergoing four weeks of simulated solar exposure (a: 3100-3800 cm^{-1}, b: 1550-1900 cm^{-1}, c: 880-940 cm^{-1}).... 91

Figure 5.7 a) Schematic of different sample locations for testing. ATR-FTIR spectra of HDPE plaques H (b, c, d) and LLDPE J (e, f, g) undergoing four weeks of simulated solar exposure at different locations (b, e: 3100-3800 cm^{-1}, c, f: 1550-1900 cm^{-1} d, g: 880-940 cm^{-1}). 93

Figure 5.8 Water contact angle measurement results of PE surfaces without and with two weeks of simulated solar exposure. 94

Figure 5.9 Raman results of LLDPE samples in pristine condition (T0), after two and four weeks of simulated solar exposure: a) LLDPE film #5 crystalline region, b) LLDPE plaque L crystalline region, c) LLDPE plaque K crystalline region, d) LLDPE plaque J crystalline region, e) LLDPE film #5 amorphous region, f) LLDPE plaque L amorphous region, g) LLDPE plaque K amorphous region, h) LLDPE plaque J amorphous region. 95

Figure 5.10 Raman results of HDPE samples in pristine condition, after two and four weeks of UV exposure: a) HDPE film #6 crystalline region, b) HDPE plaque G crystalline region, c) HDPE plaque H crystalline region, d) HDPE film #6 amorphous region, e) HDPE plaque G amorphous region, f) HDPE plaque H amorphous region. 96

Figure 5.11 Raman intensity changes of samples as a function of the UV exposure time in the crystalline region (left) and the amorphous region (right). 97

Figure 5.12 GIXRD results of samples in pristine condition, after two and four weeks of UV exposure: a) LLDPE plaque L, b) LLDPE plaque K, c) HDPE plaque G, d) HDPE plaque H, e) Summary of the crystallinity change trend observed through GIXRD analysis. 98

Figure 5.13 Nanoindentation results: plaques G, H, J, K, and L in pristine condition and after four weeks of simulated solar exposure. 99

Figure 5.14 Summary of the normalized difference between 4-week aged and pristine samples: a) Raman deduced crystallinity, b) GIXRD deduced crystallinity, c) Carbonyl index, d) Vinyl index, e) Nanoindentation. 101

Figure 5.15 Correlations of the crystallinities measured from different samples with GIXRD and Raman spectroscopy. 103

Figure 5.16 ATR-FTIR spectra of pristine LLDPE plaque J, samples after simulated solar exposure and/or lake deployment. “J0”, “J2”, and “J4” refer to the samples with 0, 2, and 4 weeks of simulated solar exposure. The sample names containing “rinse” refer to the samples rinsed using the rinsing method presented above. “ELA-2mon” and “ELA-14mon” refer to the samples with 2 and 14 months of lake deployment, respectively. “1.5m”, “15m”, and “30m” refer to the sample lake deployment depth for 1.5, 15, and 30 meters from the water surface respectively. The peaks centered at 1713 cm^{-1} (marked in the shaded orange area) are carbonyl C=O stretching signals. 105

Figure 5.17 ATR-FTIR spectra of all pristine samples, samples after simulated solar exposure, lake deployment, or both. 107

Figure 5.18 a) Summary of calculated carbonyl indices (CI) based on samples before and after different treatments. b) Plot of standard deviation of carbonyl indices for samples under different UV aging conditions. c) Plot of standard deviation of carbonyl indices for samples with different deployment times. 108

Figure 5.19 a) Linear mixed model of predicted CI (x-axis) vs. observed CI (y-axis) ; b) Conditional residual by the predicted plot. 109

Figure 5.20 Model profiler plot when PE type is J. 111

Figure 5.21 Model profiler plot when PE type is G. 113

Figure 5.22 Interaction plot. 113

Abstract

Polymeric materials are essential in industrial production, fulfilling needs from basic packaging to complex structural requirements. It is evident that polymer materials have significantly facilitated various aspects of daily life. On the other hand, plastic pollution has also emerged as a growing environmental concern.

This thesis research focuses on investigating various industrial polymer materials to understand adhesion mechanisms in sealing applications (Chapter 2 to Chapter 4) and environmental degradation in polyethylene packaging materials (Chapter 5). Sum frequency generation (SFG) vibrational spectroscopy, a second-order nonlinear optical spectroscopy with submonolayer surface/interface sensitivity, was employed to study molecular behaviors at surfaces and buried interfaces in situ nondestructively, providing insights into adhesion fundamentals. For the degradation study of polyethylene, a combination of analytical techniques and advanced statistical analysis techniques were introduced, contributing to a more comprehensive picture of the degradation process.

Potting compounds and sealants are designed to seal gaps and encapsulate substrates as protective barriers. Polyurethane potting compounds are usually applied after pre-coating substrate surfaces with primers to improve adhesion, but fundamental mechanisms of adhesion enhancement are not fully understood. In Chapter 2, SFG was used to explore the interfacial molecular structures between a polyurethane potting compound and an isocyanate-based primer. The findings suggest that isocyanate groups in primer at the interface were consumed by their reaction to amino groups

from potting compound, and the formation of urea chemical bonds at the interface contributed to the enhanced adhesion.

Along with the study of the buried interface between the primer and potting compound, it was observed that extended primer exposure to the atmosphere before applying the polyurethane potting compound reduces adhesion enhancement noticeably. In Chapter 3, SFG was utilized to examine the surface of the isocyanate-based primer under varying environmental conditions. The results indicate a decreased number of isocyanate groups on the surface due to the reaction with moisture, and the reduction in adhesion was more pronounced with higher relative humidity and longer exposure times.

In addition to exploring the adhesion system of the polyurethane potting compound and isocyanate-based primer, Chapter 4 focuses on a thiol-epoxy model fuel tank sealant in contact with a silane-based adhesion promoter. The immersion effect in saltwater at elevated temperatures was studied by SFG. The results indicate that immersion in saltwater led to disordering at the interface between the adhesion promoter and sealant, and the weaker interfacial interactions can play a role in affecting the adhesion.

Understanding the fate of plastics in the environment is crucial for finding sustainable solutions to plastic waste challenges. In Chapter 5, a combination of analytical techniques (attenuated total reflectance Fourier transform infrared spectroscopy (ATR-FTIR), water contact angle measurement, Raman, GIXRD, nanoindentation) was applied to systematically measure samples exposed to simulated solar exposure (phase 1). Then, an in-depth study involving lake deployment was conducted in phase 2 using ATR-FTIR, and the results were further studied using statistical analysis to reveal their relationships to a variety of aging conditions. The study suggests

that polyethylene with lower densities, longer UV aging, and their interactions led to noticeable polyethylene structural changes, whereas lake deployment showed insignificant effects.

In summary, this thesis research offers molecular and structural insights into diverse polymer materials for industrial applications. These methodologies aim to inspire and guide the exploration of a wider range of polymer materials in future development endeavors.

Chapter 1 Introduction

1.1 Overview: Goal and Motivation

Polymeric materials have become indispensable components in industrial production, playing a crucial role in ensuring the quality of our daily lives. With continuous technological advancements and evolving environmental considerations, efforts are underway to develop and optimize a broader range of polymer materials to meet the emerging industrial challenges posed by dynamic requirements and sustainability goals. The focus of this thesis research lies in the investigation of polymeric materials tailored for real-world applications. The goal is to elucidate the underlying mechanisms governing observed phenomena, providing insights that help improve materials in the future through experimentation and analysis.

The adhesion of polymer materials is one of the main focal points of this thesis research. Understanding the adhesion mechanism at the interface is crucial for designing and formulating polymer products with enhanced performance. The first project focused on illuminating the adhesion mechanism of a primer that enhances the adhesion strength of a potting compound. Building upon the insights gained from the first research, the second study investigated the atmospheric moisture effect on the adhesion efficiency of the primer. In the third part, model sealants employed in fuel tank interiors were analyzed to study interfacial changes during immersion in saltwater and their potential effect on adhesion. The above three projects were performed in collaboration with PPG. As adhesion takes place at the material interface, an analytical technique capable of examining molecular behaviors at surfaces and interfaces would

be ideal to elucidate the phenomena. In the research, sum frequency generation (SFG) vibrational spectroscopy serves as the major testing tool to study the adhesion at the molecular level. SFG has the capability to detect surfaces and buried interfaces in situ and non-destructively without the requirement for demanding operational environments. Meanwhile, its sub-monolayer level surface sensitivity prevents interference from bulk structure, making it a valuable metrology to probe a variety of materials. More details regarding SFG methodology and setup will be described below. By shedding light on molecular behaviors and interactions, this research endeavors to provide guidance for the enhancement of material design and formulation strategies.

Another focal point of the research is the degradation of plastics designed for packaging applications. The increasing generation of plastic waste has raised significant environmental concerns. In contrast to incineration or landfilling, recycling emerges as a more environmentally friendly approach and is actively being explored by industry. However, the question remains about the retained mechanical strength of recycled plastics to support their intended functions. Exposure of plastics to environmental conditions in nature can lead to performance changes that may impact their recyclability. In this research, plastics are subjected to simulated or real natural conditions to investigate the molecular structural changes over time. The goal is to elucidate the connection between these changes and their consequent impact on material performance, aiding in attaining a more thorough understanding of degradation processes in plastics used for packaging applications. Ultimately, the findings of this study are expected to play a role in shaping strategies that advance recyclability and promote sustainable solutions.

1.2 Adhesion at the Interface

Adhesion refers to the attraction between two different substances, driven by intermolecular forces existing between them.[1] Adhesives and sealants, with the ability to bond at

least two surfaces and fill the gap between them to create a barrier, respectively, form surface attachment through the process of adhesion. During application, the adhesive or sealant is in a liquid state to wet the surfaces and establish molecular contact with the adherends. Subsequently, the curing or hardening process occurs within the adhesive or sealant's bulk to form a cohesively strong solid, while adhesion takes place at the interface.[2] Therefore, the nature of the interface plays a crucial role in determining the properties and quality of adhesion.

The use of adhesives and sealants has a history dating back thousands of years, originating from natural substances. During the early 1900s, synthetic polymeric products started replacing many naturally occurring ones due to their stronger adhesion, more formulation options, and higher resistance to operating conditions. Since then, the progress in modern polymeric adhesives and sealants has allowed them to establish a remarkable market presence across a broad spectrum of industrial applications. Spurred by increasing market demands and evolving requirements, the desire to develop adhesives and sealants for enhanced and consistent performance encourages further studies on adhesion. As adhesion happens at the interface between the substrate surface and the adhesive or sealant, the success of bonding relies significantly on both the condition of the substrate and the formulation of adhesive or sealant. Strategies have been developed to help achieve ideal joints for many applications. For example, surface treatments (e.g. acid etch, corona, flame, thermal, plasma) have proved successful in many applications. They are performed prior to the application of adhesives or sealants to remove weak boundary layers, protect the substrate surface and/or influence the surface energy of the substrate.[1] The application of primers or adhesion promoters also helps enhance adhesion by establishing strong bonds with both the substrate and the adhesive or sealant – they can be added as an additional layer on the substrate before the adhesive or sealant is applied, or in other cases adhesion promoter is already included

in the formulation of the adhesive or sealant. Adhesives and sealants are often composed of complex formulations of components. Careful design of polymers together with the selection of modifying substances and additives are key to adhesion performance. In addition, other factors such as the operation conditions and external influences from the environment also significantly contribute to the efficiency and permanence of adhesion at the interface.

Acquiring details regarding the adhesion phenomenon in real-world applications would enhance the understanding of the product's usage scope and provide more effective insights for improvement methods. Several theories of adhesion have been proposed to help describe and predict joint strength. For example, the adsorption theory attributes the adhesion to molecular contact and resulting attractive forces, such as secondary or van der Waals forces.[1] The mechanical interlocking theory of adhesion describes that adhesives and sealants fill the irregularities on the surface of the substrate, displacing trapped air at the interface before undergoing hardening. The chemical bonding theory of adhesion suggests the formation of bonds across the interface. Other theories like the electrostatic theory and diffusion theory have also been proposed to understand adhesion.[3-7] While these theories offer valuable insights into understanding adhesion phenomena, direct observation at the buried interface would greatly enhance our fundamental knowledge of adhesion. However, research in the past was constrained by limitations in testing methods, making it challenging to directly obtain information about interface adhesion. Many earlier studies on adhesion placed great emphasis on the macro mechanical testing aspect instead of interfacial molecular structures and molecular interactions, therefore, further investigations are needed to elucidate molecular mechanisms behind adhesion-promoting strategies or the reduced adhesion caused by environment or application conditions. In the past few decades, advancements in characterization techniques have enabled the exploration of interfacial changes to investigate

adhesion in situ at the molecular level. The research presented in three chapters of this thesis systematically delves into the molecular behaviors of materials at surfaces and interfaces, employing the nondestructive technique of SFG spectroscopy to study adhesion mechanisms aimed at addressing real-world challenges. Chapter 2 focuses on the adhesion at the interface between a primer and potting compound (in some cases used interchangeably with sealant) to investigate the molecular mechanism of adhesion enhancement by the application of the primer. Chapter 3 explores the effect of the environment that impacted primer and led to the reduced adhesion with the potting compound at the interface. Chapter 4 analyzes external influences during service that lead to changes in interfacial molecular interactions of a sealant with an adhesion promoter and its implications for adhesion.

1.3 Sum Frequency Generation (SFG) Vibrational Spectroscopy

Examining a buried interface precisely in its native state can be challenging.[8] The nature of the buried interface limits the precise in situ measurement. As the bulk structure takes up a greater portion compared to the interfacial moiety, it is common to see bulk structure contributing dominantly to the overall results obtained. Molecular interactions at buried interfaces tend to be subtle compared to those in the bulk, making it difficult to obtain precise results at a molecular level due to signal interferences from homogeneous bulk phases. There are limited methodologies developed for the in situ, nondestructive examination of buried interfaces. Commonly used analytical techniques, such as X-ray photoelectron spectroscopy (XPS), time-of-flight secondary ion mass spectrometry (ToF-SIMS), attenuated total internal reflectance-FTIR (ATR-FTIR), surface-enhanced Raman scattering (SERS), and atomic force microscopy (AFM), have limitations when applied to buried interfaces. Many of these methods are based on separating the interface into two surfaces, a limitation that may compromise accuracy, especially for certain

adhesion systems where strong adhesion bonding connects the materials at the joining interface. In such cases, the separation process can potentially destroy or alter the molecular structures at the original buried interface.[9-11]

Sum frequency generation (SFG) vibrational spectroscopy, on the other hand, has proven to be a powerful tool for observing molecular structures and interactions at buried interfaces in situ and in real time. As a second-order nonlinear optical process, SFG is feasible to probe the molecular-level changes at interfaces in situ and non-destructively.[12-23] SFG has been employed extensively in research endeavors to elucidate interfacial molecular behaviors.[13,17,19,24-34] SFG signal is generated by overlapping a visible beam with a fixed wavelength (e.g., at 532 nm) and a frequency-tunable IR beam at the interface both spatially and temporally. The frequency of SFG signal is the sum of the frequencies of the two input beams. The resonant enhancement of signal intensity occurs when the frequency of the incident IR beam matches the vibrational transition frequency of sample molecules at the interface.[35-39] Schematics showing an SFG energy level diagram and SFG experiment sample geometry and are displayed in **Figure 1.1**. Similar to FTIR and Raman spectroscopy, SFG generates spectra based on signal intensity versus wavenumber, yet its distinctive advantage lies in the fact that the signal specifically originates from the surface or interface. The selection rule of the SFG process, a second-order nonlinear optical process, indicates that SFG signals can exclusively be generated from a medium with no inversion symmetry (under the electric dipole approximation). The signal intensity of SFG is proportional to the square of the second-order nonlinear optical susceptibility $\chi^{(2)}$. $\chi^{(2)}$ is a polar sensor of rank three, and the sign is reversed under the inversion operation to satisfy $\chi^{(2)}(r) = -\chi^{(2)}(-r)$. For centrosymmetric materials, the sign of $\chi^{(2)}$ remains unchanged under the same operation, thus the only viable solution to satisfy the equation is $\chi^{(2)}$ being equal to 0. As a result, no SFG signal can be generated for those

centrosymmetric materials with inversion symmetry. However, for surfaces and interfaces where inversion symmetry is broken (noncentrosymmetric), second-order nonlinear optical phenomenon can occur as $\chi^{(2)}$ (or SFG signal) is not equal to zero. This characteristic enables SFG to characterize surfaces and buried interfaces with sub-monolayer interfacial specificity non-destructively.[40-44] In contrast, bulk materials have inversion symmetry and thus do not contribute to the signal, which eliminates signal interference from them and allows for precise analysis of interfacial behaviors using SFG. Consequently, SFG serves as a suitable tool for studying molecular structures at buried interfaces.

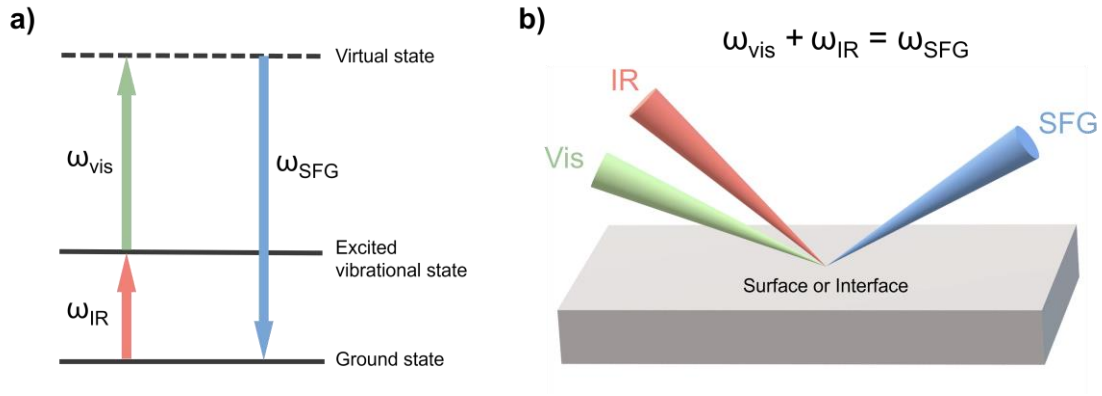


Figure 1.1 Schematics showing a) an SFG energy level diagram and b) a typical SFG experiment sample geometry.

Our SFG experiments were carried out by using a commercial SFG spectrometer manufactured by EKSPLA. A Nd:YAG laser with an output wavelength of 1064 nm was used as a light source to generate the visible and infrared input laser beams for the SFG study. The visible light at 532 nm was produced by doubling the frequency of the 1064 nm light through a second harmonic generation process, while the frequency tunable infrared beam was generated through optical parametric generation/amplification and difference frequency generation. The input visible and infrared laser beams overlap spatially and temporally at the sample surface/interface with

incident angles of 60° and 54° to the surface normal respectively. The reflected SFG signal was directed through a monochromator and measured by a photomultiplier tube (Hamamatsu Corp., Hamamatsu City, Shizuoka, Japan).[45] All SFG spectra were collected using the ssp (s-polarized SFG signal, s-polarized input visible, and p-polarized input infrared) and ppp polarization combinations of the input and output beams by scanning the IR beam frequency. Molecular structural information of the interface can be obtained from a generated SFG spectrum by plotting the intensity of the SFG signal versus the wavenumber of the IR input beam.[35,46,47] Quantitative information regarding orientation, orientation distribution, and surface coverage of probed functional groups can be studied through analyzing the intensities of SFG peaks collected using various polarization combinations.

The versatility of SFG spectroscopy allows for comprehensive investigations using different sample geometries to meet the diverse surface analysis needs across different disciplines. SFG technique has been previously utilized to study various polymer interfaces, such as the dewetting process of polystyrene films on substrates,[48] surface hydration of zwitterionic polymers exposed to salt solutions,[49,50] antimicrobial polymers interacting with lipid bilayers,[51] epoxy underfills in the semiconductor industry,[52] etc. In this thesis research, SFG was extensively employed to explore industrially relevant systems concerning adhesion. Right-angle calcium fluoride prisms (Altos Photonics, Inc., Bozeman, MT) were used in this study as substrates. In the first project, SFG was used for studying the interfacial molecular behavior of a primer and potting compound, and the results were correlated with their peel strength to elucidate the function of interfacial bonding. Following that, SFG was applied to detect the molecular change on the primer surface due to the atmospheric moisture effect to show its impact on resulting adhesion. In another study regarding a sealant and adhesion promoter system immersed in salt water, SFG spectra

before and after immersion were measured and compared to analyze the molecular change at the interface. The research presents a general approach demonstrating the potential of SFG to probe interfacial molecular interactions in a broad range of materials applications in the future.

1.4 Degradation of Polyethylene Plastic

Plastics are synthetic polymers derived from petrochemicals.[53] Known for their cost-effectiveness, lightness, durability, and processibility, plastics can be easily made into various products suitable for a wide array of applications.[54-56] This adaptability has resulted in a significant surge in plastic production over the past few decades.[54]

Surpassing an annual production of 300 million tons since 2014, global plastic production has led to a rapid increase in plastic accumulation in the environment.[57,58] This concerning trend is exacerbated by the limited global recycling rates,[59-63] resulting in over half of plastic waste being either landfilled or entering the natural environment. This poses a substantial threat to environmental health and resource sustainability.[64] A significant proportion of plastic waste faces potential fragmentation and degradation in the environment. In response to the escalating environmental challenges posed by plastic waste, a critical need has emerged for comprehensive research on plastic degradation. Such research not only helps to shed light on the fate of degraded materials but also provides crucial insights for the development of strategies to mitigate the environmental impact of plastic degradation.

Polyethylene stands out as one of the most extensively produced and widely utilized plastic materials globally.[65-68] Derived from polyolefins, polyethylene exhibits exceptional inertness and biological inactivity owing to its extensive molecular size, hydrophobic nature, and absence of susceptible functional groups.[69-71] Polyethylene can be produced in different families, including high-density polyethylene (HDPE), low-density polyethylene (LDPE), and linear low-density

polyethylene (LLDPE). In addition, various families of polyethylene can be easily processed, and the versatility enables customization for specific applications. Beyond being a suitable and cost-effective choice in packaging, polyethylene also reveals its importance in diverse sectors, including construction, automotive industry, and medical devices, performing as a fundamental and adaptable material in extensive industrial applications.

Although polyethylene has long been recognized for its significant contributions to enhancing our quality of life, the persistent presence of used polyethylene materials in the environment also raises profound questions about the long-term ecological impact, including the increasing plastic debris in nature.[72,73] Understanding polyethylene's fate in the environment emerges as an indispensable guidepost for finding sustainable and responsible solutions to address challenges posed by plastic waste. Numerous research endeavors are dedicated to elucidating the mechanisms and kinetics governing the degradation of polyethylene, which holds the promise of generating valuable insights that can benefit the development of efficient recycling strategies.

The degradation of polyethylene can be influenced by various factors. Various research endeavors have been undertaken to comprehend the degradation mechanisms of polyethylene, employing diverse treatment methods. Photodegradation is a significant pathway that may take place on polyethylene in the environment.[74-77] Triggered by sunlight exposure, with UV as the main source, photodegradation results in the deterioration of polymer chains and an increased susceptibility to subsequent degradation mechanisms.[78-81] A substantial portion of research regarding photooxidation has concentrated on specific model polyethylene materials or chosen commercial products utilizing limited characterization techniques. Further investigations are needed to establish a direct correlation between polyethylene manufacturing parameters and degradation behaviors through a more comprehensive approach. For biodegradation, previous

literature shows the feasibility of some microorganisms that can consume plastics and/or lead to the breaking down of polyethylene.[82-94] Thermal degradation, on the other hand, involves the application of heat, accelerating the deterioration of polyethylene structures.[95-101] There are also other pathways influencing the degradation of polyethylene. While laboratory studies provide valuable insights into the fundamental mechanisms of polyethylene breakdown under limited controlled variables, natural weathering introduces a multitude of variables that are often not easy to replicate in a laboratory setting. When polyethylene is left in the environment, different variables contribute synergistically to the material rather than a single pathway.[102] Variables such as exposure to varying levels of sunlight, microbial activity, and the presence of diverse environmental elements significantly influence the degradation process. Therefore, it is helpful to investigate how polyethylene behaves in real settings to understand environmental impact. This comprehensive perspective is essential for comprehending the environmental impact of degraded materials and assisting plastic producers in formulating effective solutions.

This research incorporates both laboratory exposure through a UV accelerated weathering test chamber and in situ exposure via lake deployment. This dual approach allows for the examination of weathering effects on polyethylene, facilitating investigations into the individual and combined roles of solar radiation and biofilm deposition in the polymer degradation processes. During the UV pre-aging phase, a variety of analytical techniques such as ATR-FTIR (chemical structure analysis) , Raman microscopy (change in crystallinity), nanoindentation (investigation of mechanical properties), contact angle measurements (surface hydrophilicity study), and grazing angle X-ray diffraction (further investigation on crystallinity changes compared to Raman results) were employed to assess changes in the physical and chemical properties of polyethylene materials at different exposure levels. Details will be described in the following sections. This systematic

approach aimed to foster a more comprehensive understanding of the photodegradation of polyethylene materials. Further analysis was subsequently conducted on samples after lake deployment, allowing for a systematic evaluation of the effects of various experimental and sample factors on polyethylene degradation and the correlations of these factors.

1.5 Presented Research

This thesis research mainly studies the adhesion and degradation of polymer materials for industrial applications with four aspects covered: 1) nondestructive in situ detection of chemical reactions at the buried interface between polyurethane and isocyanate-based primer; 2) investigation of atmospheric moisture effect on the molecular behavior of isocyanate-based primer surface; 3) probing salt water immersion effect on buried interfacial structures between sealant and adhesion promoter at the molecular level; 4) evaluating polyethylene weathering processes after simulated solar exposure and in situ lake deployment.

Chapter 2 presents research on the role of isocyanate-based primers in enhancing the adhesion of polyurethane potting compound to the substrate. SFG was applied to probe changes in interfacial molecular structures in situ between the potting compound and primer. ATR-FTIR spectroscopy and 180° peel tests were utilized as complementary techniques to support the SFG analyses and establish the relationship between structure and property. A series of SFG experiments were designed to confirm that the interfacial reaction occurred at the interface between the polyurethane potting compound and primer, based on the consumption of reactive groups and the presence of bonding groups observed at the buried interface. The results indicate that the formation of chemical bonds at the interface was responsible for the enhancement of adhesion.

In Chapter 3, the atmospheric moisture effect on the primer was systematically investigated. Time and humidity-dependent experiments were performed to monitor the molecular behavior at the primer surface using SFG. In addition, 180° peel testing experiments were conducted to measure the adhesion properties of primers after exposed to the corresponding conditions to correlate to SFG results. This study on the changes at the primer surface in different environments aims to provide an in-depth understanding of the moisture effect on isocyanate-based primers, paving the way to optimizing conditions for various formulated coatings, particularly those involving isocyanate primers. These learnings can be helpful in exploring a broader range of coatings and surface layers and improving customer product use guidelines.

Chapter 4 delves into the immersion effect that can impact the adhesion between a formulated sealant and an adhesion promoter. Fuel tank sealants may encounter various challenges due to the demanding conditions of their operational environments. SFG was applied to investigate a thiol-epoxy sealant on the silane-based adhesion promoter following exposures to 3% salt water conditions at elevated temperatures. The goal is to understand the interfacial molecular behavior as well as their potential role in adhesion. The results imply that the saltwater immersion process led to the disordering of the adhesion promoter/sealant interface (caused by interfacial structural randomization), which could potentially have implications for adhesion.

Chapter 5 mainly focuses on understanding the degradation processes of polyethylene for packaging applications. To help determine the individual and combined role of solar radiation and biofilms in the polyethylene degradation processes, changes in various types of polyethylene samples were studied via a combination of simulated solar exposure and in situ freshwater lake deployment. In phase 1, the polyethylene samples underwent simulated solar exposure as UV pre-aging for varying durations. A comprehensive analysis involving different kinds of techniques was

employed to assess both chemical and physical changes in the exposed materials. The study revealed that enhancements in polar groups, hydrophilicity, crystallinity, and elastic modulus due to structural alterations are time-dependent and exhibit variability based on their parameters. In phase 2, samples were deployed in the lake at different depths for different lengths of time. Chemical changes in samples were measured by ATR-FTIR, and the results were quantified and further processed using statistical analysis to reveal their relationships to a variety of aging conditions. The study indicates that the types of polyethylene, UV aging, and their interactions are the key factors that led to the polyethylene structural changes. The lake deployment in the setting does not yield a significant effect on polyethylene degradation.

In summary, this thesis provides molecular and structural insights into diverse polymer materials used across various industrial applications. Methodologies are presented that contribute to unraveling the underlying mechanisms behind the phenomena. Chapters 2, 3, and 4 focus primarily on gaining fundamental principles of adhesion in formulated sealants and potting compounds. The chemical understanding obtained from these studies is linked to adhesion performance, intending to establish design principles and facilitate formulation for targeted and superior performance properties. The studies validated the feasibility of SFG in conjunction with other analytical techniques for uncovering the mechanisms of complex formulations. Chapter 5 demonstrates a systematic study of measuring the environmental weathering process of packaging plastic. The research aims to aid in the development of sustainable packaging solutions for the future. Leveraging a series of analytical tools and incorporating statistical analysis serve as a beneficial strategy to enhance the understanding of the environmental fate of plastics.

1.6 References

1. Petrie, E. M., *Handbook of adhesives and sealants*. McGraw-Hill Education: 2007.
2. Cognard, P., *Handbook of adhesives and sealants: basic concepts and high tech bonding*. Elsevier: 2005.
3. Ebnesajjad, S.; Landrock, A. H., *Adhesives technology handbook*. William Andrew: 2014.
4. Awaja, F.; Gilbert, M.; Kelly, G.; Fox, B.; Pigram, P. J. Adhesion of polymers. *Prog. Polym. Sci.* **2009,** 34 (9), 948-968.
5. Baldan, A. Adhesion phenomena in bonded joints. *Int. J. Adhes. Adhes.* **2012,** 38, 95-116.
6. Meschut, G.; Janzen, V.; Olfermann, T. Innovative and Highly Productive Joining Technologies for Multi-Material Lightweight Car Body Structures. *J. Mater. Eng. Perform.* **2014,** 23 (5), 1515-1523.
7. Gong, L.; Xiang, L.; Zhang, J.; Chen, J.; Zeng, H. Fundamentals and Advances in the Adhesion of Polymer Surfaces and Thin Films. *Langmuir* **2019,** 35 (48), 15914-15936.
8. Zhang, S.; Andre, J. S.; Hsu, L.; Toolis, A.; Esarey, S. L.; Li, B.; Chen, Z. Nondestructive in situ detection of chemical reactions at the buried interface between polyurethane and isocyanate-based primer. *Macromolecules* **2020,** 53 (22), 10189-10197.
9. Lu, X.; Zhang, C.; Ulrich, N.; Xiao, M.; Ma, Y. H.; Chen, Z. Studying Polymer Surfaces and Interfaces with Sum Frequency Generation Vibrational Spectroscopy. *Anal. Chem.* **2017,** 89 (1), 466-489.
10. Lee, L.-H., *Fundamentals of adhesion*. Springer Science & Business Media: 2013.
11. Zhang, C. Sum Frequency Generation Vibrational Spectroscopy for Characterization of Buried Polymer Interfaces. *Appl. Spectrosc.* **2017,** 71 (8), 1717-1749.
12. Andre, J. S.; Escoffery, N.; Ulrich, N. W.; Wu, Y.; Guo, W.; Yang, M.; Myers, J.; Chen, Z. Ultraviolet Light-Sensitive Debonding Layer for Reducing Adhesion of Polymer Adhesives for Recycling. *J. Phys. Chem. C* **2022,** 126 (44), 18907-18917.
13. Chae, I.; Ahmed, S.; Atitallah, H. B.; Luo, J.; Wang, Q.; Ounaies, Z.; Kim, S. H. Vibrational Sum frequency generation (SFG) analysis of ferroelectric response of PVDF-based copolymer and terpolymer. *Macromolecules* **2017,** 50 (7), 2838-2844.
14. Gao, J.; Stengel, P.; Lu, T.; Wu, Y.; Hawker, D. D.; Gutowski, K. E.; Hankett, J. M.; Kellermeier, M.; Chen, Z. Antiadhesive copolymers at solid/liquid interfaces: Complementary characterization of polymer adsorption and protein fouling by sum frequency generation vibrational spectroscopy and quartz-crystal microbalance measurements with dissipation monitoring. *Langmuir* **2023,** 39 (34), 12270-12282.
15. Ge, A.; Qiao, L.; Seo, J.-H.; Yui, N.; Ye, S. Surface-restructuring differences between polyrotaxanes and random copolymers in aqueous environment. *Langmuir* **2018,** 34 (41), 12463-12470.
16. Guo, W.; Lu, T.; Crisci, R.; Nagao, S.; Wei, T.; Chen, Z. Determination of protein conformation and orientation at buried solid/liquid interfaces. *Chemical Science* **2023,** 14 (11), 2999-3009.
17. Hong, Y.; Li, Y.; Wang, F.; Zuo, B.; Wang, X.; Zhang, L.; Kawaguchi, D.; Tanaka, K. Enhanced Thermal Stability of Polystyrene by Interfacial Noncovalent Interactions. *Macromolecules* **2018,** 51 (15), 5620-5627.
18. Li, B.; Andre, J. S.; Chen, X.; Walther, B.; Paradkar, R.; Feng, C.; Tucker, C.; Mohler, C.; Chen, Z. Observing a chemical reaction at a buried solid/solid interface in situ. *Anal. Chem.* **2020,** 92 (20), 14145-14152.

19. Li, Q.; Hua, R.; Chou, K. C. Electronic and Conformational Properties of the Conjugated Polymer MEH-PPV at a Buried Film/Solid Interface Investigated by Two-Dimensional IR−Visible Sum Frequency Generation. *J. Phys. Chem. B* **2008,** 112 (8), 2315-2318.
20. Perry, A.; Neipert, C.; Space, B.; Moore, P. B. Theoretical modeling of interface specific vibrational spectroscopy: Methods and applications to aqueous interfaces. *Chem. Rev.* **2006,** 106 (4), 1234-1258.
21. Zhang, S.; Hsu, L.; Toolis, A.; Li, B.; Zhou, J.; Lin, T.; Chen, Z. Investigation of the atmospheric moisture effect on the molecular behavior of an isocyanate-based primer surface. *Langmuir* **2021,** 37 (43), 12705-12713.
22. Zhang, S.; Wu, G.; Chen, Z. Probing molecular structures at buried solid/solid interfaces involving low-k materials or polymers in situ nondestructively: a review. *Journal of Micro/Nanopatterning, Materials, and Metrology* **2023,** 22 (3), 031202-031202.
23. Tian, C.; Shen, Y. Recent progress on sum-frequency spectroscopy. *Surf. Sci. Rep.* **2014,** 69 (2-3), 105-131.
24. Zhang, C.; Myers, J. N.; Chen, Z. Molecular Behavior at Buried Epoxy/Poly(ethylene terephthalate) Interface. *Langmuir* **2014,** 30 (42), 12541-12550.
25. Nguyen, H. K.; Sugimoto, S.; Konomi, A.; Inutsuka, M.; Kawaguchi, D.; Tanaka, K. Dynamics Gradient of Polymer Chains near a Solid Interface. *ACS Macro Letters* **2019,** 8 (8), 1006-1011.
26. Perry, A.; Neipert, C.; Space, B.; Moore, P. B. Theoretical Modeling of Interface Specific Vibrational Spectroscopy: Methods and Applications to Aqueous Interfaces. *Chem. Rev.* **2006,** 106 (4), 1234-1258.
27. Ge, A.; Qiao, L.; Seo, J. H.; Yui, N.; Ye, S. Surface-Restructuring Differences between Polyrotaxanes and Random Copolymers in Aqueous Environment. *Langmuir* **2018,** 34 (41), 12463-12470.
28. Ding, B.; Panahi, A.; Ho, J.-J.; Laaser, J. E.; Brooks III, C. L.; Zanni, M. T.; Chen, Z. Probing site-specific structural information of peptides at model membrane interface in situ. *J. Am. Chem. Soc.* **2015,** 137 (32), 10190-10198.
29. Ge, A.; Matsusaki, M.; Qiao, L.; Akashi, M.; Ye, S. Salt Effects on Surface Structures of Polyelectrolyte Multilayers (PEMs) Investigated by Vibrational Sum Frequency Generation (SFG) Spectroscopy. *Langmuir* **2016,** 32 (16), 3803-3810.
30. Wei, S.; Zou, X.; Tian, J.; Huang, H.; Guo, W.; Chen, Z. Control of Protein Conformation and Orientation on Graphene. *J. Am. Chem. Soc.* **2019,** 141 (51), 20335-20343.
31. Peng, Q.; Chen, J.; Ji, H.; Morita, A.; Ye, S. Origin of the Overpotential for the Oxygen Evolution Reaction on a Well-Defined Graphene Electrode Probed by in Situ Sum Frequency Generation Vibrational Spectroscopy. *J. Am. Chem. Soc.* **2018,** 140 (46), 15568-15571.
32. Barry, M. E.; Davidson, E. C.; Zhang, C.; Patterson, A. L.; Yu, B.; Leonardi, A. K.; Duzen, N.; Malaviya, K.; Clarke, J. L.; Finlay, J. A.; Clare, A. S.; Chen, Z.; Ober, C. K.; Segalman, R. A. The Role of Hydrogen Bonding in Peptoid-Based Marine Antifouling Coatings. *Macromolecules* **2019,** 52 (3), 1287-1295.
33. Yang, C. S. C.; Wilson, P. T.; Richter, L. J. Structure of Polystyrene at the Interface with Various Liquids. *Macromolecules* **2004,** 37 (20), 7742-7746.
34. Xiao, M.; Wei, S.; Chen, J.; Tian, J.; Brooks Iii, C. L.; Marsh, E. N. G.; Chen, Z. Molecular Mechanisms of Interactions between Monolayered Transition Metal Dichalcogenides and Biological Molecules. *J. Am. Chem. Soc.* **2019,** 141 (25), 9980-9988.

35. Chen, Z. Investigating Buried Polymer Interfaces Using Sum Frequency Generation Vibrational Spectroscopy. *Prog. Polym. Sci.* **2010,** 35 (11), 1376-1402.
36. Ye, S.; Tong, Y.; Ge, A.; Qiao, L.; Davies, P. B. Interfacial Structure of Soft Matter Probed by SFG Spectroscopy. *Chem. Rec.* **2014,** 14 (5), 791-805.
37. Xiao, M.; Lu, T.; Lin, T.; Andre, J. S.; Chen, Z. Understanding Molecular Structures of Buried Interfaces in Halide Perovskite Photovoltaic Devices Nondestructively with Sub‐Monolayer Sensitivity Using Sum Frequency Generation Vibrational Spectroscopy. *Advanced Energy Materials* **2019**, 1903053.
38. Tan, J.; Zhang, J.; Li, C.; Luo, Y.; Ye, S. Ultrafast Energy Relaxation Dynamics of Amide I Vibrations Coupled with Protein-Bound Water Molecules. *Nat Commun* **2019,** 10 (1), 1010.
39. Lu, X.; Li, D.; Kristalyn, C. B.; Han, J.; Shephard, N.; Rhodes, S.; Xue, G.; Chen, Z. Directly Probing Molecular Ordering at the Buried Polymer/Metal Interface. *Macromolecules* **2009,** 42 (22), 9052-9057.
40. Wu, B.; Wang, X.; Yang, J.; Hua, Z.; Tian, K.; Kou, R.; Zhang, J.; Ye, S.; Luo, Y.; Craig, V. S. J.; Zhang, G.; Liu, G. Reorganization of Hydrogen Bond Network Makes Strong Polyelectrolyte Brushes pH-Responsive. *Science Advances* **2016,** 2 (8), e1600579.
41. Kubota, J.; Domen, K. Study of The Dynamics of Surface Molecules by Time-Resolved Sum-Frequency Generation Spectroscopy. *Anal. Bioanal. Chem.* **2007,** 388 (1), 17-27.
42. Li, X.; Lu, X. Interfacial Irreversibly and Loosely Adsorbed Layers Abide by Different Evolution Dynamics. *ACS Macro Letters* **2019,** 8 (11), 1426-1431.
43. Chen, C.; Even, M. A.; Chen, Z. Detecting Molecular-Level Chemical Structure and Group Orientation of Amphiphilic PEO−PPO−PEO Copolymers at Solution/Air and Solid/Solution Interfaces by SFG Vibrational Spectroscopy. *Macromolecules* **2003,** 36 (12), 4478-4484.
44. Tan, J.; Zhang, B.; Luo, Y.; Ye, S. Ultrafast Vibrational Dynamics of Membrane-Bound Peptides at the Lipid Bilayer/Water Interface. *Angew. Chem. Int. Ed. Engl.* **2017,** 56 (42), 12977-12981.
45. Leng, C.; Hung, H. C.; Sun, S.; Wang, D.; Li, Y.; Jiang, S.; Chen, Z. Probing the Surface Hydration of Nonfouling Zwitterionic and PEG Materials in Contact with Proteins. *ACS Appl. Mater. Interfaces* **2015,** 7 (30), 16881-16888.
46. Lambert, A. G.; Davies, P. B.; Neivandt, D. J. Implementing the Theory of Sum Frequency Generation Vibrational Spectroscopy: A Tutorial Review. *Appl. Spectrosc. Rev.* **2005,** 40 (2), 103-145.
47. Yan, E. C.; Fu, L.; Wang, Z.; Liu, W. Biological Macromolecules at Interfaces Probed by Chiral Vibrational Sum Frequency Generation Spectroscopy. *Chem. Rev.* **2014,** 114 (17), 8471-8498.
48. Li, B.; Chen, L.; Zhang, S.; Tao, Q.; Ma, Y.-H.; Hu, P.; Lu, X.; Chou, K. C.; Chen, Z. Absolute molecular structure of the polystyrene at the buried polystyrene/silica interface and its relationship to dewetting during annealing. *Appl. Surf. Sci.* **2023,** 611, 155715.
49. Chen, Z. Surface hydration and antifouling activity of zwitterionic polymers. *Langmuir* **2022,** 38 (15), 4483-4489.
50. Del Grosso, C. A.; Leng, C.; Zhang, K.; Hung, H.-C.; Jiang, S.; Chen, Z.; Wilker, J. J. Surface hydration for antifouling and bio-adhesion. *Chemical Science* **2020,** 11 (38), 10367-10377.
51. Avery, C. W.; Palermo, E. F.; McLaughlin, A.; Kuroda, K.; Chen, Z. Investigations of the interactions between synthetic antimicrobial polymers and substrate-supported lipid bilayers using sum frequency generation vibrational spectroscopy. *Anal. Chem.* **2011,** 83 (4), 1342-1349.

52. Vázquez, A. V.; Holden, B.; Kristalyn, C.; Fuller, M.; Wilkerson, B.; Chen, Z. Surface and buried interfacial structures of epoxy resins used as underfills studied by sum frequency generation vibrational spectroscopy. *ACS Appl. Mater. Interfaces* **2011,** 3 (5), 1640-1651.
53. Halden, R. U. Plastics and health risks. *Annual review of public health* **2010,** 31, 179-194.
54. Hopewell, J.; Dvorak, R.; Kosior, E. Plastics recycling: challenges and opportunities. *Philosophical Transactions of the Royal Society B: Biological Sciences* **2009,** 364 (1526), 2115-2126.
55. Millican, J. M.; Agarwal, S. Plastic Pollution: A Material Problem? *Macromolecules* **2021,** 54 (10), 4455-4469.
56. Shang, J.; Chai, M.; Zhu, Y. Photocatalytic degradation of polystyrene plastic under fluorescent light. *Environmental science & technology* **2003,** 37 (19), 4494-4499.
57. Bayo, J.; Rojo, D.; Olmos, S. Weathering indices of microplastics along marine and coastal sediments from the harbor of Cartagena (Spain) and its adjoining urban beach. *Mar. Pollut. Bull.* **2022,** 178, 113647.
58. Lebreton, L. C. M.; van der Zwet, J.; Damsteeg, J. W.; Slat, B.; Andrady, A.; Reisser, J. River plastic emissions to the world's oceans. *Nat Commun* **2017,** 8, 15611.
59. Al-Maaded, M.; Madi, N. K.; Kahraman, R.; Hodzic, A.; Ozerkan, N. G. An Overview of Solid Waste Management and Plastic Recycling in Qatar. *J. Polym. Environ.* **2011,** 20 (1), 186-194.
60. Chamas, A.; Moon, H.; Zheng, J.; Qiu, Y.; Tabassum, T.; Jang, J. H.; Abu-Omar, M.; Scott, S. L.; Suh, S. Degradation Rates of Plastics in the Environment. *ACS Sustainable Chemistry & Engineering* **2020,** 8 (9), 3494-3511.
61. Geyer, R.; Jambeck, J. R.; Law, K. L. Production, use, and fate of all plastics ever made. *Science advances* **2017,** 3 (7), e1700782.
62. Lebreton, L.; Andrady, A. Future scenarios of global plastic waste generation and disposal. *Palgrave Communications* **2019,** 5 (1), 1-11.
63. Shen, L.; Worrell, E., Plastic Recycling. In *Handbook of Recycling*, 2014; pp 179-190.
64. Iovino, R.; Zullo, R.; Rao, M. A.; Cassar, L.; Gianfreda, L. Biodegradation of poly(lactic acid)/starch/coir biocomposites under controlled composting conditions. *Polym. Degrad. Stab.* **2008,** 93 (1), 147-157.
65. Brewis, D.; Briggs, D. Adhesion to polyethylene and polypropylene. *Polymer* **1981,** 22 (1), 7-16.
66. Demirors, M., The history of polyethylene. In *100+ Years of Plastics. Leo Baekeland and Beyond*, ACS Publications: 2011; pp 115-145.
67. McDaniel, M. P.; DesLauriers, P. J., Ethylene Polymers, HDPE. In *Kirk-Othmer Encyclopedia of Chemical Technology*, 2015; pp 1-40.
68. Pathak, V. M.; Navneet. Review on the current status of polymer degradation: a microbial approach. *Bioresources and Bioprocessing* **2017,** 4 (1), 1-31.
69. Harshvardhan, K.; Jha, B. Biodegradation of low-density polyethylene by marine bacteria from pelagic waters, Arabian Sea, India. *Mar. Pollut. Bull.* **2013,** 77 (1-2), 100-106.
70. Restrepo-Flórez, J.-M.; Bassi, A.; Thompson, M. R. Microbial degradation and deterioration of polyethylene – A review. *International Biodeterioration & Biodegradation* **2014,** 88, 83-90.
71. Martínez, K. I.; González‐Mota, R.; Soto‐Bernal, J. J.; Rosales‐Candelas, I. Evaluation by IR spectroscopy of the degradation of different types of commercial polyethylene

exposed to UV radiation and domestic compost in ambient conditions. *J. Appl. Polym. Sci.* **2021,** 138 (14), 50158.
72. Heimowska, A. Environmental Degradation of Oxo-Biodegradable Polyethylene Bags. *Water* **2023,** 15 (23),
73. Zbyszewski, M.; Corcoran, P. L. Distribution and Degradation of Fresh Water Plastic Particles Along the Beaches of Lake Huron, Canada. *Water, Air, & Soil Pollution* **2011,** 220 (1-4), 365-372.
74. Gauthier, E.; Nikolić, M.; Truss, R.; Laycock, B.; Halley, P. Effect of soil environment on the photo‐degradation of polyethylene films. *J. Appl. Polym. Sci.* **2015,** 132 (39),
75. Geetha, R.; Torikai, A.; Nagaya, S.; Fueki, K. Photo-oxidative degradation of polyethylene: Effect of polymer characteristics on chemical changes and mechanical properties. Part 1—Quenched polyethylene. *Polym. Degrad. Stab.* **1987,** 19 (3), 279-292.
76. Martin, L. K.; Yang, C. Q. Infrared spectroscopy studies of the photooxidation of a polyethylene nonwoven fabric. *Journal of environmental polymer degradation* **1994,** 2, 153-160.
77. Rodriguez, A. K.; Mansoor, B.; Ayoub, G.; Colin, X.; Benzerga, A. A. Effect of UV-aging on the mechanical and fracture behavior of low density polyethylene. *Polym. Degrad. Stab.* **2020,** 180, 109185.
78. Bonhomme, S.; Cuer, A.; Delort, A. M.; Lemaire, J.; Sancelme, M.; Scott, G. Environmental biodegradation of polyethylene. *Polym. Degrad. Stab.* **2003,** 81 (3), 441-452.
79. Gardette, M.; Perthue, A.; Gardette, J.-L.; Janecska, T.; Földes, E.; Pukánszky, B.; Therias, S. Photo- and thermal-oxidation of polyethylene: Comparison of mechanisms and influence of unsaturation content. *Polym. Degrad. Stab.* **2013,** 98 (11), 2383-2390.
80. Therias, S.; Rapp, G.; Masson, C.; Gardette, J.-L. Limits of UV-light acceleration on the photooxidation of low-density polyethylene. *Polym. Degrad. Stab.* **2021,** 183,
81. Xingzhou, H. Wavelength sensitivity of photo-oxidation of polyethylene. *Polym. Degrad. Stab.* **1997,** 55 (2), 131-134.
82. Skariyachan, S.; Patil, A. A.; Shankar, A.; Manjunath, M.; Bachappanavar, N.; Kiran, S. Enhanced polymer degradation of polyethylene and polypropylene by novel thermophilic consortia of Brevibacillus sps. and Aneurinibacillus sp. screened from waste management landfills and sewage treatment plants. *Polym. Degrad. Stab.* **2018,** 149, 52-68.
83. Ghosh, S. K.; Pal, S.; Ray, S. Study of microbes having potentiality for biodegradation of plastics. *Environmental Science and Pollution Research* **2013,** 20, 4339-4355.
84. Restrepo-Flórez, J.-M.; Bassi, A.; Thompson, M. R. Microbial degradation and deterioration of polyethylene–A review. *International Biodeterioration & Biodegradation* **2014,** 88, 83-90.
85. Roy, P.; Titus, S.; Surekha, P.; Tulsi, E.; Deshmukh, C.; Rajagopal, C. Degradation of abiotically aged LDPE films containing pro-oxidant by bacterial consortium. *Polym. Degrad. Stab.* **2008,** 93 (10), 1917-1922.
86. Sanniyasi, E.; Gopal, R.; Gunasekar, D.; Raj, P., Biodegradation of low-density polyethylene (LDPE) sheet by microalga. Uronema africanum Borge Sci Rep 11 (1): 17233. 2021.
87. Sarmah, P.; Rout, J. Efficient biodegradation of low-density polyethylene by cyanobacteria isolated from submerged polyethylene surface in domestic sewage water. *Environmental Science and Pollution Research* **2018,** 25, 33508-33520.
88. Sen, S. K.; Raut, S. Microbial degradation of low density polyethylene (LDPE): A review. *Journal of Environmental Chemical Engineering* **2015,** 3 (1), 462-473.

89. Wróbel, M.; Szymańska, S.; Kowalkowski, T.; Hrynkiewicz, K. Selection of microorganisms capable of polyethylene (PE) and polypropylene (PP) degradation. *Microbiol. Res.* **2023,** 267, 127251.
90. Kim, M. Evaluation of degradability of hydroxypropylated potato starch/polyethylene blend films. *Carbohydr. Polym.* **2003,** 54 (2), 173-181.
91. Lee, B.; Pometto III, A. L.; Fratzke, A.; Bailey Jr, T. B. Biodegradation of degradable plastic polyethylene by Phanerochaete and Streptomyces species. *Applied and Environmental Microbiology* **1991,** 57 (3), 678-685.
92. Shah, A. A.; Hasan, F.; Hameed, A.; Ahmed, S. Biological degradation of plastics: a comprehensive review. *Biotechnol. Adv.* **2008,** 26 (3), 246-265.
93. Sivan, A.; Szanto, M.; Pavlov, V. Biofilm development of the polyethylene-degrading bacterium Rhodococcus ruber. *Appl. Microbiol. Biotechnol.* **2006,** 72, 346-352.
94. Upreti, M.; Srivastava, R. A potential Aspergillus species for biodegradation of polymeric materials. *Current science* **2003,** 84 (11), 1399-1402.
95. Aboulkas, A.; El Bouadili, A. Thermal degradation behaviors of polyethylene and polypropylene. Part I: Pyrolysis kinetics and mechanisms. *Energy Convers. Manage.* **2010,** 51 (7), 1363-1369.
96. Arnett, R. L.; Stacy, C. J. Kinetics of the thermal degradation of linear polyethylene. *Polymer Engineering & Science* **1966,** 6 (4), 295-298.
97. Jellinek, H. Thermal degradation of polystyrene and polyethylene. Part III. *Journal of Polymer Science* **1949,** 4 (1), 13-36.
98. Murata, K.; Sato, K.; Sakata, Y. Effect of pressure on thermal degradation of polyethylene. *J. Anal. Appl. Pyrolysis* **2004,** 71 (2), 569-589.
99. Ranzi, E.; Dente, M.; Faravelli, T.; Bozzano, G.; Fabini, S.; Nava, R.; Cozzani, V.; Tognotti, L. Kinetic modeling of polyethylene and polypropylene thermal degradation. *J. Anal. Appl. Pyrolysis* **1997,** 40, 305-319.
100. Zong, R.; Wang, Z.; Liu, N.; Hu, Y.; Liao, G. Thermal degradation kinetics of polyethylene and silane‐crosslinked polyethylene. *J. Appl. Polym. Sci.* **2005,** 98 (3), 1172-1179.
101. Lomakin, S.; Rogovina, S.; Grachev, A.; Prut, E.; Alexanyan, C. V. Thermal degradation of biodegradable blends of polyethylene with cellulose and ethylcellulose. *Thermochim. Acta* **2011,** 521 (1-2), 66-73.
102. Hakkarainen, M.; Albertsson, A.-C. Environmental degradation of polyethylene. *Long term properties of polyolefins* **2004**, 177-200.

Chapter 2 Nondestructive in Situ Detection of Chemical Reactions at the Buried Interface between Polyurethane and Isocyanate-Based Primer

Adapted with permission from "Zhang, S.; Andre, J. S.; Hsu, L.; Toolis A.; Esarey, S. J.; Li, B.; Chen, Z. Nondestructive In Situ Detection of Chemical Reactions at the Buried Interface between Polyurethane and Isocyanate-Based Primer. *Macromolecules*, 2020, 53(22), 10189-10197". Copyright 2020 American Chemical Society.

S.Z. contributed to investigation, methodology, data analysis and writing. J.S.A. and B.L. provided assistance on experiments. L.H. contributed to investigation, methodology, analysis and editing. A.T., S.J.E. contributed to investigation and editing. Z.C. contributed to conceptualization, methodology, supervision and editing.

2.1 Introduction

Potting compounds and sealants are generally designed for encapsulation of a wide variety of substrates, protecting them from changes induced by environmental exposure such as physical weathering, chemicals, temperature, and moisture. Among different kinds of potting compounds and sealants, polyurethanes represent a highly demanded category featuring outstanding flexibility, exceptional cryogenic properties, excellent abrasion resistance, advantageous cost, and easily adjustable formulations.[1-4] These strengths allow polyurethanes to be extensively utilized in common household products in a variety of booming industries.

After application to a substrate, the polyurethanes are cured and adhesion takes place at the interface.[5] To improve adhesion properties, they are usually paired with isocyanate-based primers or adhesion promoters. **Figure 2.1** shows a schematic of a polyurethane potting compound (PPC) applied on a primer-coated substrate. The adhesion efficiency of PPC can be promoted by the primer pre-coated on the substrate surface; the latter also helps achieve other desirable benefits such as improvement in wettability and corrosion inhibition.[1,6,7] Despite the significant role of the primer, little direct evidence has been shown to demonstrate the fundamental mechanism of adhesion enhancement at the interface between primer and PPC. Understanding such knowledge would assist in establishing critical design principles for developing polymeric materials with enhanced interfacial properties targeting specialty applications. A strong research impetus to understand structure-function (e.g., mechanical performance) correlations has been stimulated by the growing needs of industries.

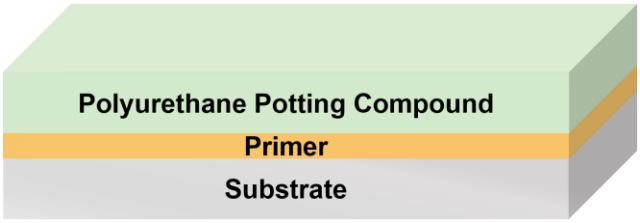


Figure 2.1 Schematic showing a polyurethane potting compound (PPC) on a primed substrate in a real application.

Historically, several theories of adhesion have been postulated, as introduced in Chapter 1.[1,8-11] It is believed that active isocyanate groups in the primers are associated with adhesion properties at interfaces through possible interactions that include chemical reactions, the formation of hydrogen bonding and/or interactions of polar functionalities.[12]

Recent studies provide insights by investigating adhesion mechanisms between isocyanates and different kinds of substrates, such as aluminum, gold, copper, steel and epoxy

resin surfaces.[13-20] Although both experimental tests and modeling have been utilized, most existing knowledge is established on select model compounds and/or limited by the incapability of characterizing molecular structures directly and selectively at the buried interfaces. Thereby, the nature of a buried interface involving isocyanate functionality needs further investigation, especially for practical systems containing more diversified and multifunctional structures.

SFG works as a suitable tool to study the molecular structure at buried interfaces in this study. SFG investigations on polyurethanes, especially in terms of their adhesion mechanism, were sparse despite their significance and broad applications. Previous SFG studies on polyurethane materials focused on the surface structures in air or surface structure changes when in contact with water and protein solutions.[21-24] Up until our research, the adhesion of polyurethanes especially when adhering to primers at the buried solid/solid interface had not yet been studied in detail with SFG. Here we aimed to provide direct evidence of the interfacial molecular interactions via SFG to uncover their adhesion mechanism.

In this study, both the primer and the PPC examined are commercial products commonly used to investigate adhesion in real applications. This also enables a correlation built up directly between interfacial molecular structures and practical mechanical performance, which was measured by 180°peel tests in this study. The applied primer PR-420 contains various molecules with isocyanate (-NCO) groups, organic solvents, and some inorganic additives. On the other hand, the PPC is a two-part, chemically curing polyurethane system containing amine functionality. ATR-FTIR was also used in this research to determine the general bulk molecular spectroscopic features of the primer and the PPC.

The SFG study first focused on the molecular behaviors of the isocyanate groups (-NCO) at the buried interfaces. The results indicate that through the adhesion process, isocyanate groups

of the primer at the interface were consumed by their reaction to amino groups in the PPC. This interfacial reaction contributed to chemical bonding between the primer and the PPC and resulted in adhesion enhancement revealed by the mechanical tests. The urea bonds were also detected by SFG as the product of the interfacial reaction. To the best of our knowledge, this is the first study to observe the chemical reaction in situ nondestructively at the buried solid/solid interface of the isocyanate family. This research also provides a general approach that SFG can be used to probe interfacial chemical reactions related to a broad area of materials applications in the future.

2.2 Materials and Methods

2.2.1 Materials

Calcium fluoride (CaF_2) prisms were ordered from Altos Photonics, Inc. (Bozeman, MT). The commercial primer (PR-420A, PR-420B) and the PPC (PR-1547A, PR-1547B) were obtained from PPG Inc. (Pittsburgh, PA). Methyl ethyl ketone (MEK) was purchased from Sigma-Aldrich, Inc. (Burlington, MA). All materials were used as received.

2.2.2 Sample Preparation

For both the primer and the PPC, the mass ratios of parts A and B in this study are the same as those in practical use. Meanwhile, the annealing procedures were performed in accordance with the technical instructions in practical use. The primer is an opaque, orange-colored liquid formulated by a mixing ratio of 13.7 parts of primer part A and 100 parts of primer part B by mass. The PPC was made by a mixture of 32 parts of PPC part A and 100 parts of PPC part B by mass. The PPC is viscous, typically ranging up to 450 Poise measured via a Brookfield viscometer using a #5 spindle at 10 rpm.

Samples for 180°peel tests were prepared as performed in practical use. The primer was applied to the substrate by brush and allowed to dry for approximately 1 hour at ambient temperature. The PPC was manually applied to the primed substrate (or substrate) using a spatula. For SFG experiments, in order to ensure that the input beams can reach the interface between the primer and PPC (**Figure 2.2**), a thin primer (or PPC) layer on the prism was prepared by spin-coating, and then PPC (or primer) was manually applied on top of the layer to create the buried interface. Since the sample compositions and annealing procedures were adopted in accordance with the technical instructions in practical use, the interfaces for SFG experiments are believed to serve as good models for understanding primer-PPC interactions. To make a thin primer film, a 2 wt% primer MEK solution was prepared. MEK was selected as the solvent because its volatility makes it easily evaporate from the thin film. In addition, it has no characteristic peaks in our targeted spectral frequency region, and MEK is not reactive with components in either the primer or the PPC. The primer solution was spin-coated onto a pre-cleaned calcium fluoride (CaF_2) prism at 4000 rpm for 1 min using a P-6000 spin coater (Speedline Technologies, Franklin, MA). The spin-coated film was dried at room temperature for 60 min followed by PPC cast onto the primed prism. The sample was degassed and cured at 82 °C for 16 hours under a nitrogen atmosphere. In the control experiments (**Figure 2.6a**), the PPC was made and cured as described above on a glass microscope slide. The cured PPC was then peeled from the slide and placed against the primer-coated prism to make a primer/PPC interface for testing. A different sample system was also prepared to study the interface between the primer and the PPC by SFG. Instead of using primer (on CaF_2) in contact with a PPC bulk, a thin PPC layer was made by spin coating on CaF_2 and was placed in contact with a thick primer bulk material to create a PPC/primer interface for study. The

thickness of the primer film and the PPC film were measured by using a Dektak depth profilometer with an average of around 30 nm and around 100 nm, respectively.

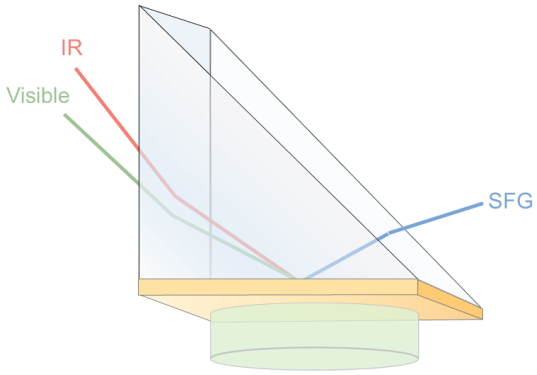


Figure 2.2 Schematic showing an SFG sample geometry used in this study to collect SFG spectra from the buried primer (orange layer)/PPC (green cylinder) interface.

2.2.3 ATR-FTIR Experiments

ATR-FTIR was used as a supplemental tool in this study. ATR-FTIR spectra were collected with a Nicolet iS50 (Thermo Fisher Scientific, Waltham, MA) spectrometer controlled by OMNIC software from the dried primer or the cured PPC in contact with the ATR crystal.

2.2.4 Peel Tests (180°)

Peel tests (180°) involve stripping away the PPC by a moving jaw from the fixed aluminum substrate. Samples were prepared by initially abrading and degreasing a 3” x 6” metal substrate, followed by priming the surface with PR-420 and then subsequent application of the PPC in accordance with manufacturer’s instructions. Two 1” x 12” primer-coated strips of metal mesh were placed in parallel on the sample area to enable a sample number of 2 per panel. The samples were cut into two 1” wide strips, lengthwise over the mesh. The peel strength as measured in pounds per linear inch (pli) was determined using an Instron 3345 machine, using a pull rate of 2

inches/min. The specimen is peeled at an angle of l80°. The 180° peel tests were performed at PPG by our collaborators.

2.3 Results and Discussion

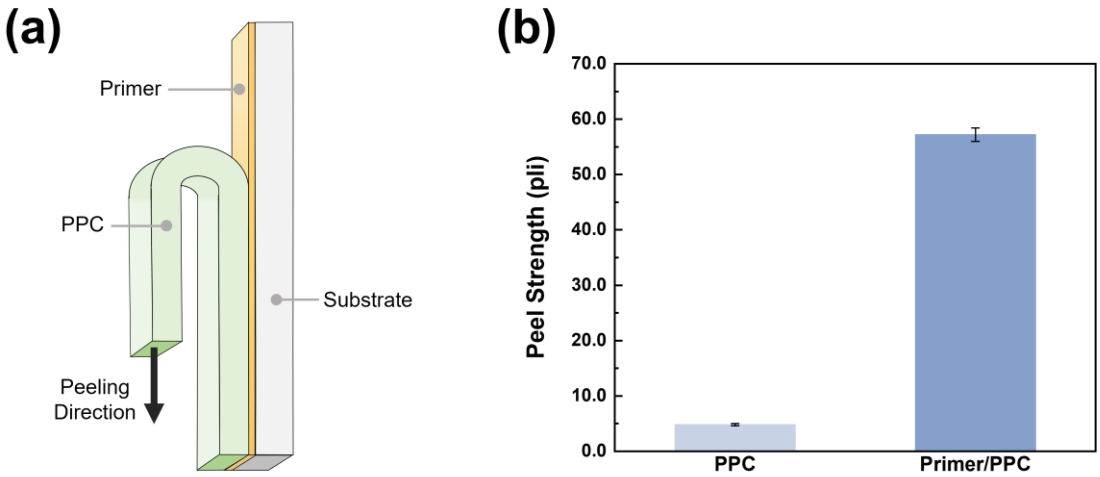


Figure 2.3 (a) Schematic showing the 180° peel strength test. (b) Results of 180° peel tests.

Peel tests (180°) were conducted first to characterize macroscopic interfacial adhesion strength in our system.[4] **Figure 2.3a** illustrates a schematic to show the 180° peel test performed in this study. **Figure 2.3b** displays the results of the PPC peeled in the same fashion from a pristine aluminum substrate surface and a primer-coated surface of an aluminum substrate, respectively. When the PPC was peeled directly from the substrate surface (the left bar in **Figure 2.3b**), the peel strength on average was as low as 4.8 pli. In contrast, an order-of-magnitude increase in peel strength (57.2 pli) was observed when the PPC was applied to the primer-pretreated surface (the right bar in **Figure 2.3b**). The adhesion data demonstrates that the presence of primer greatly promoted the adhesion strength of the interface. All the PPC systems were cured at 82°C prior to the peel tests, as done in practical applications.[25] To understand the curing temperature effect, we

attempted to examine samples cured at room temperature. However, those samples failed cohesively before adhesive failure occurred, preventing measurement of the interfacial adhesion strength. Therefore, an 82°C curing process was applied for samples in the following SFG studies to better correlate SFG results to the peel tests. These correlated results will elucidate the interfacial structure-property relationship.

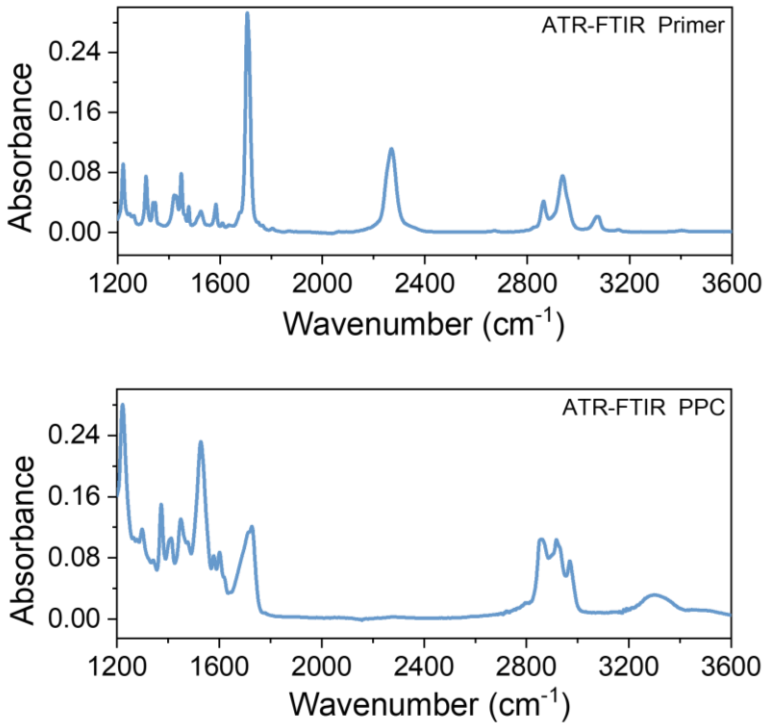


Figure 2.4 ATR-FTIR spectra collected from the primer (top) and the PPC (bottom) in the frequency region of 1200-3600 cm^{-1}.

Differences between the bulk structures of the primer and the PPC can be seen through ATR-FTIR tests (**Figure 2.4**). In the region of 2200-2350 cm^{-1}, a distinct absorption peak was observed in the ATR-FTIR spectrum of the primer (top spectrum in **Figure 2.4**), whereas this peak was not detected in the ATR-FTIR spectrum collected from the PPC (bottom spectrum in **Figure 2.4**). This is the characteristic peak of isocyanate groups in the primer.[26] Signals between 2800 and

3000 cm^{-1} were detected from both samples, contributed by C-H stretching vibrational modes. N-H stretching modes contributed to the peak in the region of 3200-3400 cm^{-1} of the PPC. Many peaks below 1800 cm^{-1} can also be seen from the primer and the PPC. For example, the peak at around 1727 cm^{-1} in the top spectra can be assigned to urethane C=O stretching in the PPC.[27]

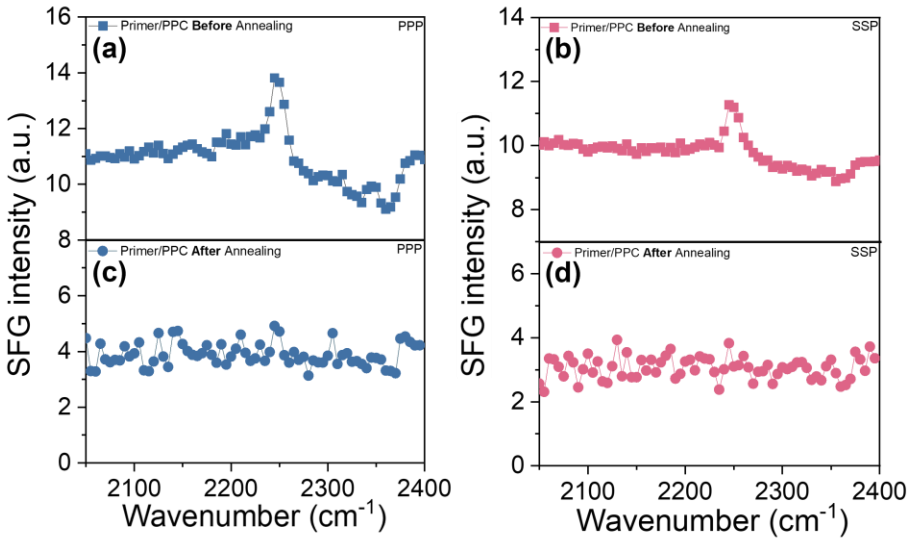


Figure 2.5 SFG ppp (a) and ssp (b) spectra collected from the buried primer/PPC interface before annealing. SFG ppp (c) and ssp (d) spectra collected from the buried primer/PPC interface after annealing.

SFG was then applied to study the buried primer/PPC interface. After the PPC was applied to the primer surface and left uncured, strong ssp and ppp SFG signals from the isocyanate –NCO groups were detected from the buried primer/PPC interface, showing that –NCO groups were present at the interface with order before curing (**Figures 2.5a** and **2.5b**). In contrast, in **Figures 2.5c** and **2.5d**, the strong isocyanate peak disappeared from the primer/PPC interface after the sample was cured at 82°C for 16 hours under N_2. The negative peaks observed in the spectra at around 2350 cm^{-1} are due to CO_2 (in air) absorption of the IR input laser beam. It is worth mentioning that the SFG spectra presented in this work were collected on different days, while the SFG laser performance and the IR input beam intensities could be different. In addition, the CO_2

concentration in the lab environment could fluctuate slightly. Therefore, the negative peaks detected in various spectra are different. All the samples were degassed and cured under a nitrogen atmosphere, which limited the reaction of isocyanate groups with water in air over time. In view of the reactivity of the isocyanate groups, it is very likely that the isocyanate groups in primer at the interface were consumed gradually through a chemical reaction with the PPC. This interfacial reaction led to the disappearance of the SFG signal from the –NCO groups and bonded the two materials together, resulting in adhesion enhancement. Before a conclusion was drawn, more experiments were followed to further verify our hypothesis.

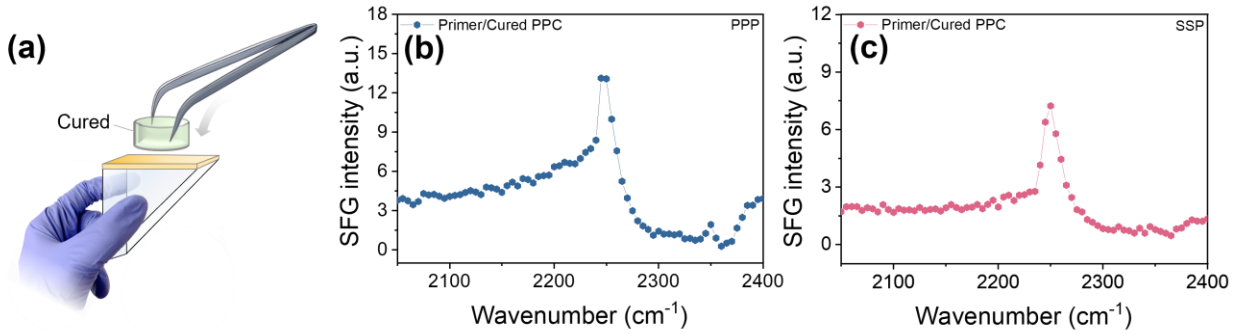


Figure 2.6 (a) Schematic showing the SFG sample preparation process used to collect SFG spectra from the primer/PPC interface after placing a cured PPC sample in contact with primer. SFG ppp (b) and ssp (c) spectra collected from the buried primer/PPC interface after the PPC was cured first and was then placed in contact with the primer.

In view of any possible changes of the PPC itself by curing that may interfere with the detection of -NCO signals at the buried interface, a control experiment was performed by using a similar sample geometry using a different sample preparation method, shown in **Figure 2.6a**. SFG spectra were still collected from an interface between a primer and a PPC, but instead of curing the PPC on the primer surface, a cured PPC was prepared in advance, separate from the primer. This procedure ensures that no interactions with the primer take place at the interface through the

curing process of the PPC. After curing, the PPC was placed against the surface of the primer and analyzed with SFG without further treatment. SFG spectra of the primer/cured PPC interface can be seen in **Figures 2.6b** and **2.6c**. The result shows that the SFG signal contributed from the –NCO group at the primer/cured PPC interface can still be clearly observed, which is different from the SFG spectra collected from the primer/PPC interface when the PPC is cured on the primer surface. The results obtained from this experiment illuminate that the disappearance of the -NCO groups at the buried interface is not induced by the changed state of the PPC itself.

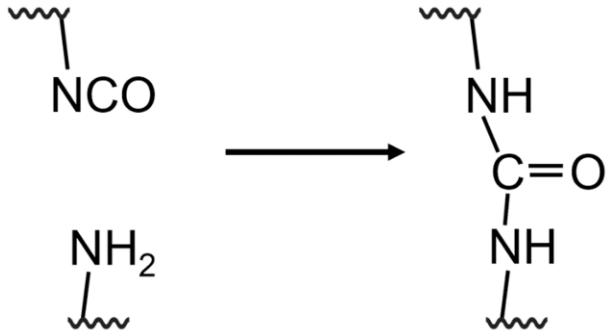


Figure 2.7 Postulated chemical reaction between isocyanate and primary amino groups.

SFG was further applied to probe the primer when placed in contact with each individual component of the PPC. Both PPC Part A and PPC Part B are polyurethane-based precursors, but PPC Part B does not contain amino groups while PPC Part A does. As shown in **Figure 2.7**, it is well known that isocyanate groups favor the reaction with amino groups to form urea bonds.[28] SFG spectra were collected from the buried interface between the primer and the PPC Part B (**Figures 2.8a** and **2.8b**). All procedures and annealing conditions for sample preparations are the same as the samples prepared in **Figure 2.5** except for the omission of PPC Part A from the PPC formulation. In fact, the SFG results are different from those presented in **Figures 2.5c** and **2.5d**. Instead of –NCO signals disappearing at the interface, the spectra show strong SFG signals from

the primer –NCO groups, indicating that isocyanate groups were still present at the primer/PPC Part B interface with order. It is therefore believed that no chemical reaction took place at the interface of the primer samples when only PPC Part B was involved.

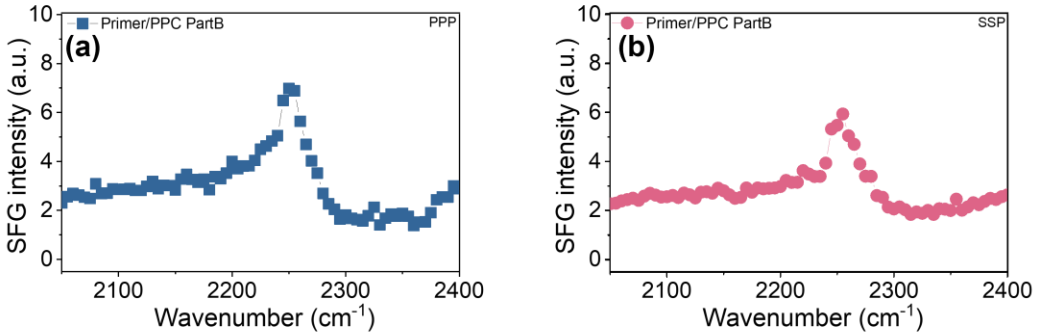


Figure 2.8 SFG ppp (a) and ssp (b) spectra collected from the buried primer/PPC Part B interface after annealing.

To help verify this conclusion, the interface between the primer and the PPC Part A was also studied using the same sample preparation and SFG data collection method. The SFG spectrum of the primer/PPC Part A interface after annealing is shown in **Figure 2.9**. Similar to those collected from the primer/PPC (full formula) interface, the SFG spectrum from the primer/PPC Part A interface after annealing shows the disappearance of the SFG –NCO signals, which is different from the result of the primer/PPC Part B interface after annealing. This experimental result supports our hypothesis that an interfacial reaction occurred between the primer isocyanate groups and the amine functionality within PPC Part A.

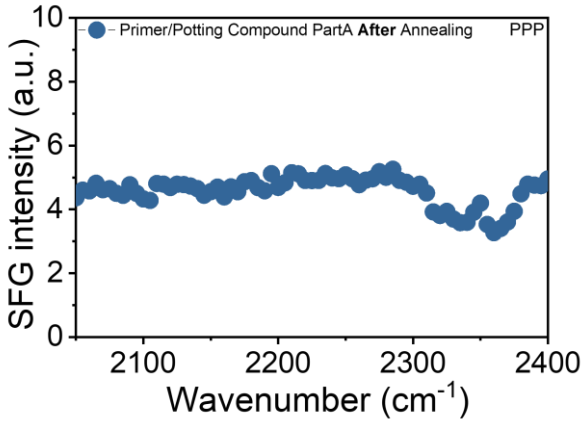


Figure 2.9 SFG ppp spectrum collected from the primer/PPC Part A interface after annealing.

In the above SFG studies at buried interfaces, the thin primer film used has a primer/CaF_2 substrate interface and a primer/PPC interface. If SFG –NCO signal was contributed from the primer/CaF_2 substrate interface, similar SFG signals in this region after annealing should have been observed from the primer/PPC sample, the primer/PPC Part A sample, and the primer/PPC Part B sample. However, such signals observed were not similar. Thus, the SFG –NCO signal is believed to be generated mainly from the primer/PPC interface, not the primer/CaF_2 substrate interface. That is to say, the disappearance of the SFG –NCO signal from the primer/PPC sample (**Figure 2.5**) was not because of the signal changing due to the primer/CaF_2 substrate interface (but due to the interfacial reaction at the primer/PPC interface), otherwise no signal should be observed from the primer/PPC Part B interface as well. To further confirm the reaction at the interface, a different system was used to study the interface between the primer and the PPC by SFG. Instead of using primer (on CaF_2) in contact with a PPC bulk, SFG spectra were collected from PPC (on CaF_2)/primer bulk interface. In this case, the possible SFG signal contribution from the –NCO groups at the interface between the CaF_2 prism and the primer can be eliminated. Similar

to the previous experimental procedures, before the buried interface was analyzed, SFG spectra were collected first from a thin PPC film on CaF_2 in air (**Figures 2.10a** and **2.10b**). No obvious resonant SFG signal of the –NCO groups could be detected from the PPC surface in air. Some non-resonant SFG signals (with CO_2 absorption by the infrared input beam) appeared in the spectra. The buried interface between the PPC (on CaF_2) and primer was then studied. Before the 16-hour annealing process, strong SFG signals from the –NCO groups could be detected from the buried PPC (on CaF_2)/primer interface (**Figures 2.10c** and **2.10d**), showing that the –NCO groups were present at the interface with order. After the annealing process, SFG signals from the –NCO groups were greatly decreased (**Figures 2.10e** and **2.10f**), which can be explained by the consumption of the -NCO groups at the interface. The results obtained from the SFG studies on the PPC/primer interface match those acquired from the above SFG studies.

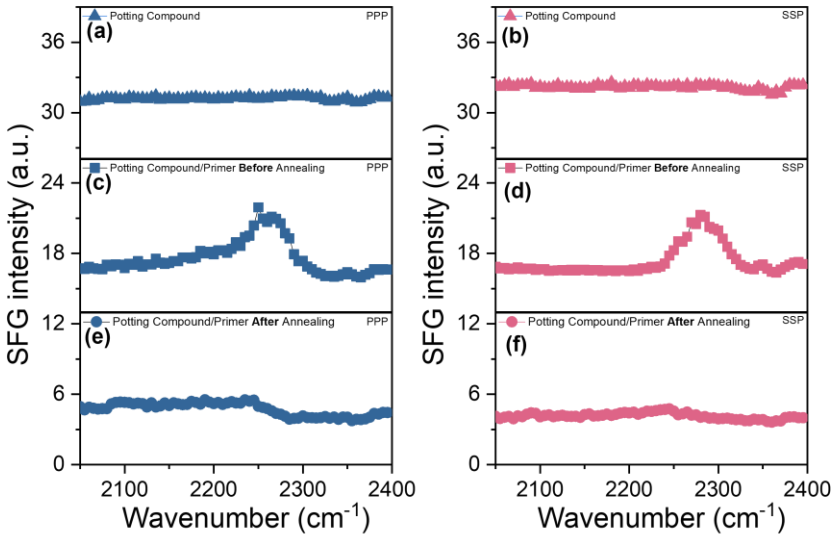


Figure 2.10 The ppp (a) and ssp (b) SFG spectra collected from the PPC (on CaF_2). The ppp (c) and ssp (d) SFG spectra collected from the PPC (on CaF_2)/primer interface before annealing. The ppp (e) and ssp (f) SFG spectra collected from the PPC (on CaF_2)/primer interface after annealing.

Since the chemical reaction at the interface led to the loss of the SFG –NCO signals, attempts were also made to observe the reaction from other regions. In the region above 3000 cm^{-1}, amino groups have characteristic peaks due to the N-H stretching mode. However, in addition to the NH_2 amino groups, N-H bonds in urethane groups are also present in the PPC, which can also contribute to SFG signals in the N-H stretching region. Furthermore, if amino groups were responsible for the interfacial reaction with isocyanate groups, their products from the reaction would also contribute to the N-H stretching signals, which convolutes the signal from the original NH_2 signal before the reaction. This further complicated the interpretation of the N-H stretching signals in the SFG spectra (data not shown). Instead, the formation of the new bonds was probed by SFG in the region of 1500-1700 cm^{-1}. In **Figure 2.11**, the SFG spectra show the PPC, primer and their interface after the annealing process using the same sample geometry for **Figure 2.10**. **Figures 2.11a-d** show that no obvious SFG signal can be detected between 1610 – 1645 cm^{-1}, which agrees with the ATR-FTIR data presented in **Figure 2.4**. The SFG spectra collected from the interface between the PPC and the primer shown in **Figures 2.11e** and **2.11f** exhibit distinguishable signals between 1610 – 1645 cm^{-1}, indicating the existence of ordered H-bonded C=O stretching vibrations from urea structures.[29,30] Different from the urethane bonds, the stretching frequency of the H-bonded urea C=O is lower due to two NH groups connected to the urea C=O group, which avoided the signal confusion from urethane in the C=O stretching frequency region.[28,31] The formation of the urea bonds detected by SFG further confirms the chemical reaction at the buried primer/PPC interface and explains the adhesion enhancement. In addition, the observation of the C=O stretching signal by SFG after annealing also demonstrates that the disappearance of the –NCO signals was not caused by the disappearance of the interface, but by the interfacial chemical reaction.

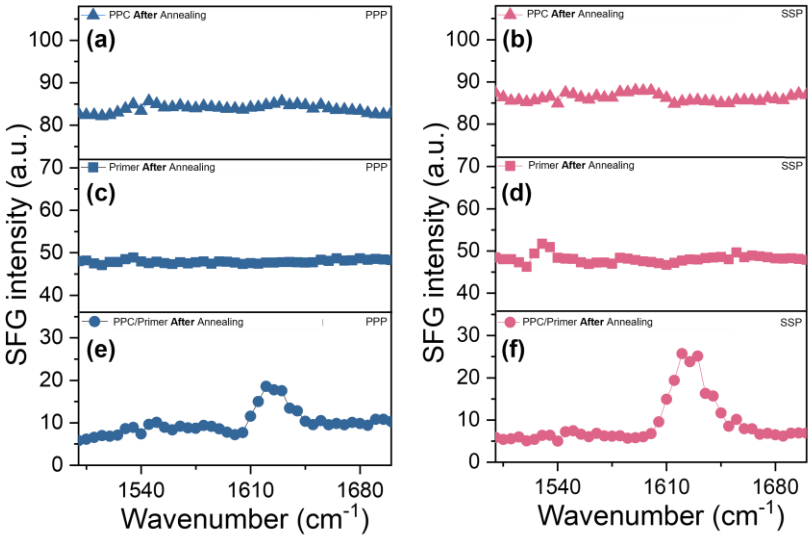


Figure 2.11 SFG ppp and ssp spectra collected from the PPC (a) (b), primer (c) (d) and PPC/primer interfaces (e) (f) after annealing.

2.4 Conclusion

In this work, for the first time, the interfacial reaction of a commercial isocyanate-based primer and a PPC was successfully probed in situ and nondestructively by SFG spectroscopy to study the adhesion mechanism. The SFG signals of –NCO groups in the primer were detected from the buried interface between the primer and the uncured PPC. Such signals disappeared through the curing process, indicating that –NCO groups of the primer were consumed at the interface by the interfacial reaction with the PPC. Other possible factors that might cause the disappearance of the SFG –NCO signal were ruled out from control experiments, since this signal could also be detected from 1) the buried primer film/PPC interface when the bulk PPC was cured in advance and placed against the primer, and 2) a different sample with a PPC film in contact with a primer bulk before annealing. Furthermore, it was found that –NCO signals were only consumed at the

buried interface when amine-containing PPC Part A was included in the formulation. The urea groups, which are the product of the reaction, were detected at the interface after annealing for the first time by SFG as well, further confirming the interfacial reaction. The results indicate that the formed chemical bonds can greatly facilitate the enhancement of the adhesion at the interface between the primer and the PPC.

Other techniques including ATR-FTIR and 180° peel tests were used as supplemental tools in the study to support the conclusion. ATR-FTIR was applied to determine the bulk compositions of the primer and the PPC. 180° peel tests directly show that the adhesion strength of the PPC at the interface is enhanced by the primer, which correlates to the conclusions drawn from the SFG experiments, ultimately connecting the interfacial molecular behavior with the macroscopic adhesion performance.

Understanding interfacial interactions including chemical reactions is important for the rational design of multilayer polymer materials with optimized function and performance. The methodology developed in this study is generally applicable to probe interfacial chemical reactions at buried solid/solid interfaces in situ nondestructively, which can assist in studying a broader area of polymers in the future.

2.5 References

1. Ebnesajjad, S.; Landrock, A. H., *Adhesives technology handbook*. William Andrew: 2014.
2. Dostal, C., Engineered Materials Handbook Volume 2: Engineering Plastic. Metals Park, OH: ASM International: 1988.
3. Edwards, B. H., Polyurethane structural adhesives. In *Structural Adhesives*, Springer: 1986; pp 181-215.
4. Harper, C. A., *Handbook of plastics, elastomers, and composites*. McGraw-Hill New York: 2002; Vol. 4.
5. Adams, R. D., *Adhesive bonding: science, technology and applications*. Elsevier: 2005.

6. Bodnar, M. J.; Arsenal, P. Processing for adhesives bonded structures: held at Stevens Center, Stevens Institute of Techno logy, Hoboken, New Jersey, August 23-25, 1972. **1972**,
7. Chaturvedi, M. C., *Welding and joining of aerospace materials*. Elsevier: 2011.
8. Awaja, F.; Gilbert, M.; Kelly, G.; Fox, B.; Pigram, P. J. Adhesion of polymers. *Prog. Polym. Sci.* **2009,** 34 (9), 948-968.
9. Baldan, A. Adhesion phenomena in bonded joints. *Int. J. Adhes. Adhes.* **2012,** 38, 95-116.
10. Meschut, G.; Janzen, V.; Olfermann, T. Innovative and Highly Productive Joining Technologies for Multi-Material Lightweight Car Body Structures. *J. Mater. Eng. Perform.* **2014,** 23 (5), 1515-1523.
11. Gong, L.; Xiang, L.; Zhang, J.; Chen, J.; Zeng, H. Fundamentals and Advances in the Adhesion of Polymer Surfaces and Thin Films. *Langmuir* **2019,** 35 (48), 15914-15936.
12. Heath, R., Isocyanate-Based Polymers. In *Brydson's Plastics Materials*, 2017; pp 799-835.
13. Dillingham, R. G.; Moriarty, C. The Adhesion of Isocyanate-Based Polymers to Steel. *J. Adhes.* **2010,** 79 (3), 269-285.
14. Fug, F.; Nies, C.; Possart, W. in situ FTIR Study of Adhesive Interactions of 4,4′ -Methylene Diphenyl Diisocyanate and Native Metals. *Int. J. Adhes. Adhes.* **2014,** 52, 66-76.
15. Kim, J.; Cho, J.; Lim, Y.-S. Bonding of Urethane Reactants to Aluminum Surface. *J. Mater. Sci.* **2005,** 40 (11), 2789-2794.
16. Nies, C.; Wehlack, C.; Ehbing, H.; Dijkstra, D. J.; Possart, W. Adhesive Interactions of Polyurethane Monomers with Native Metal Surfaces. *J. Adhes.* **2012,** 88 (8), 665-683.
17. Ramirez, M.; Vargas, J.; Springborg, M. Energetic, Structural, and Vibrational Properties of 4,4'-Methylenediphenyl Diisocyanate with Relevance for Adhesion. *J. Phys. Chem. A* **2016,** 120 (24), 4256-4266.
18. Sensui, K.; Tarui, T.; Miyamae, T.; Sato, C. Evidence of Chemical-Bond Formation at the Interface between an Epoxy Polymer and an Isocyanate Primer. *Chem. Commun. (Camb.)* **2019,** 55 (98), 14833-14836.
19. Shimizu, K.; Phanopoulos, C.; Loenders, R.; Abel, M.-L.; Watts, J. F. The Characterization of the Interfacial Interaction between Polymeric Methylene Diphenyl Diisocyanate and Aluminum: A ToF-SIMS and XPS Study. *Surf. Interface Anal.* **2010,** 42 (8), 1432-1444.
20. Tardio, S.; Abel, M.-L.; Carr, R. H.; Watts, J. F. The Interfacial Interaction between Isocyanate and Stainless Steel. *Int. J. Adhes. Adhes.* **2019,** 88, 1-10.
21. Clarke, M. L.; Wang, J.; Chen, Z. Sum Frequency Generation Studies on the Surface Structures of Plasticized and Unplasticized Polyurethane in Air and in Water. *Anal. Chem.* **2003,** 75 (14), 3275-3280.
22. Clarke, M. L.; Wang, J.; Chen, Z. Conformational Changes of Fibrinogen after Adsorption. *J. Phys. Chem. B* **2005,** 109 (46), 22027-22035.
23. Zhang, D.; Ward, R. S.; Shen, Y. R.; Somorjai, G. A. Environment-Induced Surface Structural Changes of a Polymer: An in Situ IR + Visible Sum-Frequency Spectroscopic Study. *J. Phys. Chem. B* **1997,** 101 (44), 9060-9064.
24. Zhou, J.; Anim-Danso, E.; Zhang, Y.; Zhou, Y.; Dhinojwala, A. Interfacial Water at Polyurethane-Sapphire Interface. *Langmuir* **2015,** 31 (45), 12401-12407.
25. TECHNICAL DATA: PR-1547 Potting And Molding Compound. *PPG*,
26. Zhang, L.; Rowan, S. J. Effect of Sterics and Degree of Cross-Linking on the Mechanical Properties of Dynamic Poly(alkylurea–urethane) Networks. *Macromolecules* **2017,** 50 (13), 5051-5060.

27. Jiang, H.; Ye, L.; Wang, Y.; Ma, L.; Cui, D.; Tang, T. Synthesis and Characterization of Polypropylene-Based Polyurethanes. *Macromolecules* **2020,** 53 (9), 3349-3357.
28. Zhang, S.; Ren, Z.; He, S.; Zhu, Y.; Zhu, C. FTIR Spectroscopic Characterization of Polyurethane-Urea Model Hard Segments (PUUMHS) Based on Three Diamine Chain Extenders. *Spectrochim. Acta. A Mol. Biomol. Spectrosc.* **2007,** 66 (1), 188-193.
29. Wu, C.; Wang, J.; Chang, P.; Cheng, H.; Yu, Y.; Wu, Z.; Dong, D.; Zhao, F. Polyureas from Diamines and Carbon Dioxide: Synthesis, Structures and Properties. *Phys. Chem. Chem. Phys.* **2012,** 14 (2), 464-468.
30. Mattia, J.; Painter, P. A Comparison of Hydrogen Bonding and Order in a Polyurethane and Poly(urethane−urea) and Their Blends with Poly(ethylene glycol). *Macromolecules* **2007,** 40 (5), 1546-1554.
31. Yilgor, I.; Yilgor, E.; Guler, I. G.; Ward, T. C.; Wilkes, G. L. FTIR Investigation of the Influence of Diisocyanate Symmetry on the Morphology Development in Model Segmented Polyurethanes. *Polymer* **2006,** 47 (11), 4105-4114.

Chapter 3 Investigation of Atmospheric Moisture Effect on the Molecular Behavior of Isocyanate-Based Primer Surface

Adapted with permission from "Zhang, S.; Hsu, L.; Toolis A.; Li, B.; Zhou, J.; Lin, T.; Chen, Z. Investigation of Atmospheric Moisture Effect on the Molecular Behavior of Isocyanate-Based Primer Surface. Langmuir, 2021, 37 (43), 12705–12713". Copyright 2021 American Chemical Society.

S.Z. contributed to investigation, methodology, data analysis and writing. L.H. contributed to investigation, methodology, analysis and editing. A.T. contributed to investigation and editing. B.L., J.Z, and T.L. provided assistance on experiments. Z.C. contributed to conceptualization, methodology, supervision and editing.

3.1 Introduction

As detailed in Chapter 2, primers are applied to substrate surfaces as an intermediate layer prior to the application of a subsequent coating and are capable of providing improved adhesion properties between the substrate and the coating.[1-5]

Isocyanate-based primers are oftentimes advised to be applied, then top coated by the next product within a specified timeframe to ensure proper bonding, since adhesion properties change over time. An appreciably lower degree of adhesion enhancement can occur if primers are applied and not top coated within the recommended period of time. When topcoating is not accomplished

within the recommended open time, one solution recommended by the industry is to repeat the priming procedure, and the adhesion ability is thus ameliorated by the freshly primed surface. In some cases, additional work is needed regarding completely stripping off the primer before repeating priming. However, the surface molecular behavior behind the reduced adhesion performance of primer over time has not been fully investigated. There is industry interest in observing the molecular changes at the primer surface. Understanding the molecular behavior of the primer surface with time can provide insights into this phenomenon, assisting in future product development and clarification of customer product use guidelines.

Chapter 2 confirmed the formation of chemical bonding at the buried primer/potting compound interface, which contributed to the enhanced adhesion performance. As the key functional groups that participated in the interfacial reaction, isocyanates play an essential role in the adhesion efficiency of the primer. Meanwhile, adhesion is a surface phenomenon,[6,7] thus it is imperative to preserve the chemical activity of these surface isocyanate groups before application of the potting compound to achieve desired adhesion performances. Isocyanates are known to be highly reactive and can easily interact with active hydrogen sources.[8-12] After they are applied to their exposed surfaces, isocyanate-based primers are likely to face potential challenges from the environment that possesses active hydrogen-containing reactants. Atmospheric moisture could be one challenge that affects their performance. Although the reaction between isocyanate and water (**Figure 3.1**) is beneficial when producing polyurethane foam in manufacturing where water functions as a chemical blowing agent,[8,13-15] it becomes undesirable for isocyanate-based primers, as the reaction could reduce or minimize the activity of isocyanates, diminishing its ability to further react with functional groups in adhesives or other products at the interface. Thus, the surface of an isocyanate-containing material could be vulnerable in the atmosphere. Extensive

research was carried out to study a variety of subjects involving the reaction between isocyanates and water,[16-23] whereas in situ surface studies on the atmosphere effect on adhesion of isocyanate-based primers have not been commonly investigated. Thus, we hope to gain knowledge through research to further understand this phenomenon.

In this study, the atmospheric moisture effect on the surfaces of isocyanate-based primers was probed by SFG, and the molecular behaviors of such surfaces were correlated to macroscopic properties to investigate the relationship. Different conditions in the experiments were set up in a variation of humidity levels and exposure time to understand the influences of their effects on the primer surfaces. In addition to a commercial primer, a model compound containing isocyanate groups was also used to further verify the results. Understanding the atmosphere effect on the surfaces of isocyanate compounds paves the way to exploring optimized conditions for various formulated coatings involving isocyanate primers. The method in this study for detecting the surface changes caused by the environment may also be applied to a variety of coatings or surface layers and used to help guide raw material choices during product development, better define the usage limitations of products and/or satisfy broader requirements.

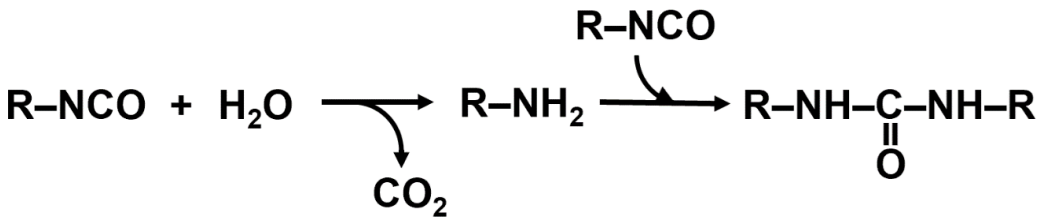


Figure 3.1 Schematic diagram for the reaction of isocyanates with water.

3.2 Materials and Methods

3.2.1 Materials

Right angle calcium fluoride (CaF_2) prisms were ordered from Altos Photonics, Inc. (Bozeman, MT). A two-part primer (PR-420A, PR-420B) was obtained from PPG Industries, Inc. Methyl ethyl ketone (MEK) and polymeric diphenylmethane diisocyanate (PMDI) were purchased from Sigma-Aldrich, Inc (St. Louis, MO).

3.2.2 Sample Preparation

The primer film was prepared using the same method as described in Chapter 2. Briefly, the formulated primer was prepared by mixing the two parts according to manufacturer's instructions and then spin-coated onto a pre-cleaned CaF_2 prism at 4000 rpm for 1 min. The sample to be exposed was placed in a chamber under an environment with a relative humidity of 18% or 50% for a specified timeframe.

3.3 Results and Discussion

3.3.1 180° Peel Strength Test

To determine the level of interfacial adhesion developed by the primer macroscopically, 180° peel strength tests were carried out at PPG between the primer and the potting compound introduced in the previous chapter. The details of the 180° peel strength tests were presented in Chapter 2 above. Before applying the potting compound on top of the primer and the 16-hour curing process, four groups of primer samples were prepared by depositing the primer films on aluminum substrate surfaces. Group 1 primer samples were exposed to nitrogen (with no water

vapor) for 1 hour followed by the potting compound applied on the primer film – This group of the primer sample serves as a control sample group by drying the primer layer in the nitrogen atmosphere without exposing it to humidity. Group 2 and Group 3 primer samples were exposed to an 18% relative humidity RH (low humidity) environment in the air for 4 and 16 hours, respectively, before the application of the potting compound. These two groups of samples were prepared to study the effect of varied exposure times to humidity on interfacial adhesion. The Group 4 primer samples were exposed to 50% RH (high humidity) in the air for 4 hours, aiming to have a comparison to Group 2 to study the effect of the exposed humidity levels on interfacial adhesion.

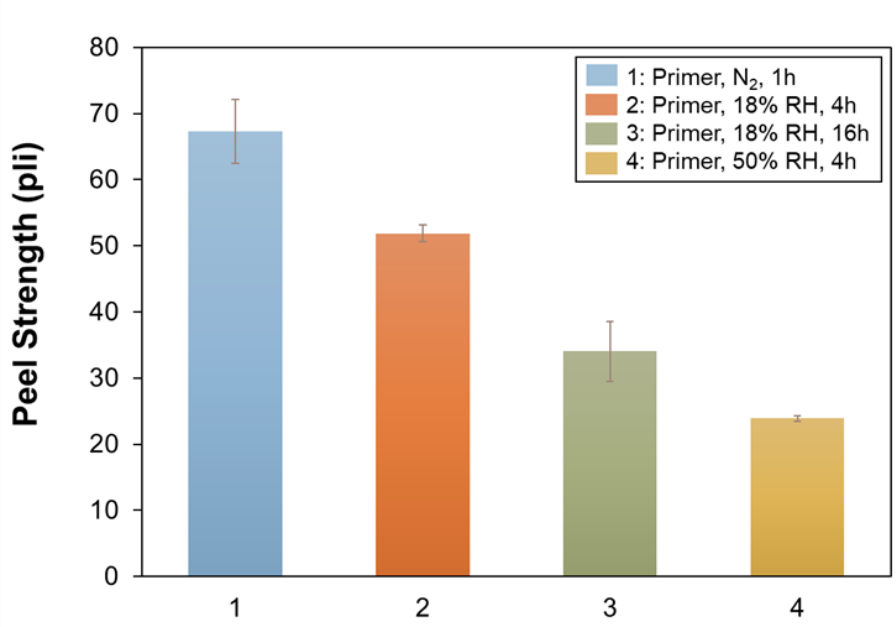


Figure 3.2 Results of 180° peel strength tests. Groups 1-4: the primers used for tests were exposed to nitrogen for 1 h, air with 18% RH for 4 h, air with 18% RH for 16 h, and air with 50% RH for 4 h, respectively.

Figure 3.2 shows the results of the peel strengths at the interfaces between primers and potting compounds when different groups of the primer samples were used. When a primer layer

dried for 1 h under the protection of nitrogen (group 1), very few water molecules were expected to interact with the primer surface in the drying process, and the peel strength was measured to be 67.3 ± 4.8 pli. In contrast, the adhesion strengths measured from the primer/potting compound interfaces for other groups of the primer samples are lower. For the Group 2 primer samples (when the primer layer dried at 18% RH for 4 hours before applying the potting compound), the measured peel strength was reduced to 51.9 ± 1.3 pli, indicating the adhesion strength declined due to the exposure of primer to humid air. A more obvious decrease in adhesion compared to Group 2 can be seen for sample group 3 (34.0 ± 4.5 pli) when the exposure time at 18% RH increased to 16 hours (group 3 samples). The comparison between the Group 2 and Group 3 samples indicates that an increased time of exposure of the primer surface to atmospheric moisture tends to weaken the adhesion performance of the isocyanate-based primer. A longer exposure time increases the chances for water molecules to interact with the primer. The decreasing trend in adhesion was also observed when keeping the exposure time at 4 hours but increasing the relative humidity levels. Group 4 samples with the primer layer dried at 50% RH for 4 hours showed a significant drop in peel strength of the primer/potting compound interface (23.9 ± 0.4 pli), which was much lower than that of the group 2 samples exposure at 18% RH. As a higher relative humidity signifies more water molecules in the same volume, the surface of the primer layer had a greater possibility of being affected by water molecules in a shorter time, which eventually led to a poorer peel strength for the primer/potting compound interface.

It is worth mentioning that both interfacial and bulk properties can affect adhesion. The purpose of this study is to investigate the effects of interfacial interactions on adhesion, therefore we focused on the water effect at the primer surface which induced adhesive failure, and did not study water penetration into the interior of the primer layer which might cause cohesive failure. In

all adhesion measurements above, only adhesive failures were observed, and none of the groups failed cohesively.

3.3.2 SFG Experiments

To explore the mechanisms that led to the differences in peel strengths, SFG was employed to investigate the molecular behavior of the primer surface as a function of the exposure time to humid air. As the chemically active and pivotal part of the primer, isocyanate moieties were monitored as a function of time by SFG at 18% RH. **Figure 3.3** displays the SFG spectra collected from the primer surface in the wavenumber region of 2050-2400 cm^{-1} using the ppp and ssp polarization combinations of the input laser beams and the output signal beam. A distinct peak around 2250 cm^{-1} was observed in each spectrum, which is assigned to the characteristic NCO stretching signal.[24] In **Figures 3.3a** and **3.3b**, a noticeable decrease in terms of the intensity of this peak in both the ssp and ppp spectra was observed from the primer surface with 4 h exposure to the atmosphere compared to that with no atmosphere exposure. This peak intensity further decreased when the primer sample surface was exposed to the 18% RH for a longer period of 16 h. The above results indicate that the longer the primer surface remained exposed to humidity, the greater the reduction in SFG signal intensity of the isocyanate groups.

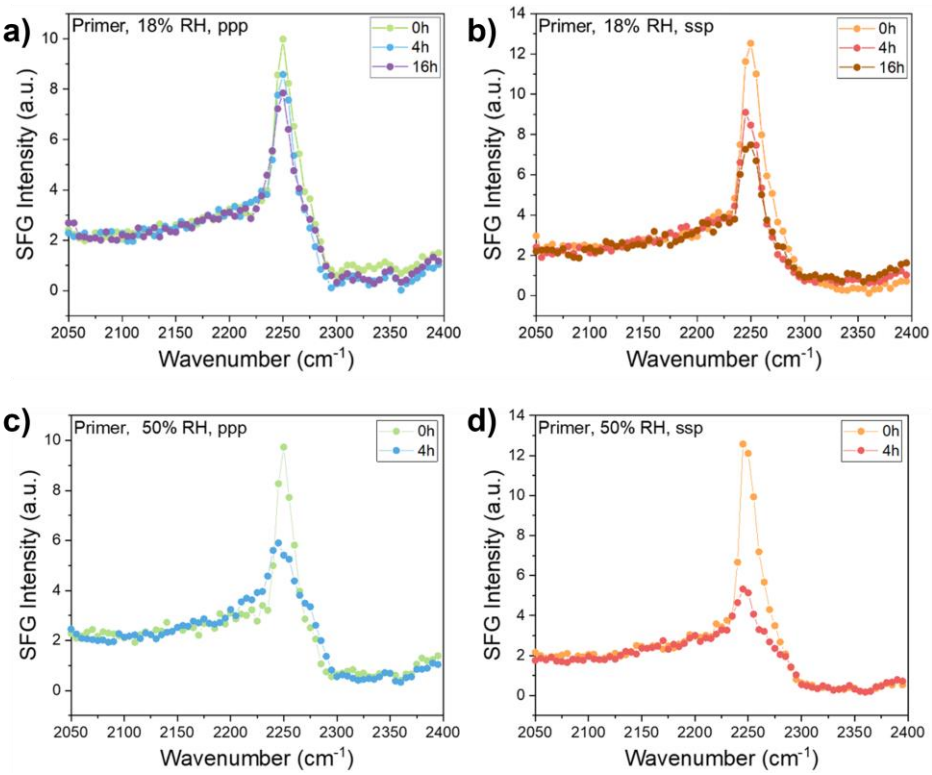


Figure 3.3 (a) SFG ppp and (b) ssp spectra collected from the primer (on CaF_2) at 18% RH at 0-h, 4 h, and 16 h. (c) SFG ppp and (d) ssp spectra collected from the primer (on CaF_2) at 50% RH at 0 h and 4 h. The spectra were collected in the wavenumber range from 2050 to 2400 cm^{-1}.

Figures 3.3c and **3.3d** present the SFG ppp and ssp spectra collected from the primer surface before and after exposure to 50% RH. Both ssp and ppp spectra show that the SFG signal intensity of the isocyanate NCO group substantially decreased after being exposed to the humid air for 4 h, which is more remarkable compared to that occurred at 18% RH. The results indicate that the decrease in SFG intensity after exposure to humid air was attributed to the gradual consumption of the surface NCO groups as a function of time, and the atmospheric moisture likely accounts for the change. The primer surface NCO groups reacted with water molecules in the environment.

It is worth mentioning that **Figure 3.3** also shows that the SFG ssp and ppp signal intensity ratios for NCO groups on surfaces without and with moisture exposure at different humidity levels

and different times are slightly varied. This shows that NCO group orientations could slightly change under different conditions. More details about such orientation changes are under the current investigation.

The above-presented SFG data are well correlated to the measured peel strengths in **Figure 3.2**. The peel strengths indicate that the adhesion between the primer and potting compound decreased after the primer surface was exposed to humid air with a longer time or higher humidity. SFG data in both SFG ssp and ppp spectra indicated that the intensity of the SFG peak contributed by the isocyanate groups on the primer surface decreased after exposure to humid air, indicating the decrease of the isocyanate groups on the primer surface. According to Chapter 2, a key factor for the strong adhesion between the primer and potting compound is the interfacial chemical reaction involving isocyanate groups on the primer surface. The results indicate that the decreased adhesion at the primer/potting compound interface was likely associated with the lower surface coverage of the primer surface isocyanate group.

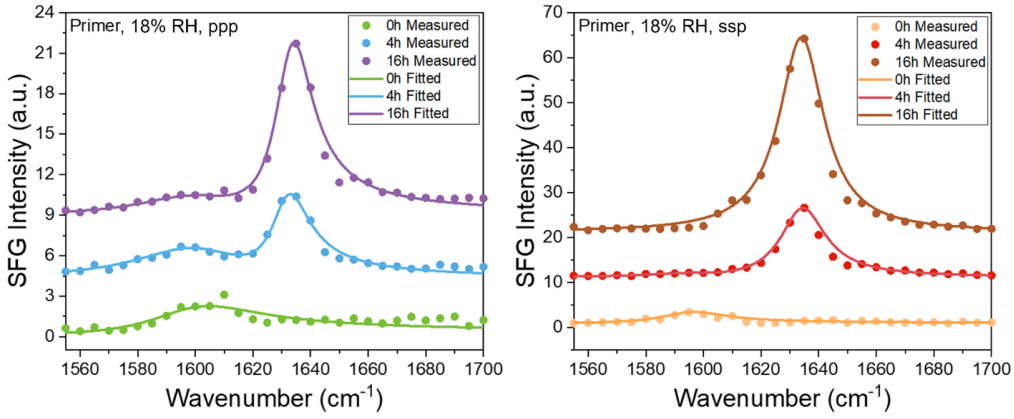


Figure 3.4 SFG ppp (left) and ssp (right) spectra collected from the primer (on CaF_2) at 18% RH at 0 h, 4 h, and 16 h in the wavenumber range from 1555 to 1700 cm^{-1}.

In addition to observing the spectral change in the reactant NCO stretching frequency region, attempts have also been made to study urea linkages, which are the product of the reaction

between isocyanate groups and water in the C=O stretching wavenumber region. Likewise, SFG spectra were obtained from the primer surface at 0 h, 4 h, and 16 h (shown in **Figure 3.4** with data fitted). No obvious SFG signals in the ssp and ppp spectra were detected around 1630 cm^{-1} before the exposure of the primer surface to air (at 0 h), showing that initially urea groups were hardly generated on the primer surface. A noticeable SFG peak showed up at around 1634 cm^{-1} after a 4-hour exposure of the primer surface to the 18% RH. This peak was assigned to the C=O stretching from urea moieties formed as the result of the reaction between isocyanate groups and water moisture.[24] Further growth in intensity of this peak was observed as the primer surface humidity exposure time was extended to 16 h.

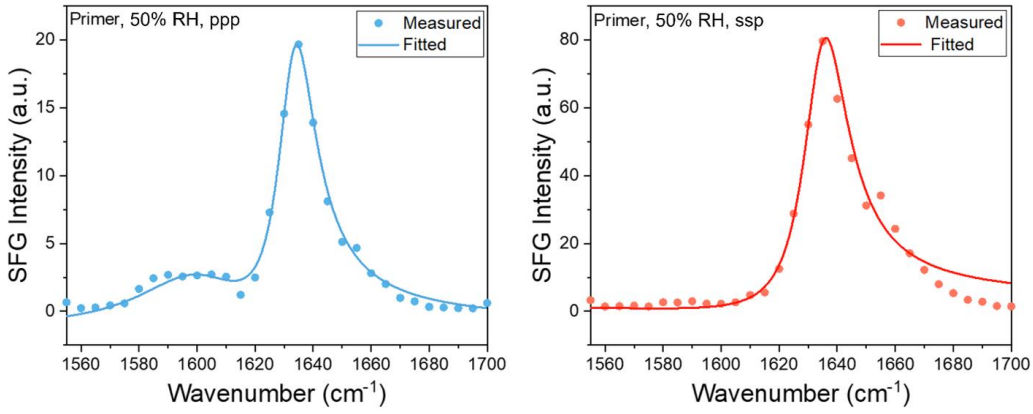


Figure 3.5 SFG ppp (left) and ssp (right) spectra collected from the primer (on CaF_2) at 50% RH at 4 h in the wavenumber range from 1555 to 1700 cm^{-1}.

The product C=O stretching signals were also monitored when the primer was placed in a 50% RH environment for 4 h using SFG. **Figure 3.5** shows that the SFG spectral features collected from the primer surface after exposure to a higher humidity level are similar to those in **Figure 3.4**. Strong SFG C=O peaks representing the formation of urea linkages were detected after 4 h exposure of the primer surface to a higher humidity level, which is correlated well to the decrease in SFG NCO signals shown in **Figure 3.3**.

To verify that the increase in the SFG signal intensity from the primer surface is due to the coverage increase instead of the C=O orientation change, the C=O orientation was determined on the primer surface. SFG orientation analysis was conducted using the methodology reported previously to deduce the tilt angle between the principal axis of a C=O double bond in urea groups and the surface normal.[25] The relation between the measured SFG fitted signal strength χ_{ppp}/χ_{ssp} ratio and a urea group orientation angle θ is shown in **Figure 3.6**.

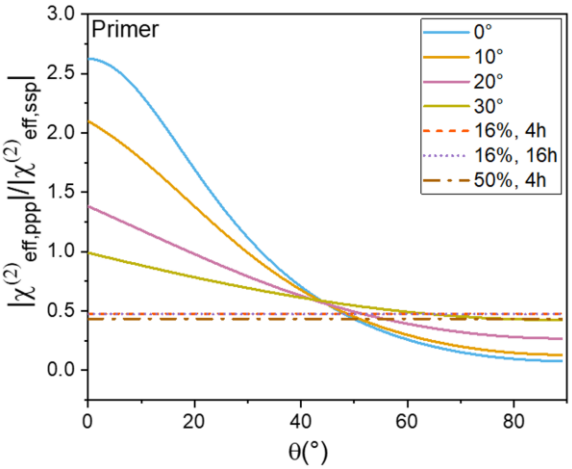


Figure 3.6 The relationship between the SFG susceptibility ($|\chi^{(2)}$eff, ppp$|/|\chi^{(2)}$eff, ssp|) and the tilt angle (θ) of a C=O group vs. the surface normal.

The solid lines in **Figure 3.6** represent the relations when different orientation angle distributions were assumed with Gaussian distributions. The dotted and dashed lines are the measured χ_{ppp}/χ_{ssp} ratios obtained from the fitted SFG spectra (18% RH at 4 h, 16 h and 50% RH at 4 h) shown in **Figure 3.4** and **Figure 3.5**. The intersections of the measured values and the "theoretical solid curves" signify the tilt angles of the C=O groups on the surface. **Figure 3.6** shows that both the tilt angles of the urea C=O structures generated at 18% RH after 4 h and 16 h are around 49°, which indicates that the C=O orientation almost did not change as more urea groups were formed on the surface of the primer through the process. Based on the calculation

results, the differences in SFG C=O spectral intensity for the primer sample surface at 4 h and 16 h humidity exposures shown in **Figure 3.4** are not caused by the C=O orientation difference. The results confirmed that more urea groups were generated along the process as more isocyanate groups reacted with moisture.

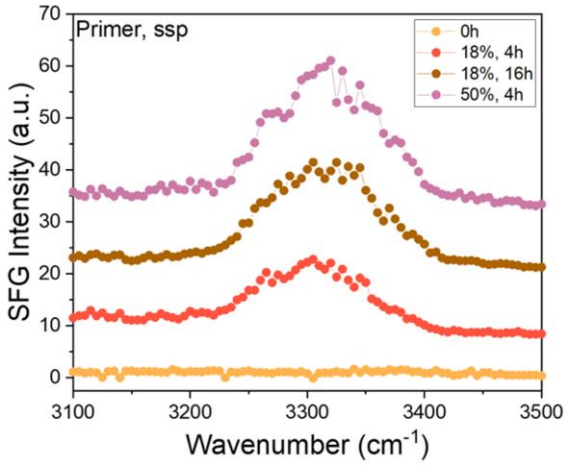


Figure 3.7 SFG ssp spectra collected from the primer (on CaF_2) at 0 h, 18% RH at 4 h, 16 h and 50% RH at 4 h. The spectra were collected in the wavenumber range from 3100 to 3500 cm^{-1}.

In the process of the hydrolysis reaction between isocyanate and water, amine groups and urea groups were generated, both of which contain N-H structures, thus SFG signals were also collected in the wavenumber region between 3100 and 3500 cm^{-1} to further confirm the occurrence of hydrolysis. **Figure 3.7** shows the results of SFG tests on the primer in different conditions in the N-H stretching wavenumber region. The SFG spectrum collected at 0 h before moisture exposure (orange curve) does not show obvious N-H stretching signals, indicating that initially primer did not contain N-H structures, and few products of hydrolysis reaction were generated.

After exposing the primer to humid air, a distinguishable N-H stretching peak was detected by SFG. For the sample exposed to 18% RH for 4 h, the N-H stretching peak from the product urea was detected, indicating the presence of the hydrolysis reaction on the primer surface. The intensity of this peak exhibited an upward trend when the exposure time reached 16 h at the same relative humidity, signifying that more surface isocyanate groups were transformed by the moisture. This trend correlates well with the increase of C=O intensity shown in **Figure 3.4** above, serving as another indication of the surface hydrolysis reaction. On the other hand, the primer exposed to a higher relative humidity of 50% for 4 h showed the most obvious peak among all the sample groups, which suggests a higher extent of transformation of the surface isocyanate groups. The results obtained from SFG studies in the N-H stretching wavenumber region match those obtained in lower frequency regions. The SFG results along with those acquired from the mechanical peel strength tests demonstrate that the higher humidity increased the chances for isocyanate groups to interact with water molecules, leading to more urea linkages produced and a reduced adhesion efficiency.

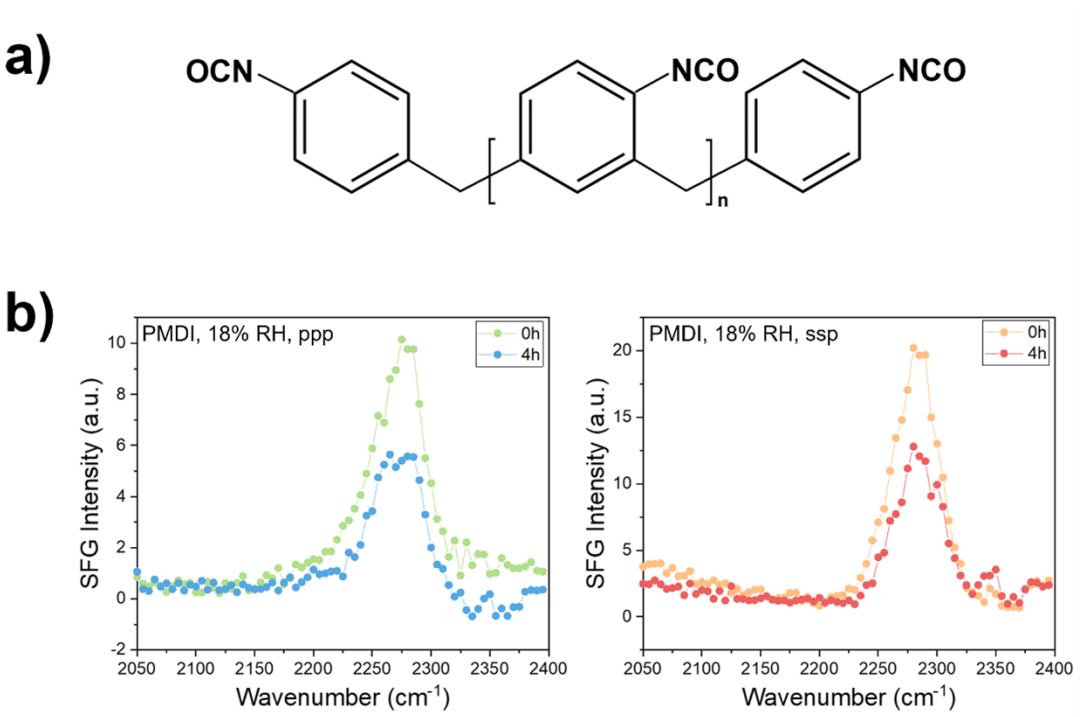


Figure 3.8 a) Chemical structure of PMDI. b) SFG ppp (left) and ssp (right) spectra collected from PMDI (on CaF_2) at 18% RH in the wavenumber range from 2050 to 2400 cm^{-1}.

The isocyanate-based primer used in this study is a commercially formulated product containing a variety of ingredients. To avoid any possible complications, an isocyanate model compound was used to further confirm the chemical reaction between primer surface isocyanate groups and water moisture to generate urea groups. As one of the most commonly used isocyanates, polymeric diphenylmethane diisocyanate (PMDI) demonstrates many distinctive characteristics, like its formaldehyde emission-free feature, small amounts needed for applications, and improved moisture resistance.[20,22] More importantly, it is also a key isocyanate ingredient in the primer tested. Thus, PMDI was considered a suitable candidate for the following SFG study. Its chemical structure is shown in **Figure 3.8a**.

For the control experiments on PMDI, exposure of the polymer model PMDI surface to 18% RH for 4 hours was used for comparison. SFG signals were collected in the same way as

those for previous commercial primer samples. NCO groups were probed by SFG and the related results are illustrated in **Figure 3.8b**. Both SFG ppp and ssp spectra collected from the PMDI surface before and after humidity exposure show characteristic NCO peaks, indicating the surface presence of the NCO groups. The SFG NCO signals became weaker after 4 h humidity exposure compared to those at 0 h, indicating the consumption of isocyanate groups with time on the PMDI surface due to the isocyanate–water reaction, like that observed on the commercial primer surface.

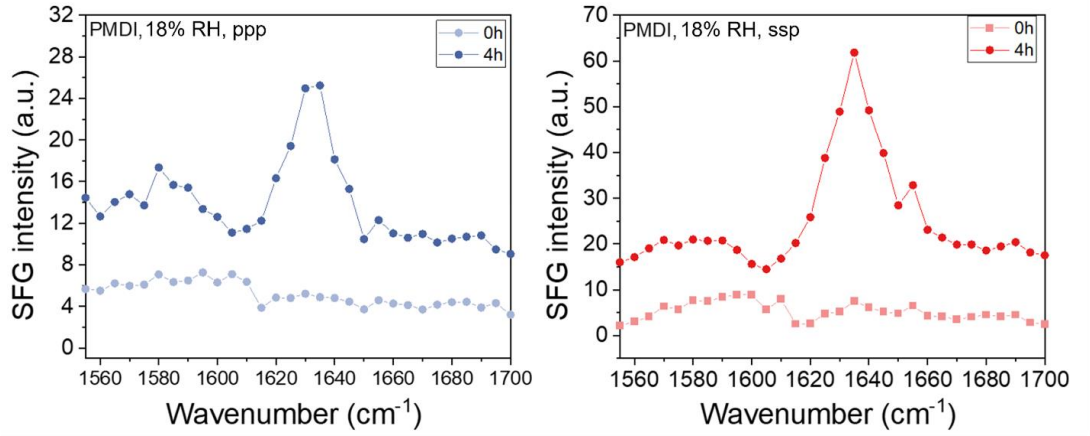


Figure 3.9 SFG ppp (left) and ssp (right) spectra collected from PMDI (on CaF_2) at 18% in the wavenumber range from 1555 to 1700 cm^{-1}.

Figure 3.9 depicts the SFG spectra collected from the primer surface before and after a 4 h exposure to 18% RH in the C=O stretching frequency region. Before exposure, no noticeable SFG signals were detected. In contrast, SFG signals around 1635 cm^{-1} were detected in both ssp and ppp spectra after 4 hours of exposure to the humid air at 18% RH due to the urea linkage formed by the reaction between isocyanate groups and water moisture at the surface. The results presented in **Figures 3.8** and **3.9** are well correlated with each other, showing that water molecules in humid air can react with PMDI surface isocyanate groups to produce urea functionality. The results on PMDI further confirm the conclusion from the study on the commercial primer reported above. This research demonstrates that atmospheric moisture can react with the surface isocyanate

groups to reduce their surface coverage to decrease the primer/potting compound interface adhesion.

3.4 Conclusion

In this study, the atmospheric moisture effect was investigated using SFG to observe the molecular behavior on the surfaces of isocyanate-based primers. It was found that SFG signals of isocyanate groups were gradually decreased as a function of time while the relative humidity was maintained at 18%. A higher relative humidity at 50% led to a further reduction while keeping the exposure time constant. The results indicate an association with the consumption of isocyanate groups at the surface by the reaction with moisture. Further SFG tests were conducted in the C=O and N-H stretching wavenumber regions to verify the reaction. SFG signals in both wavenumber regions were observed to develop throughout the process as isocyanate signals were reduced, which confirms the reaction on the surface. The SFG results are correlated well to the interfacial adhesion strength tested through 180° peel tests, indicating that the surface reaction between the isocyanate group and moisture contributed to the adhesion loss of primer after exposure to the environment. In addition to the commercially used primer, a model compound containing isocyanate groups was also used to further verify the results.

This research is the first time for SFG to be used to probe the isocyanate hydrolysis reaction on the surface and study the atmospheric effect on adhesion strength. SFG can be used to investigate a broad range of surface changes caused by the environment, providing possibilities for establishing structure-function relationships for different types of materials to understand their property changes induced by environmental exposure or environmental changes.

3.5 References

1. Petrie, E. M., *Handbook of adhesives and sealants*. McGraw-Hill Education: 2007.
2. Wypych, G. Handbook of Adhesion Promoters. **2018**,
3. Ebnesajjad, S., *Handbook of adhesives and surface preparation: technology, applications and manufacturing*. William Andrew: 2010.
4. Ebnesajjad, S.; Landrock, A. H., *Adhesives technology handbook*. William Andrew: 2014.
5. Zhou, Y.; Rossi, B.; Zhou, Q.; Hihara, L.; Dhinojwala, A.; Foster, M. D. Thin Plasma-Polymerized Coatings as a Primer with Polyurethane Topcoat for Improved Corrosion Resistance. *Langmuir* **2020,** 36 (4), 837-843.
6. Adams, R. D., *Adhesive bonding: science, technology and applications*. Elsevier: 2005.
7. Wegman, R. F.; Van Twisk, J., *Surface preparation techniques for adhesive bonding*. William Andrew: 2012.
8. Delebecq, E.; Pascault, J. P.; Boutevin, B.; Ganachaud, F. On the versatility of urethane/urea bonds: reversibility, blocked isocyanate, and non-isocyanate polyurethane. *Chem. Rev.* **2013,** 113 (1), 80-118.
9. Heath, R., Isocyanate-Based Polymers. In *Brydson's Plastics Materials*, 2017; pp 799-835.
10. Loureiro, M. V.; Attaei, M.; Rocha, S.; Vale, M.; Bordado, J. C.; Simões, R.; Pinho, I.; Marques, A. C. The role played by different active hydrogen sources in the microencapsulation of a commercial oligomeric diisocyanate. *J. Mater. Sci.* **2019,** 55 (11), 4607-4623.
11. Ma, Y.; Zhang, Y.; Liu, X.; Gu, J. Synthesis of isocyanate microcapsules as functional crosslinking agent for wood adhesive. *J. Adhes.* **2019,** 97 (1), 38-52.
12. Shi, J.; Zheng, T.; Zhang, Y.; Guo, B.; Xu, J. Cross-linked polyurethane with dynamic phenol-carbamate bonds: properties affected by the chemical structure of isocyanate. *Polymer Chemistry* **2021,** 12 (16), 2421-2432.
13. Rashmi, B. J.; Rusu, D.; Prashantha, K.; Lacrampe, M. F.; Krawczak, P. Development of water-blown bio-based thermoplastic polyurethane foams using bio-derived chain extender. *J. Appl. Polym. Sci.* **2013,** 128 (1), 292-303.
14. Santiago-Calvo, M.; Tirado-Mediavilla, J.; Ruiz-Herrero, J. L.; Rodríguez-Pérez, M. Á.; Villafañe, F. The effects of functional nanofillers on the reaction kinetics, microstructure, thermal and mechanical properties of water blown rigid polyurethane foams. *Polymer* **2018,** 150, 138-149.
15. Yi, S.; Cho, Y. J.; Roh, J. S. Improved dimensional stability of water‐blown polyurethane foam with aluminum hydroxide and magnesium hydroxide. *J. Appl. Polym. Sci.* **2020,** 137 (46),
16. Daniel-da-Silva, A. L.; Bordado, J. C. M.; Martín-Martínez, J. M. Moisture curing kinetics of isocyanate ended urethane quasi-prepolymers monitored by IR spectroscopy and DSC. *J. Appl. Polym. Sci.* **2008,** 107 (2), 700-709.
17. Du, W.; Liu, Q.; Lin, R.; Yu, J. Influence of external environment on self-repairing ability of the cement-based materials containing paraffin/toluene-di-isocyanate microcapsules. *Construction and Building Materials* **2021,** 281,
18. Frazier, C., Isocyanate Wood Binders. In *Handbook of Adhesive Technology, Revised and Expanded*, 2003.
19. Gao, Z. H.; Gu, J. Y.; Wang, X. M.; Li, Z. G.; Bai, X. D. FTIR and XPS study of the reaction of phenyl isocyanate and cellulose with different moisture contents. *Pigment & Resin Technology* **2005,** 34 (5), 282-289.
20. He, G.; Yan, N. Effect of moisture content on curing kinetics of pMDI resin and wood mixtures. *Int. J. Adhes. Adhes.* **2005,** 25 (5), 450-455.

21. Martin-Alfonso, M. J.; Navarro, F. J.; García-Morales, M.; Gallegos, C. s. Role of water in the development of new isocyanate-based bituminous products. *Industrial & engineering chemistry research* **2008,** 47 (18), 6933-6940.
22. Wang, X.; Zhao, L.; Deng, Y.; Li, Y.; Wang, S. Effect of the penetration of isocyanates (pMDI) on the nanomechanics of wood cell wall evaluated by AFM-IR and nanoindentation (NI). *Holzforschung* **2018,** 72 (4), 301-309.
23. Wei, Y.; Jiang, X.; Li, S.; Kong, X. Z. Catalysis of isocyanate reaction with water by DMF and its use for fast preparation of uniform polyurea microspheres through precipitation polymerization. *Eur. Polym. J.* **2019,** 115, 384-390.
24. Zhang, S.; Andre, J. S.; Hsu, L.; Toolis, A.; Esarey, S. L.; Li, B.; Chen, Z. Nondestructive In Situ Detection of Chemical Reactions at the Buried Interface between Polyurethane and Isocyanate-Based Primer. *Macromolecules* **2020,** 53 (22), 10189-10197.
25. Li, B.; Andre, J. S.; Chen, X.; Walther, B.; Paradkar, R.; Feng, C.; Tucker, C.; Mohler, C.; Chen, Z. Probing Molecular Behavior of Carbonyl Groups at Buried Nylon/Polyolefin Interfaces in Situ. *Langmuir* **2020,** 36 (38), 11349-11357.

Chapter 4 Probing Saltwater Immersion Effect on Buried Interfacial Structures between Sealant and Adhesion Promoter at the Molecular Level

Adapted from "Zhang, S.; Fu, N.; Cui, W.; Peng, S.; Srivatsan, N.; Chen, Z. Probing Saltwater Immersion Effect on Buried Interfacial Structures between Sealant and Adhesion Promoter at the Molecular Level." *Under review*

S.Z. contributed to investigation, methodology, data analysis and writing. N.F., W.C., and S.P. contributed to methodology and editing. N.S. and Z.C. contributed to conceptualization, methodology, supervision and editing.

4.1 Introduction

Aircraft structures such as fuselages and fuel tanks contain many joints and interfaces that create vulnerabilities to water and contaminant ingress and egress of atmosphere and fuel. Sealants are thus extensively applied on contact points throughout aircraft to serve as protective barriers. For sealants to function effectively, the materials necessarily need to exhibit adhesion to substrates that is robust with respect to the extreme conditions encountered during normal aircraft operation, such as wide temperature swings and contact with various fluids.[1-6] Frequently therefore, for added assurance, sealants are used in conjunction with adhesion promoters that are first separately applied to the substrates. At the present time, new sealants development initiatives to meet the evolving needs of the aerospace industry are quite impeded, in large part due to the difficulty in

engineering robust adhesion. Structural insights into the buried sealant/adhesion promoter interface would hence be invaluable in guiding and expediting the rational design of new higher performing materials. Such interfacial information is difficult to obtain through conventional techniques. Therefore, SFG was applied to investigate interfacial structural information relevant to sealant adhesion.

In this first SFG spectroscopic investigation of an aerospace sealant/adhesion promoter interface, analysis was based on a simplified epoxy-polythioether model sealant system combined with a co-condensation product of hydrolyzed amino and vinyl silanes as adhesion promoter.[7-9] The epoxy-polythioether system is of considerable interest as it lends itself to the development of differentiated high-performance materials such as ultra-light weight 0.75 specific gravity sealants.[10] With respect to the adhesion promoter, the composition was inspired by the work of van Ooij et al. who showed that mixtures of bis[trimethoxysilylpropyl]amine and vinyltriacetoxysilane when cast on metals yield coatings that adhere strongly to the metals, engender excellent paint to metal adhesion, and protect the substrates from corrosion by preventing water ingress.[8] In principle, these characteristics are desirable for aerospace sealant applications where during the normal course of aircraft operation sealants are exposed to various fluids, including jet fuel and water due to condensation in fuel tanks, that can negatively impact adhesion.[2] In practice to ensure robust long-term performance in the field, in-development sealants are subjected to adhesion tests following harsh exposures such as saltwater and hydrocarbon fluid immersions at elevated temperatures.[1] Here as a first step, SFG spectroscopy was employed to study a model sealant-adhesion promoter system following exposure to saltwater at elevated temperatures. Our objective in this preliminary study was to selectively interrogate the

sealant/adhesion promoter interface and attempt to detect structural changes at the interface attributable to the saltwater exposure.

By measuring and comparing spectral features before and after immersion, it was found that the interfacial structure gradually changed during the immersion process, which is likely due to a saltwater-induced change of the adhesion promoter structure. To further investigate which component possibly played a dominant role, model silane compounds that were used as key ingredients of the formulated adhesion promoter were studied separately. The results showed that the amino silane likely dominated the interface that contacted the sealant and contributed more to the adhesion. Based on the intriguing results obtained from the saltwater immersion studies, model fuel immersion experiments will be performed in the future. In addition, functional adhesion tests will be conducted following saltwater and fuel exposures, following which, attempts will be made to connect interfacial structure and structure change to adhesion performance.

4.2 Materials and Methods

4.2.1 Materials

The thiol-epoxy sealant used in this study is a mixture of four parts: Permapol P-3.1e (PPG Inc., CA), THIOCURE TEMPIC (Bruno Bock GmbH, Germany), EPON 828 (Hexion Inc., OH), DABCO 33 LV (Evonik Corporation, VA), which were obtained from PPG Inc. The adhesion promoter 6111 (PPG Inc.) consists of a proprietary combination of amino and vinyl silanes that is partially hydrolyzed. Model silanes including an amino silane ((3-Aminopropyl)triethoxysilane, APTES) and a vinyl silane (Silquest Y-15866 silane, Momentive Performance Materials Inc.) were used to compare with the formulated adhesion promoter. Pre-hydrolyzed silanes were prepared by making a 5% silane solution in isopropanol in the presence of 2 wt% of water followed by a 3-hour treatment at 70°C. The isopropanol used to make model silane solutions and methyl ethyl

ketone used to make thin layer sealant specimens were both purchased from Sigma-Aldrich, Inc. (Burlington, MA). All materials were used as received or as otherwise stated. Calcium fluoride (CaF_2) prisms were obtained from Altos Photonics, Inc. (Bozeman, MT).

4.2.2 Sample Preparation

The mass ratio of components to make the model sealant system and the heating procedure were per the instructions of the manufacturer. Permapol P-3.1e (10 parts), THIOCURE TEMPIC (0.5 parts), EPON 828 (1.7 parts), and DABCO-33 LV (a few drops) were mixed, followed by an elevated temperature heating at 50°C for a few minutes to cure. For SFG experiments, to create buried interfaces between sealant and adhesion promoter, two sample geometries were involved (**Figure 4.1**). A three-layer sandwich sample geometry (which is referred to as three-layer sample or sandwich sample geometry below) was designed and primarily used in the study. Specifically, a thin sealant layer was made on one right-angle side of a pre-cleaned prism through the spin-coating of a 2 wt% diluted sealant solution using MEK. The spin-coating was conducted using a P-6000 spin coater (Speedline Technologies, Franklin, MA) at 2000 rpm for 30 seconds. To prepare the second layer, adhesion promoter 6111 was spin-coated on top using the same spin-coating parameters as mentioned above. Then a thick bulk sealant was cast manually on the dried 6111 layer, so that both sides of adhesion promoter 6111 were in contact with sealant. Therefore, characteristic peaks of 6111 that come from the interface between 6111 and sealant can be measured. MEK is very volatile and does not react with any components in the system. The illustration of the sandwich geometry can be found in **Figure 4.1c**. The other geometry is a two-layer geometry which only contains an adhesion promoter layer spin-coated directly onto a prism, and a bulk sealant on top (**Figure 4.1a**). The preparation procedures and spin-coating parameters are the same as described above. Spin-coated thin adhesion promoter layer samples (as well as

spin-coated sealant layer samples) were also studied as control samples (**Figure 4.1b**). To study the change of interface between adhesion promoter and sealant caused by the immersion process, samples were first tested on SFG to measure the initial spectral features. Subsequently, samples were fully immersed in 3 wt% salt (sodium chloride) water at 60°C. Samples were allowed enough time to dry every time they were taken out of the saltwater before SFG measurements were conducted.

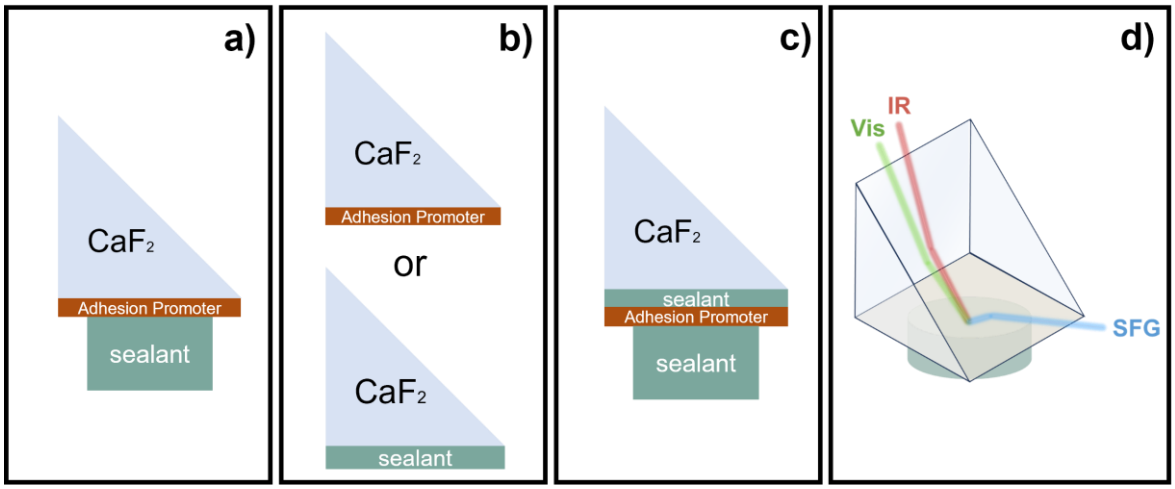


Figure 4.1 Schematic showing the design of three sample geometries used in this study: (a) two-layer sample, (b) spin coated thin layer sample (either adhesion promoter or sealant), and (c) three-layer sandwiched sample. (d) Schematic of sample geometry for collecting SFG spectra.

4.3 Results and Discussion

The primary emphasis of the research was directed towards examining the changes occurring at the sealant/adhesion promoter interfacial region due to immersion, since these could be potentially connected to adhesion performance. In the following, we will present SFG results obtained from three types of samples shown above in **Figure 4.1**: (1) a two-layer sample geometry with a thick sealant layer on an adhesion promoter layer spin-coated on prism substrate, (2) a spin-

coated adhesion promoter on prism substrate, and (3) a three-layer sample geometry with an adhesion promoter sandwiched between sealant layers.

4.3.1 Two-layer Sample Geometry

The two-layer geometry was first examined in the preliminary study – the adhesion promoter 6111 was pre-coated directly onto the prism followed by the application of the sealant (**Figure 4.1a**). SFG spectra in the C-H stretching frequency region were successfully obtained from the cured sample as shown in **Figure 4.2a**. Several peaks were present both in SFG ppp and ssp spectra in the wavenumber region from 2800 to 3100 cm^{-1}. For example, the peak around 2895 cm^{-1} may be attributed to C-H symmetric stretching of methyl groups that are from the adhesion promoter and/or the sealant. The peaks around 2960 and 2980 cm^{-1} may be contributed by the asymmetric C-H stretching of these methyl groups. A peak at around 3050 cm^{-1} was observed in the ppp spectrum, which is likely assigned to C-H stretching mode of vinyl structure from the adhesion promoter and/or aromatic structure of the sealant.

Then the samples were treated at 60°C with or without saltwater for 7 days, and SFG tests were performed to determine whether any molecular changes could be observed. **Figures 4.2b** and **4.2c** show the results of the samples with the two-layer geometry after immersion in 3% saltwater at 60°C for 7 days and after 7 days in air at 60°C absent of saltwater immersion, respectively. Here we compare the spectral features of the SFG results displayed in **Figure 4.2**, not the absolute SFG signal intensities. The changes in SFG signal intensities originated from the fluctuations of laser energy on different days.

Comparing the SFG spectra displayed in **Figures 4.2a** and **4.2b**, it is clear that the sample immersed in saltwater underwent structural changes after 7 days, as demonstrated by the markedly different spectra shown in these two figures. The relative intensity of the peak around 2895 cm^{-1}

versus other signals dropped substantially in both SFG ssp and ppp spectra. Differently, the SFG spectra shown in **Figure 4.2c** are relatively similar to those presented in **Figure 4.2a**. This shows that the sample with only high temperature treatment without saltwater immersion does not exhibit a significant change, though the sample treatment temperature and time lengths were both set to be the same as the immersed one. The results presented in **Figure 4.2** imply that saltwater immersion is likely the main factor that changes the sample over time.

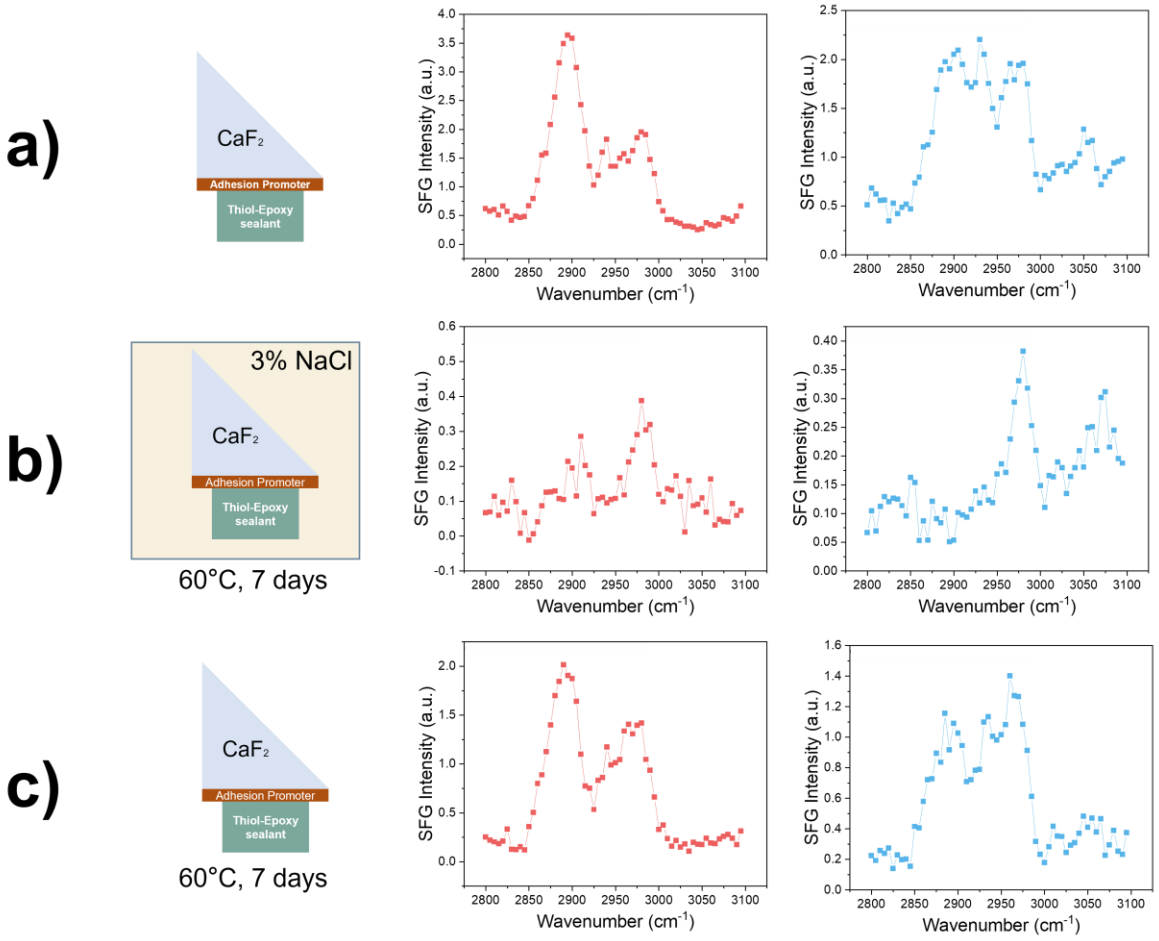


Figure 4.2 a) Schematic showing the two-layer sample geometry before saltwater immersion, ssp (red) and ppp (blue) SFG spectra collected from the sample before immersion. b) Schematic showing the two-layer sample geometry after saltwater immersion at 60°C for 7 days, ssp (red) and ppp (blue) SFG spectra collected from the sample after the 7-day immersion. c) Schematic showing the two-layer sample geometry placed in air at 60°C for 7 days without saltwater immersion, ssp (red) and ppp (blue) SFG spectra collected from the sample after the treatment at 60°C for 7 days.

It is worth mentioning that SFG signals collected from the two-layer samples may originate not only from the sealant/adhesion promoter 6111 interface, but also from the interface between adhesion promoter 6111 and the CaF_2 prism substrate. The above observed spectral changes may be due to the changes at the interface between adhesion promoter 6111 and CaF_2 prism substrate. Thus, further experiments need to be performed to exclude some uncertainties to confirm that the spectral changes observed were indeed caused by the changes at the interface between adhesion promoter and sealant. Such results will be presented below.

4.3.2 Spin-coated Thin Layer Samples on Prism Substrate

In a control experiment, a single adhesion promoter 6111 layer or sealant layer spin-coated on a prism was probed (**Figure 4.3**). The SFG ssp spectrum collected from the adhesion promoter 6111 (**Figure 4.3a**) shows two main peaks centered at 2895 cm^{-1} and 2990 cm^{-1}, likely due to the methyl symmetric and asymmetric stretching modes. These two peaks were also detected from the SFG ppp spectrum from 6111 (**Figure 4.3a**). The ppp spectrum also contains several weaker peaks centered at 2935 and 2965 cm^{-1}, likely due to methyl Fermi resonance and asymmetric stretching. In addition, a peak centered at about 3065 cm^{-1} was detected in the ppp spectrum, due to the vinyl C-H stretching.

Figure 4.3b shows ssp and ppp SFG spectra collected from the sealant thin layer deposited on the prism. In both ssp and ppp spectra, three peaks were detected, centered around 2865 cm^{-1}, 2915 cm^{-1}, and 3050 cm^{-1}. These peaks are likely assigned to the methylene symmetric, asymmetric and aromatic C-H stretching modes, respectively. Interestingly, the peak at 2895 cm^{-1} with the largest change in the immersion process of the two-layer sample geometry presented above was not detected from the sealant, which was detected from the adhesion promoter 6111

(**Figure 4.3a**). This likely indicated that the main change of the two-layer geometry sample observed with saltwater immersion is caused by the change of 6111. This will be tested further below.

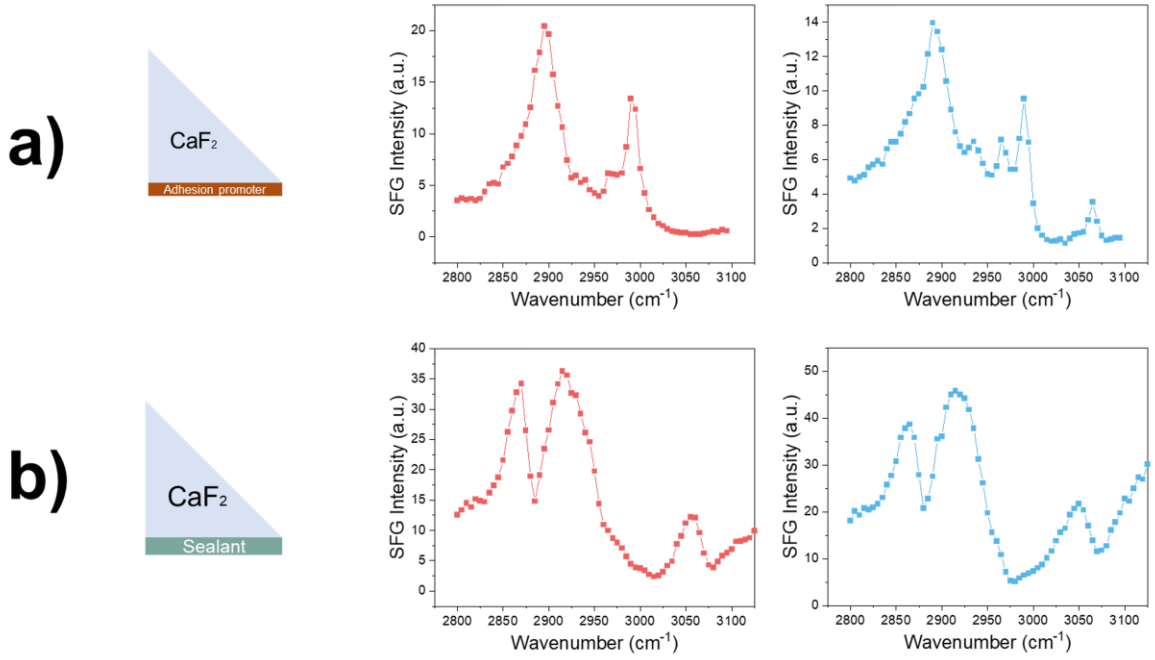


Figure 4.3 a) Schematic showing the adhesion promoter 6111 applied on prism and ssp (red) as well as ppp (blue) SFG spectra collected from the sample. b) Schematic showing the sealant applied on prism and ssp (red) as well as ppp (blue) SFG spectra collected from the sample.

4.3.3 Three-layer Sample Geometry

Another sample geometry was designed to help interpret the process, in which both sides of 6111 were in contact with sealant, as shown in **Figure 4.1c**. In this case, the interface between prism and 6111 in the two-layer geometry was avoided, and distinctive peaks of 6111 (especially the one at ~2895 cm^{-1} which exhibited the largest change in the two-layer sample geometry

presented above) that were absent in sealant would be monitored in order to gain insights into the interfacial behavior of the adhesion promoter during the saltwater immersion process.

Figure 4.4a shows the SFG ssp and ppp spectra of the three-layer sandwich geometry with 6111 before immersion. Both spectra have a distinctive peak at around 2895 cm^{-1} and a weak peak at ~2975 cm^{-1}. As discussed above, the ~2895 cm^{-1} signal was not clearly present in the spectra of the sample containing thiol-epoxy sealant only, which helps to confirm that this signal was contributed by the adhesion promoter 6111 at the sealant/6111 interface. This shows that the target interface between the adhesion promoter and sealant was indeed detected by SFG, and the interface was not disordered (otherwise no SFG signal could be collected). This demonstrates the feasibility of probing molecular structures at the buried adhesion promoter/sealant interfaces in situ using SFG.

Subsequently, the saltwater immersion effect on the 6111/sealant interface with time was studied using the three-layer sample geometry. In **Figure 4.4b**, SFG ssp and ppp spectra collected from the interface of 6111 and sealant after saltwater immersion at 60°C for 1 hour show some difference in the peak relative intensity from the original state, but the peak at 2895 cm^{-1} could still be clearly seen. This indicated that the interfacial structure might be slightly altered by the one-hour water immersion, but such changes were not substantial. SFG ssp and ppp spectra collected from the same interface after immersion in water at 60 °C for 1 day (**Figure 4.4c**) exhibit further changes - the initially detected peak at around 2895 cm^{-1} decreased dramatically, showing that the interface between adhesion promoter and sealant had substantial changes over time that could impact the adhesion. Longer time saltwater immersion to 7 days (**Figure 4.4d**) did not exhibit much further difference in the SFG spectra compared to the 1-day immersed sample, which is likely because the major molecular change at the interface had been completed by one day.

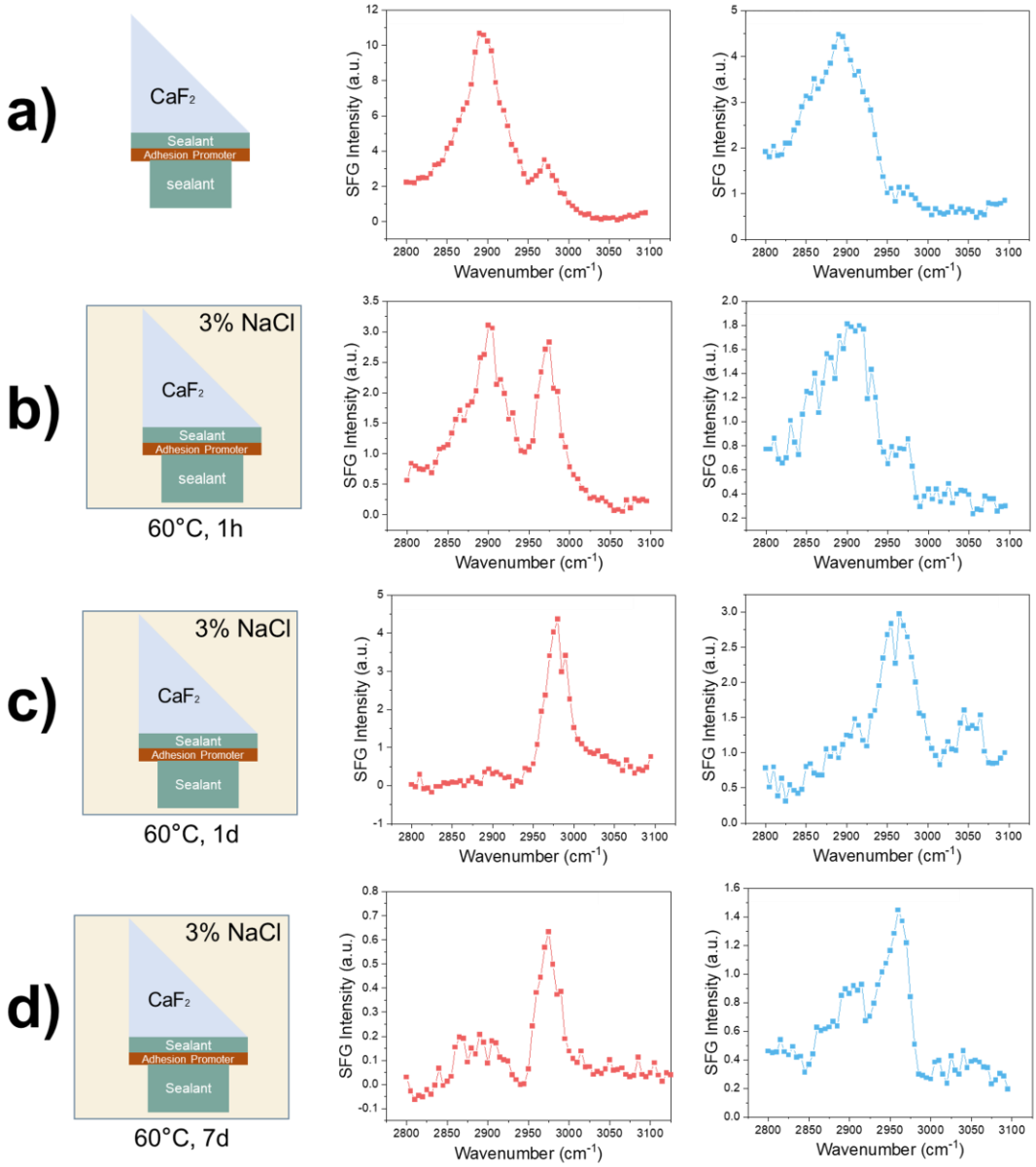


Figure 4.4 Schematic showing the sandwich sample geometry (a, b, c, d) applied on the prism, ssp (red) and ppp (blue) SFG spectra collected from the sample in the condition of: a) before immersion; b) after saltwater immersion at 60°C for 1 hour; c) after saltwater immersion at 60°C for 1 day; d) after saltwater immersion at 60°C for 7 days.

Two control experiments were performed to further compare the immersion conditions and the effect of saltwater. In one control experiment, the three-layer samples were fully immersed in saltwater in the same way for one day, but the temperature was kept at room temperature instead of 60°C during the experiment. In the other experiment, the three-layer samples were placed in the air at 60°C without saltwater immersion. For the samples in saltwater at room temperature for one day, the collected SFG spectra displayed in **Figure 4.5b** show relatively similar results compared to those obtained from the sample treated by the standard immersion setting (at 60 °C, **Figure 4.4c**). This shows that the structural change at the sealant/adhesion promoter interface caused by saltwater immersion does not require a high temperature. It can readily occur at room temperature. The samples treated at 60 °C without saltwater immersion resulted in SFG spectra (**Figure 4.5a**) that do not show much change to their original state (**Figure 4.4a**). This result is similar to those obtained from the two-layer sample presented above and further shows the effect of saltwater on the interface between adhesion promoter and sealant. The intensity decreases or disappearance of the characteristic peak of 6111 at around 2895 cm^{-1} indicates the interfacial changes of 6111 due to the saltwater immersion.

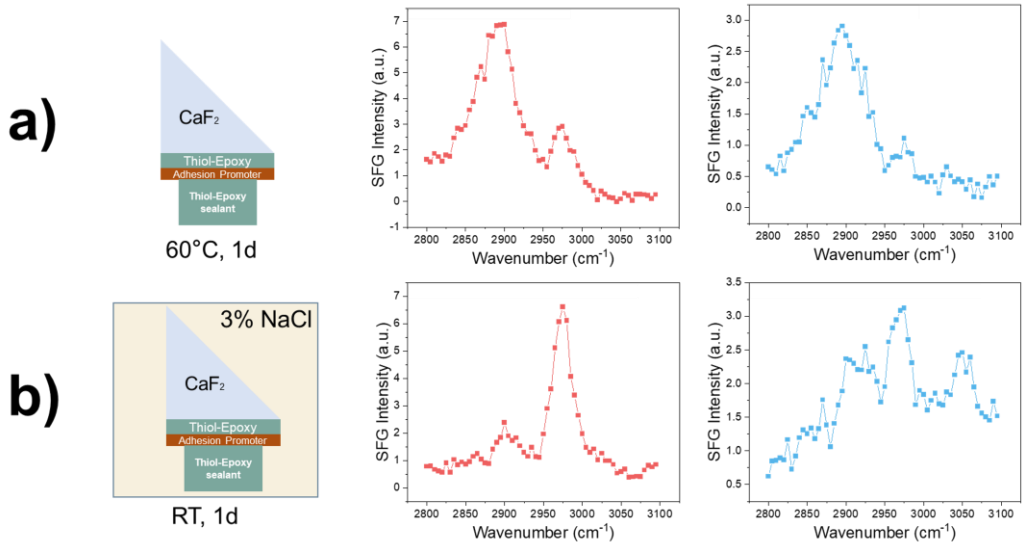


Figure 4.5 a) Schematic showing the sandwich sample geometry placed in the air at 60°C for 1 day, ssp (red) and ppp (blue) SFG spectra collected from the sample after treatment. b) Schematic showing the sandwich sample geometry after salt water immersion at room temperature for 1 day, ssp (red) and ppp (blue) SFG spectra collected from the sample after the 1-day immersion.

The adhesion promoter 6111 is a formulated silane-based product with various types of silanes mixed together. Even though several silanes are involved, they may not all segregate at the sealant/6111 interface and interact with the sealant layer. It is possible that certain types of silane may remain in the bulk structure and do not contribute much to the adhesion, while other types of silanes are dominantly present at the interface and play significant roles in adhesion. Therefore, it is of interest to investigate the interfacial behaviors of different silanes at the sealant/adhesion promoter interfaces. Such knowledge will provide helpful information for future adjustments on adhesion promoter formulations.

Since the major silane compositions in 6111 are amino silanes and vinyl silanes, in this study, two model silanes, an amino silane APTES and a vinyl silane Y-15866, were used to replace the 6111 in the sandwich geometry shown in **Figure 4.1c** for SFG tests. Therefore, the interface against the sealant would be either the amino silane or the vinyl silane. If the results obtained from a model silane three-layer sample are similar to those from the 6111 sandwich geometry, then the silane likely dominates the sealant/6111 interface and plays an important role in adhesion. **Figures 4.6a and 4.6d** show SFG ssp and ppp spectra collected from the sandwich-geometry samples involving model silanes before immersion. Compared to the SFG spectra from the sandwich geometry with 6111 (**Figure 4.4a**), the spectra collected from the vinyl silane Y-15866 three-layer sample (**Figure 4.6a**) do not show much similarity, which likely indicates that a great amount of vinyl silane molecules tends to stay in the bulk of the 6111 layer after the application rather than the interface with sealant, or the portion of the vinyl silane in the formulated 6111 at the

sealant/6111 interface is small that it does not contribute much to the overall adhesion. On the other hand, the SFG spectra collected from the amino silane APTES three-layer sample are more similar to those from the sandwich sample with 6111, meaning plenty of amino silane molecules are likely present at the interface and contribute to the adhesion with sealant.

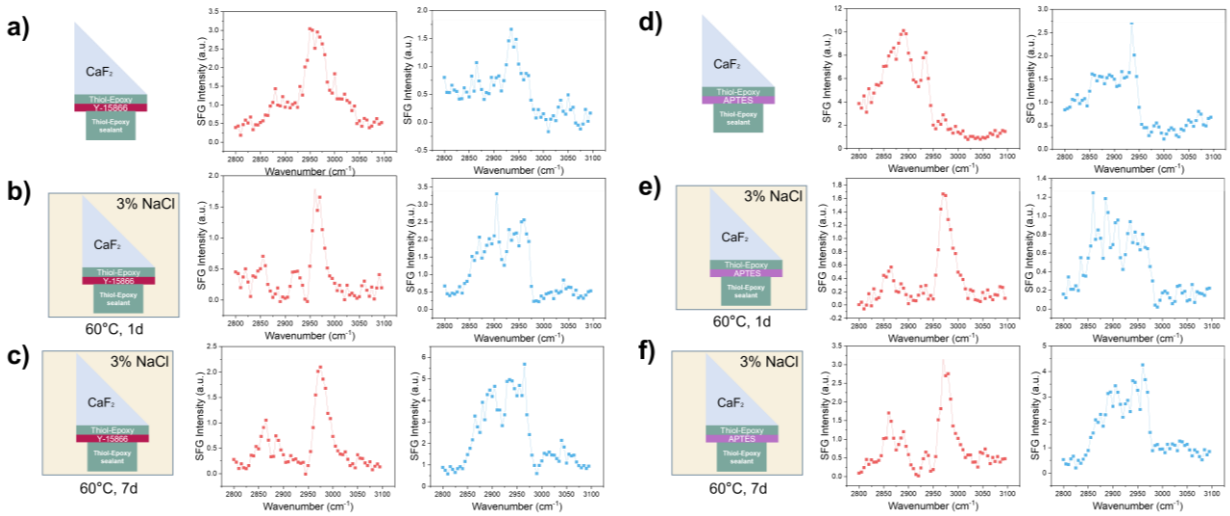


Figure 4.6 Schematic showing the sandwich sample geometry made with the vinyl silane Y-15866, ssp (red) and ppp (blue) SFG spectra collected from the sample in the conditions of: a) before immersion; b) after saltwater immersion at 60°C for 1 day; c) after saltwater immersion at 60°C for 7 days. Schematic showing the sandwich sample geometry made with the amino silane APTES, ssp (red) and ppp (blue) SFG spectra collected from the sample in the conditions of: d) before immersion; e) after saltwater immersion at 60°C for 1 day; f) after saltwater immersion at 60°C for 7 days.

Interestingly, different from the results obtained from the model silane three-layer samples where different silanes led to varied interfacial structures between silanes and sealant, SFG spectra collected from both model silane sandwich samples after the saltwater immersion displayed in **Figures 4.6b, 4.6c, 4.6e,** and **4.6f** show relatively similar results. This is probably because either different types of silane molecules interacted with the sealant in the same way during the immersion process (which was less likely), or the silane molecules were randomly distributed at the interface or left the interface and completely diffused into the sealant.

While silane coupling agents can directly react with certain substrates without the need for prehydrolysis, anchoring silane molecules to surfaces becomes challenging for substrates with low accessibility.[11] Therefore, it is a common practice in the industry to conduct pre-hydrolysis to generate more reactive silanol groups. This hydrolysis step will influence the silane adhesion to the surface.[12,13] As silanes used in the recipe of 6111 are partially hydrolyzed, to better mimic the real situation, in this study, we also carried out SFG experiments on model silane three-layer samples after silane pre-hydrolysis. **Figure 4.7** shows SFG spectra collected from model silane three-layer samples after silane pre-hydrolysis before and after saltwater immersion. Before immersion, the SFG spectra from the amino silane sandwich geometry are similar to those from the 6111 three-layer sample. However, after immersion, all the SFG spectra appear similar, regardless of the model silanes used in the three-layer sample. The results are also similar to those presented above acquired from the samples without pre-hydrolysis.

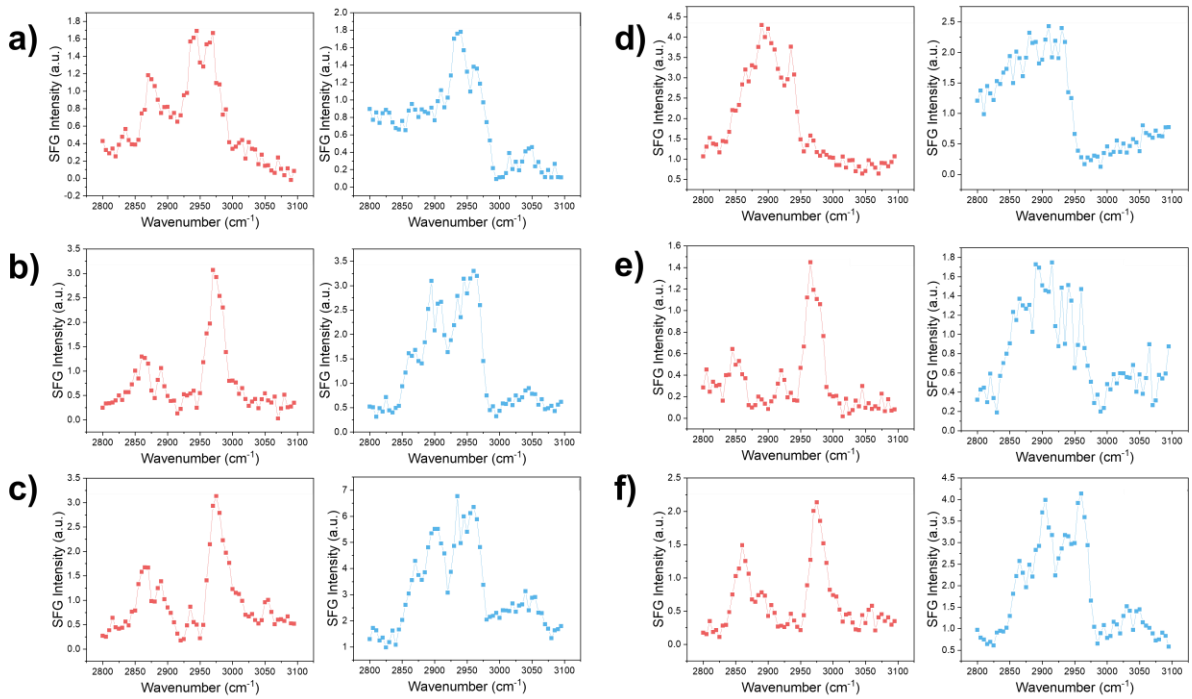


Figure 4.7 Schematic showing the sandwich sample geometry made with the pre-hydrolyzed vinyl silane Y-15866, ssp (red) and ppp (blue) SFG spectra collected from the sample in the conditions of: a) before immersion; b) after saltwater immersion at 60°C for 1 day; c) after saltwater immersion at 60°C for 7 days. Schematic showing the sandwich sample geometry made with the pre-hydrolyzed amino silane APTES, ssp (red) and ppp (blue) SFG spectra collected from the sample in the conditions of: d) before immersion; e) after saltwater immersion at 60°C for 1 day; f) after saltwater immersion at 60°C for 7 days.

To help further elucidate the above observations, a sample prepared using thiol-epoxy sealant only was immersed in the saltwater at 60°C for 1 day. This sample only contains the CaF_2 substrate/sealant interface which can generate SFG signal. The SFG spectra (**Figure 4.8a**) of the original sample before immersion are different from the SFG spectra collected from previous three-layer samples (**Figure 4.4a**). For example, the 2895 cm^{-1} peak was not detected, further confirming the assignment of this peak to 6111. After immersion, SFG spectra collected from the sealant sample (**Figure 4.8b**) showed similarities to those collected from three-layer samples (with 6111 or model silanes) immersed in the same condition. Thus, the above SFG signals collected after the immersion were more likely mainly contributed by the interface between prism and sealant, which indicates the sealant/adhesion promoter interface was disordered. SFG spectra were also collected in lower frequency regions (1500 – 1900 cm^{-1}) where no signal was detected.

With respect to adhesion, an epoxy cure sealant is expected to covalently anchor to adhesion promoter containing aminosilanes via amine-epoxy coupling reactions. The facile nature of the order to disorder transition upon saltwater immersion however suggests that the interactions between the adhesion promoter and sealant are non-covalent in nature. The initial ordered 6111 at the interface (evidenced by the strong 2895 cm^{-1} peak) might lead to stronger interfacial interaction. After the saltwater immersion, the disordered interface could have less hydrogen bonds between sealant and 6111, and reduced the Van der Waals interaction at the interface as well, with potential implications for adhesion.

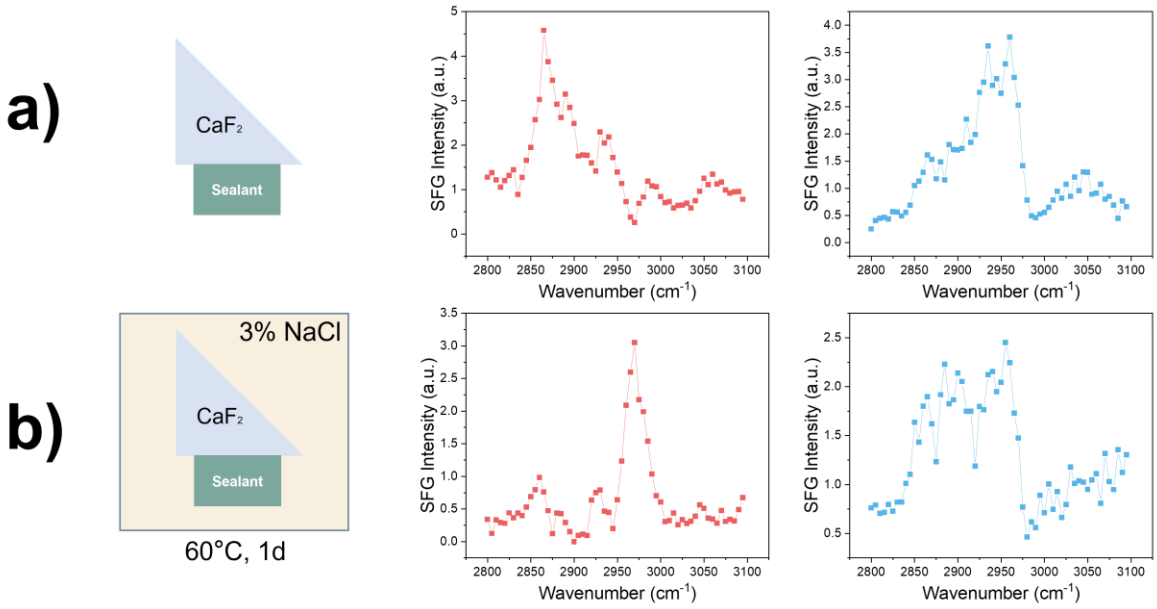


Figure 4.8 Schematic of SFG sample geometry and SFG ssp (red) and ppp (blue) spectra collected from a sample with thiol-epoxy sealant alone before (a) and after (b) the 3% saltwater immersion at 60°C for 1 day.

4.4 Conclusion

This research demonstrated the feasibility of applying SFG to examine molecular changes at the buried interface between an adhesion promoter 6111 and a model thiol-epoxy sealant after saltwater immersion. SFG spectra were successfully collected by creating the interfaces of adhesion promoter and sealant using two sample geometries. The two-layer geometry indicates that the saltwater immersion is likely the main factor that changes the sample over time, whereas elevated temperature does not play a significant role that affects the interfacial molecular structures. Then a characteristic peak from the adhesion promoter was used as a benchmark to confirm the detection of the sealant/6111 adhesion promoter interface by SFG using the three-layer sandwich geometry. The interface experienced structural change during the first day of immersion, with the decrease in the peak around 2895 cm^{-1} clearly observed. The structural change does not seem to

continue obviously after the first day, as the results of a 7-day immersion are similar to the 1-day immersed ones.

In this study, model silanes were employed to investigate whether any specific silanes in 6111 exert a predominant influence at the interface with sealant, and it was found that the amino silane APTES likely aggregates more at the interface and interacts with sealant compared to the vinyl silane Y-15866. The results after the saltwater immersion are generally similar to those obtained from the sample with sealant directly in contact with the prism, which suggests that the interface of the adhesion promoter likely became disordered, which could lead to weaker interfacial interactions with sealant. Such changes have potential implications for adhesion.

The interfacial selectivity and sensitivity that SFG possesses make it feasible to detect potential structural changes at buried interfaces in situ without destruction throughout a sample treatment process. This study introduces an examination method designed to offer insights for the industry, aiding in the interpretation of the mechanism behind performance and contributing to addressing emerging challenges for materials.

4.5 References

1. SAE International; AMS 3277TM Rev. K; Sealing Compound, Polythioether Rubber Fast Curing for Integral Fuel Tanks and General Purpose, Intermittent Use to 360 °F (182 °C). 2019.
2. Giannis, S.; Adams, R.; Clark, L.; Taylor, M. Investigation of the water and fuel exposure characteristics of aircraft fuel tank sealants and the effect on their glass transition temperature. *J. Appl. Polym. Sci.* **2008,** 108 (5), 3073-3091.
3. Giannis, S.; Adams, R.; Clark, L.; Taylor, M. Peel behaviour of aircraft fuel tank sealants: the effect of peel angle, sealant layer thickness and peel rate. *J. Adhes. Sci. Technol.* **2008,** 22 (13), 1495-1522.
4. Giannis, S.; Adams, R.; Clark, L.; Taylor, M. The use of a modified peel specimen to assess the peel resistance of aircraft fuel tank sealants. *Int. J. Adhes. Adhes.* **2008,** 28 (4-5), 158-175.
5. Giannis, S.; Adams, R. D. Failure of elastomeric sealants under tension and shear: Experiments and analysis. *Int. J. Adhes. Adhes.* **2019,** 91, 77-91.

6. Ruiz-Yi, B.; Oswald, C.; Frankovich, L.; Fersner, A.; Kandapallil, B.; Lauterbach, J. Response surface design of a thiol-ene polymer sealant to model adhesive strength. *J. Adhes. Sci. Technol.* **2021,** 35 (23), 2710-2720.
7. Clark, L. J.; Cosman, M. A. Use of Permapol® P3. 1 polymers and epoxy resins in the formulation of aerospace sealants. *Int. J. Adhes. Adhes.* **2003,** 23 (5), 343-348.
8. Zhu, D.; Van Ooij, W. J. Corrosion protection of metals by water-based silane mixtures of bis-[trimethoxysilylpropyl] amine and vinyltriacetoxysilane. *Prog. Org. Coat.* **2004,** 49 (1), 42-53.
9. Zook, J. D.; DeMoss, S.; Jordan, D. W.; Rao, C. B., Composition and method for producing fuel resistant liquid polythioether polymers with good low temperature flexibility. US 6172179 B1, 2001.
10. Virnelson, B., Low density aerospace compositions and sealants. US 11760909 B2, 2023.
11. Xie, Y.; Hill, C. A.; Xiao, Z.; Militz, H.; Mai, C. Silane coupling agents used for natural fiber/polymer composites: A review. *Composites Part A: Applied Science and Manufacturing* **2010,** 41 (7), 806-819.
12. Blum, F. D.; Meesiri, W.; Kang, H.-J.; Gambogi, J. E. Hydrolysis, adsorption, and dynamics of silane coupling agents on silica surfaces. *J. Adhes. Sci. Technol.* **1991,** 5 (6), 479-496.
13. Sypabekova, M.; Hagemann, A.; Rho, D.; Kim, S. 3-Aminopropyltriethoxysilane (APTES) Deposition Methods on Oxide Surfaces in Solution and Vapor Phases for Biosensing Applications. *Biosensors* **2022,** 13 (1), 36.

Chapter 5 Evaluating Polyethylene Weathering Processes after Simulated Solar Exposure and in Situ Lake Deployment

Adapted from a submitted manuscript "Zhang, S.; Lin, T.; Zhang, C.; Cable, R.; Choi, J.; Thakre P.; Serrat, C.; Tan, Y.; Hu J.; Meunier, D.M.; Lai, Y.; Duhaime, M.; Chen, Z. Analysis of Accelerated Weathering Effect on Polyethylene with Varied Parameters Using a Combination of Analytical Techniques. " *Under Review*

S.Z., T.L., and C.Z. contributed to investigation, methodology, data analysis and writing. R.C., J.C., contributed to investigation and editing. P.T., C.S., Y.T., and J.H. contributed to methodology and editing. D.M.M. contributed to conceptualization, methodology and editing. Y.L. contributed to conceptualization, methodology, editing, and supervision. M.D. and Z.C. contributed to conceptualization, methodology, supervision, supervision and editing.

5.1 Introduction

Polyethylene (PE) is a ubiquitous and versatile plastic that finds widespread use in various applications due to its unique properties. The key advantages such as durability, lightweight nature, and chemical inertness make it excel in packaging that preserves a wide array of products.[1,2]

Despite the recognition of polyethylene's positive contributions to our quality of life, the persistent accumulation of used polyethylene materials in the environment poses significant

questions about their long-term ecological implications, notably the rising presence of plastic debris in nature.[3,4] As such, understanding the environmental fate of polyethylene becomes imperative in guiding the development of sustainable and responsible solutions to address the challenges associated with plastic waste.

Numerous studies have explored the degradation of polyethylene through various treatments. Among these, photooxidation has been extensively investigated as a means to accelerate polyethylene degradation over the past several decades.[5-12] In theory, pure polyethylene is resistant to photooxidative degradation due to its hydrocarbon structure, which is not easily susceptible to sunlight reaching the earth's surface (with a cutoff wavelength of 295 nm). Nonetheless, degradation may occur due to structural defects and impurities introduced during manufacturing. These defects are more susceptible to photooxidation, while impurities act as chromophores, absorbing UV light and undergoing photooxidation, thereby contributing to the degradation of polyethylene materials.

Despite significant research on photooxidation, a great portion of it has focused on specific polyethylene models or commercial products with limited characterization techniques, necessitating further investigation to establish a direct correlation between polyethylene manufacturing parameters and degradation behaviors through a more comprehensive approach. This knowledge is critical for evaluating the environmental consequences of degraded materials and for enabling plastic producers to identify variations in molecular architecture changes. These changes may impede materials from undergoing numerous cycles of mechanical recycling without encountering a notable decline in performance in the future. For phase 1, this research stands out for its focus on a diverse range of polyethylene materials, including high-density polyethylene (HDPE) and linear low-density polyethylene (LLDPE) products, which enables a more

comprehensive comparison of their responses to weather exposure. These materials are commonly employed in packaging applications and this research is in collaboration with a main plastic manufacturer Dow Chemical Company. Here plaques and films made from these materials were subjected to simulated solar radiation to assess the UV irradiation effect on polyethylene degradation and to comprehend the weathering process. Additionally, the research is notable for its utilization of various analytical techniques, such as attenuated total reflection - Fourier transform infrared spectroscopy (ATR-FTIR), water contact angle measurement, Raman microscopy, grazing incidence X-ray Diffraction (GIXRD), and nano-indentation tests, to evaluate and correlate the physical and chemical properties of polyethylene materials at different exposure levels. ATR-FTIR analysis has been employed to track changes in the number of carbonyl, hydroxyl, and vinyl groups, commonly observed degradation products, within the wavenumber range of 4000 to 600 cm^{-1}. ATR-FTIR allows for the examination of changes in the surface regions of polyethylene specifically, as the infrared beam only penetrates the surface rather than traversing the entire sample. Water contact angles serve to assess the hydrophilicity of polyethylene surfaces, indicating the presence of polar functional groups generated during degradation. Raman spectroscopy provides microscopic structural insights into crystallinity changes induced by photooxidation. Additionally, GIXRD serves as a surface-sensitive diffraction technique to confirm differences in polyethylene crystallinity. Furthermore, nanoindentation tests reveal macroscopic differences in mechanical properties resulting from molecular changes. The findings demonstrate that increased polar groups, hydrophilicity, crystallinity, and higher elastic modulus are contingent on dynamic structural changes of various polyethylene samples under UV irradiation over time. The combined application of these techniques allows for a comprehensive comparison of the chemical and physical properties of different polyethylene materials induced by

solar exposure. By correlating polyethylene material parameters with their photooxidative behaviors, this study aims to elucidate polyethylene degradation, fostering a deeper understanding of the environmental impact of degraded materials and assisting industries in developing and modifying plastics that are less detrimental to the environment.

When polyethylene is exposed to the environment, degradation is influenced by a combination of factors such as sunlight exposure,[9,13-19] microbial activity,[2,20-31] heat,[32-38] and environmental elements.[39] Therefore, investigating polyethylene behavior in real-world environments is crucial for gaining a comprehensive understanding of its environmental impact. This holistic approach is essential for thoroughly assessing the environmental consequences of degraded materials and assisting plastic producers in devising effective solutions.

Many research efforts have been made to study polyethylene degradation in lab settings and real environments. Biber et al. investigated several types of plastics including polyethylene deployed in both air and sea water and measured the change in the range of 7 and 600 days.[40] Elkori et al. studied the degradation of HDPE bottles through accelerated artificial weathering in seawater with different aging times and temperatures.[41] Ma et al. used freshwater lake sediments as microorganism sources and studied the biodegradation of polyethylene in aerobic and anaerobic microculture environments.[42] Sudhakar et al. immersed HDPE, LDPE and PP coupons in the Bay of Bengal near Chennai Port in Asia for a period of 6 months to observe their degradation in tropical sea water.[43] Previous studies of the environmental degradation of polyethylene provide a variety of approaches that are meaningful to measure the changes and the effect of variables, offering profound insights into the long-term consequences of polyethylene presence in the environment.

In phase 2, our research reported here combined laboratory exposure using a UV accelerated weathering test chamber and in situ exposure by lake deployment to study weathering effects on polyethylene, which enabled an investigation of the individual and combined role of solar radiation and biofilm deposition in the polymer degradation processes. The combination of in situ exposure by lake deployment of the samples pre-treated using an accelerated weathering chamber in the lab aimed to monitor the effect of pre-UV treatment on the subsequent degradation in the real environment. Different from many existing works, the highlight of this phase is the multiple variables set up in hopes of a comprehensive assessment of their effects on polyethylene structural changes. For treatments, various simulated solar exposure (or UV aging) times and *in situ* lake exposure times were applied to observe the degradation trends. In addition, to study whether different lake environments (differences in microbe community composition, sunlight penetration, etc.) would result in various degradation outcomes, *in situ* exposed samples were deployed at different water columns (or depths from the water surface). The large data sets generated based on the multiple variables were studied using statistical analysis for a systematic evaluation of various experimental and sample factors and their correlations.

5.2 Materials and Methods

5.2.1 Materials

HDPE and LLDPE samples used in this study were provided by The Dow Chemical Company. Detailed parameters of materials are shown in **Table 5.1**. The samples contain five polyethylene plaques and two polyethylene films.

Generic Label	Architecture	Generic description	Density (g/cm^3)	Melt Index (g/10 min at 190 °C)	Thickness (mm)
G	Plaque	HDPE	0.9573	1.4	~3
H	Plaque	HDPE	0.9555	1.5	~3
J	Plaque	LLDPE	0.9159	0.94	~3
K	Plaque	LLDPE	0.9145	0.98	~3
L	Plaque	LLDPE	0.9214	0.95	~3

Generic Label	Architecture	Generic description	Density (g/cm^3)	Melt Index (g/10 min at 190 °C)	Thickness (mil/μm)
#5	Film	LLDPE	0.923	1	3/75
#6	Film	HDPE	0.9646	0.91	3/75

Table 5.1 Material parameters of polyethylene investigated in this research

UV pre-aging (wks)	Deployment (Month)	Depth (m)
0, 2, 4	2,14	1.5, 15, 30

Table 5.2 Treatment conditions on samples

5.2.2 Weathering Conditions

Table 5.2 shows the conditions of the simulated solar exposure in the UV accelerated weathering test chamber (also referred to as "UV aging" below) and in situ exposure (freshwater lake deployment) applied for individual and combined treatments to evaluate their effects on polyethylene samples. Samples were treated using varied lab UV aging duration, lake deployed

time, and deployed depths in order to comprehensively investigate the individual and synergistic effects of various experimental factors on the changes of these samples.

Simulated Solar Exposure: UV pre-aged samples were prepared based on ISO 4892 cycle 4 (SUNTEST XXL chamber, ATLAS MTS LLC) with UV, heat, and moisture stressors involved to mimic the outdoor environment. The acceleration factor is four to five times compared to the outdoor aging in southern Florida using equivalent UV dosage calculation. The length of time for UV pre-aging ranges from 0, 2 to 4 weeks in the chamber and that translates to 0, 2 and 4 months of outdoor UV aging respectively.

In situ Exposure: Polyethylene samples were fixed on a series of frames that were deployed in Lake 239 at the IISD Experimental Lakes Area (ELA; Ontario, Canada) at 1.5 m (photic), 15 m, and 30 m (benthos) for 2 and 14 months to investigate the lake effect on the degradation of polyethylene materials. The 14-month retrieval time allows samples to experience at least one cycle of all four seasons.

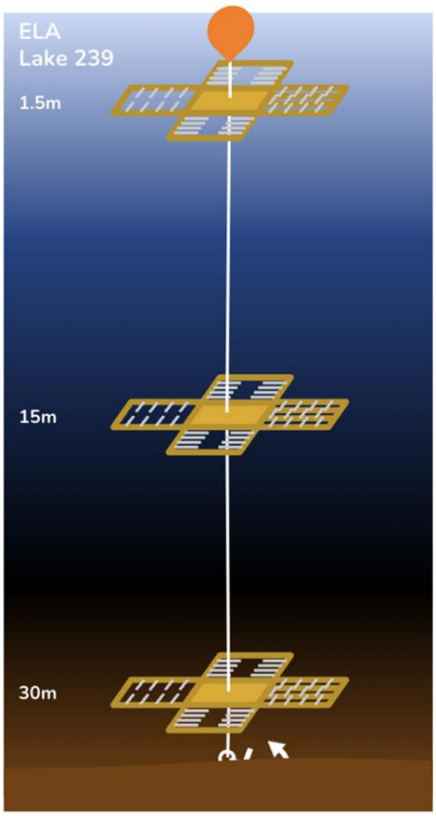


Figure 5.1 Schematic of plastic samples deployed in the lake for in situ exposure.

Post-lake deployed samples are often covered with biofilms and that prevents the characterization at polyethylene surface of interest. To effectively remove biofilms while preserving the changes at polyethylene surface, samples are rinsed with ethanol, sodium dodecyl sulfate (SDS) water solution, and deionized water to remove the attached biofilms, algae, and/or sediments on the surface, followed by air drying before characterization.

5.2.3 ATR-FTIR Experiments

Attenuated total reflectance Fourier transform infrared spectroscopy (ATR-FTIR) has been commonly used to observe the chemical changes in plastic samples. In this study, ATR-FTIR spectra with a wavenumber range of 4000 to 600 cm^{-1} and a resolution of 4 cm^{-1} were obtained by using a spectrometer (Nicolet iS50, Thermo Scientific) controlled by OMNIC software. The

functional group changes could be monitored by ATR-FTIR signals to describe the degradation process of polyethylene. To quantitively compare the polyethylene structural change, particular attention was paid to carbonyl groups, and the carbonyl index could be deduced based on a ratio of a carbonyl peak to a reference peak. For phase 1, the carbonyl index was determined by assessing the maximum absorption in the carbonyl range (approximately 1714 cm^{-1}) relative to the reference methylene absorbance at around 730 cm^{-1}, following the methodology described in the existing literature. This calculation relied on averaging values obtained from repeated tests conducted on each sample. Similarly, the vinyl index was established by comparing the absorbance around 909 cm^{-1} to the reference methylene absorbance. In phase 2, the carbonyl index was calculated using the maximum intensity in the carbonyl range relative to the CH_2 peak around 2915 cm^{-1}.[44-46]

5.2.4 Water Contact Angle Measurement

Water contact angles were assessed on the polyethylene material surfaces with a CAM 100 contact angle goniometer (KSV Instruments) to evaluate the hydrophilicity. For each sample, contact angles were measured for at least five water droplets, with multiple samples of the same type tested to establish error bars for the data.

5.2.5 Raman Spectroscopy

The Raman spectra were acquired using a Leica optical microscopy-equipped Renishaw inVia Raman spectrophotometer. This system utilizes a 785 nm laser, an 1800 lines/mm grating, a 65 micron slit, and a RenCam CCD detector. Spectra were collected in extended mode (200 – 3800 cm^{-1}). Raman spectroscopy was employed to analyze the photodegradation of both HDPE and

LLDPE samples following UV exposure. Raman spectra offer valuable microscopic structural details regarding chemicrystallization during the degradation process.

5.2.6 Grazing Incident X-ray Diffraction (GIXRD)

GIXRD results were obtained using a Rigaku Ultima IV diffractometer operating in grazing incident mode. The diffractometer featured a 2.2 kW Cu K-alpha radiation long-fine focus tube with a 0.4 x 12 mm focus size, a goniometer with a 285 mm radius and a minimum step size of 0.0001°, and a D/teX-ULTRA scintillation detector. Prior to data collection, calibration procedures were conducted. GIXRD is a surface-sensitive crystallinity characterization technique with a detection depth in the magnitude of nanometers, providing complementary insights to Raman spectroscopy.

5.2.7 Nanoindentation Tests

Nanoindentation is considered a powerful method to measure the mechanical properties of polymer materials.[47-49] Here, nanoindentation tests were conducted using the Hysitron TI 950 TriboIndenter (Bruker, Eden Prairie, MN) with an optical camera for viewing the surface structures in high-resolution and defining areas to be indented. Tests were controlled by TriboScan9 software. A Berkovich indentation probe with a triangular base was used for depth-sensing indentation (lift height 25 nm). Before nanoindentation experiments, samples were glued onto circular AFM specimen discs (Ted Pella Inc., Redding, CA) and mounted on the intender stage which transfers samples back and forth between optics and probes. The device was calibrated before indentation experiments to ensure the probe was at the desired location during the tests. The experiments were performed in ambient conditions. Each sample was indented 18 times in different locations by setting up two 3 × 3 grids using array pattern with a load range of 0-100 μN. The reduced elastic

modulus was obtained from each indentation process, and Young's modulus can be deduced by the Oliver and Pharr method.[50] Parameters needed for calculations were obtained from previous literature.[51-53]

5.2.8 Statistical Approach

Statistical analysis using JMP software was applied to analyze how the carbonyl index is influenced by experimental variables. To quantify the factor impact, we developed linear models between the four input factors (PE grade, UV aging duration, water column (depth) and lake deployment time) and the key output variable carbonyl index (CI). In the collected data, CI values were calculated from repeated measurements on the same polyethylene sample where repeated measurements were taken on different spots of a sample. The total variation of the CI is the sum of two components: between sample variation and within sample variation. The variation of the repeated measurements within the sample includes the random within sample variation and random measurement noise. Between sample variation can be further partitioned into two parts: 1). between sample non-random variation determined by the input factors and 2). between sample random variation caused by nuisance variables in the experimental process.

One way to model this data is to consider the average CI of the repeated measures within sample as a response variable where the within sample variation is ignored. This approach works well when sample variation is small and negligible. However, preliminary data analysis (**Figure 5.3**) shows that some PE grades have large within sample variations (e.g., J and L PE grades). An alternative way is to estimate the within sample variation and between sample variation separately using a linear mixed modeling (LMM) approach.[54] The LMM we adopted is described below:

$$y = \mu + X\beta + u + \varepsilon$$

Where y is the output variable carbonyl index (CI); μ is the overall mean of the CI; β is the main effects and 2-way interaction effects of the input factors; X is a matrix which contains indicator columns (i.e., 0 or 1) for β; u is a random effect assumed to follow a normal distribution with mean zero and a between sample random variation component σ_u^2; ε is the random noise factor assumed to follow a normal distribution with mean zero and a within sample random variation component σ_ε^2. With LMM, we can estimate the effects of input factors with a lower risk of potential bias compared to the approach of fitting linear models using average CI. After fitting the LMM to the data, some interaction effects of the input factors are insignificant. We performed model reduction to improve model fitting based on the model selection criterion AICc[55] (i.e., smaller is better) and model hierarchy (i.e., remove insignificant higher-order effects).

5.3 Results and Discussion

5.3.1 Phase 1

5.3.1.1 ATR-FTIR

ATR-FTIR monitors the change in functional groups of polyethylene samples by simulated solar exposure. UV effects on the HDPE and LLDPE films are shown in **Figure 5.2**. The signals detected from the 3100 – 3800 cm^{-1} are assigned to the O-H stretching modes, the C=O signals are detected in the 1600 – 1800 cm^{-1} region while the peak around 910 cm^{-1} is due to the vinyl groups.

Their changes in intensity were studied as an indication of the photooxidation progression.

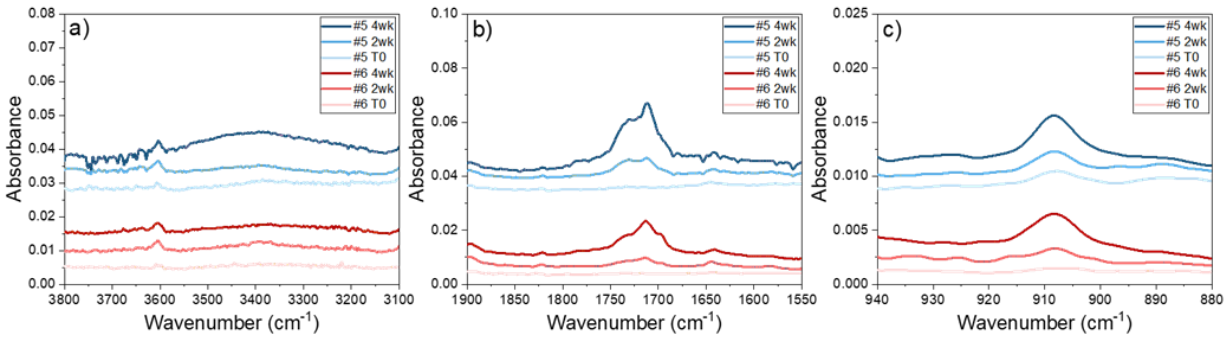


Figure 5.2 ATR-FTIR of LLDPE film #5 and HDPE film #6 in pristine condition (T0), after two and four weeks of simulated solar exposure. (a: 3100-3800 cm^{-1}, b: 1550-1900 cm^{-1}, c: 880-940 cm^{-1}).

Increases in peak intensity were observed from the three wavenumber regions in **Figure 5.2**, as a result of hydroxyl groups, carbonyl groups, and vinyl groups generated by simulated solar exposure. This result is consistent with the increasing hydrophilicity measured by water contact angles, as the amount of polar groups is increased upon UV aging. The formation of terminal vinyl groups was caused by the chain scission of its backbone.[56] In addition, both LLDPE and HDPE film samples were changed in their chemical structures as a function of time by exposure. Their changes are quantified by the carbonyl indices shown in **Figure 5.3**, where increases in the values are observed along the exposure time. Both LLDPE films and HDPE films experienced a sharp increase in carbonyl indices after two weeks (from two weeks to four weeks), indicating longer simulated solar exposure led to a greater number of groups generated. **Figure 5.3** also displays the vinyl indices of the films. Overall, the vinyl index increases after simulated solar exposure.

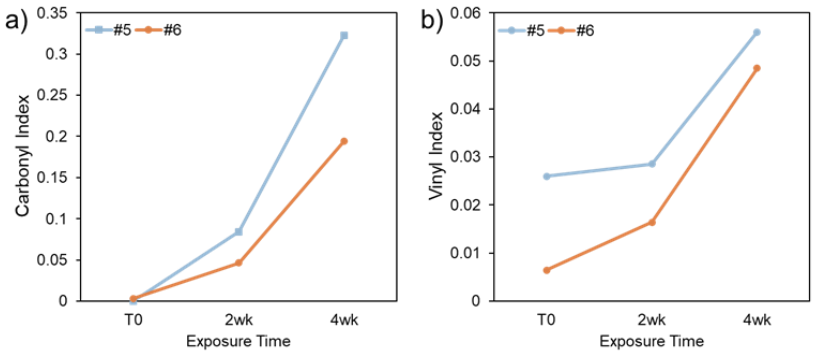


Figure 5.3 Carbonyl index (a) and vinyl index (b) of LLDPE film #5 and HDPE film #6 in pristine condition (T0), after two and four weeks of simulated solar exposure.

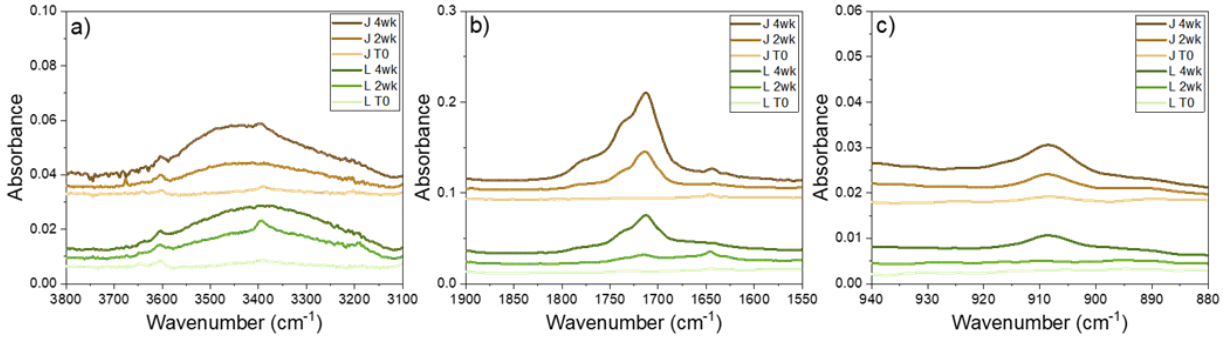


Figure 5.4 ATR-FTIR spectra of LLDPE plaques J, L in pristine condition (T0), after two and four weeks of simulated solar exposure (a: 3100-3800 cm^{-1}, b: 1550-1900 cm^{-1}, c: 880-940 cm^{-1}).

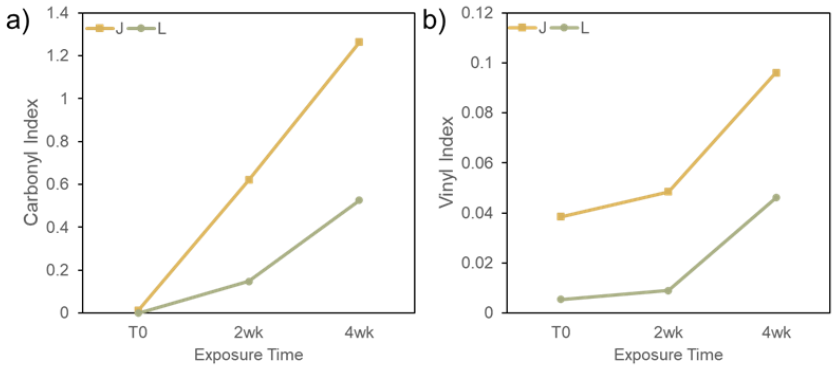


Figure 5.5 Carbonyl index (a) and vinyl index (b) of LLDPE plaques in pristine condition, after two and four weeks of simulated solar exposure.

Apart from thin films, rigid plaques were also tested after undergoing UV irradiation for different lengths of time. **Figure 5.4** depicts the results of two types of LLDPE plaques. Simulated solar exposure also changed the functional groups in them. The increase in peaks reflects that the degradation of LLDPE plaques proceeded as a function of time. The results indicate that LLDPE plaques of J with a lower density (0.9159 g/cm^3) degraded faster than those of L (0.9214 g/cm^3), which could also be seen from their carbonyl indices as shown in **Figure 5.5**. **Figure 5.5** also shows that the overall trend of the vinyl index increases after simulated solar exposure.

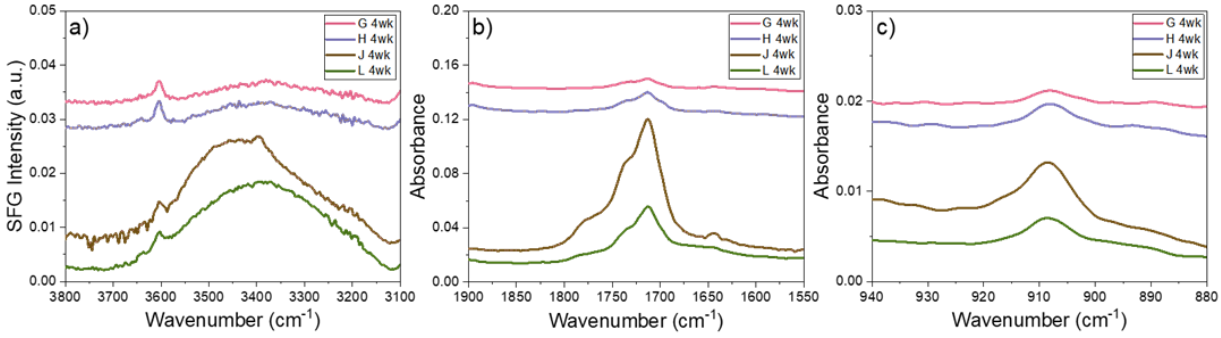


Figure 5.6 ATR-FTIR spectra of HDPE plaques G, H and LLDPE plaques J, L undergoing four weeks of simulated solar exposure (a: 3100-3800 cm^{-1}, b: 1550-1900 cm^{-1}, c: 880-940 cm^{-1}).

Figure 5.6 compares HDPE plastic plaques with LLDPE plaques undergoing four weeks of UV aging. It was found that both the LLDPE plaques exhibit stronger peaks in the three regions compared to HDPE samples. As indicators of chain scission induced by photooxidation,[56,57] the increases of carbonyl groups and vinyl groups are normalized to carbonyl index and vinyl index to evaluate the degree of chemical oxidation as listed in **Table 5.3**. LLDPE plaques J and L both show higher carbonyl indices and vinyl indices than HDPE plaques G and H. In general, LLDPE plaques show a higher degree of degradation than HDPE after being exposed to UV radiation for

the same length of time. This is because compared to HDPE, more branches in LLDPE led to polymer chains not being closely packed and a reduced degree of crystallinity. A lower crystallinity increases oxygen permeability and therefore shows an increased sensitivity to photooxidation.

	G ($0.9573\ g/cm^3$)	H ($0.9555\ g/cm^3$)	J ($0.9159\ g/cm^3$)	L ($0.9214\ g/cm^3$)
Carbonyl Index	0.135	0.145	1.252	0.526
Vinyl Index	0.018	0.016	0.058	0.041

Table 5.3 Summary of changes in carbonyl index and vinyl index for plaques after 4 weeks of simulated solar exposure.

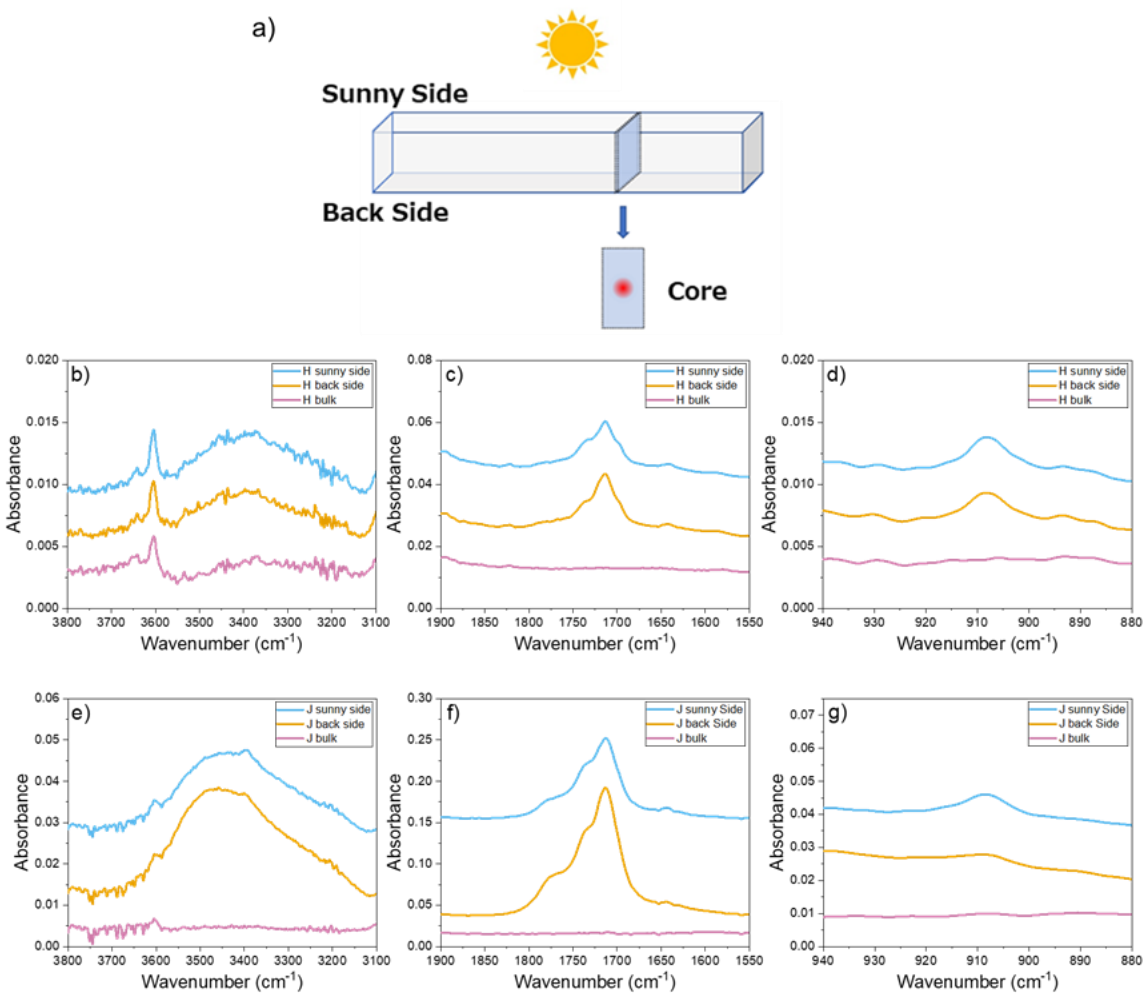


Figure 5.7 a) Schematic of different sample locations for testing. ATR-FTIR spectra of HDPE plaques H (b, c, d) and LLDPE J (e, f, g) undergoing four weeks of simulated solar exposure at different locations (b, e: 3100-3800 cm^{-1}, c, f: 1550-1900 cm^{-1} d, g: 880-940 cm^{-1}).

Furthermore, a comparison was made between different locations of plaques on ATR-FTIR (**Figure 5.7**). Sunny sides represent the side towards the UV source, while the back sides mean the one away from the light source. Based on the intensity of peaks, the core part of both LLDPE and HDPE plaque samples with a nominal thickness of 3 mm was less likely affected by UV exposure. Degradation processes are subject to diffusion-limited oxidation phenomena.[58] Oxygen present in the core part of the polyethylene samples is believed to be much less than in the surface region.

The depth and oxygen permeability of the material will be factors that lead to different oxidation results.

The back sides away from UV sources were also degraded to varying degrees, and the signals of oxidation products were even stronger than those of sunny sides. This indicates that the oxidation rate on the back sides is possibly faster than on the sunny sides. It may be due to the difference in adsorbed water amount between the two sides of the sample resulting from the UV exposure where water was sprayed onto specimens for 18 mins every 120 mins duration. The adsorbed water amount on the sunny side may be less compared to the back side, as the rate of evaporation is faster on the side of direct exposure to UV light. This will be further studied in future works.

We also performed water contact angle measurements on selected PE surfaces before and after the UV exposure. The results are presented in **Figure 5.8**, which show that the PE surfaces become more hydrophilic after the UV exposure, due to the surface photooxidation caused by UV irradiation. Such results are well correlated to the ATR-FTIR data presented above.

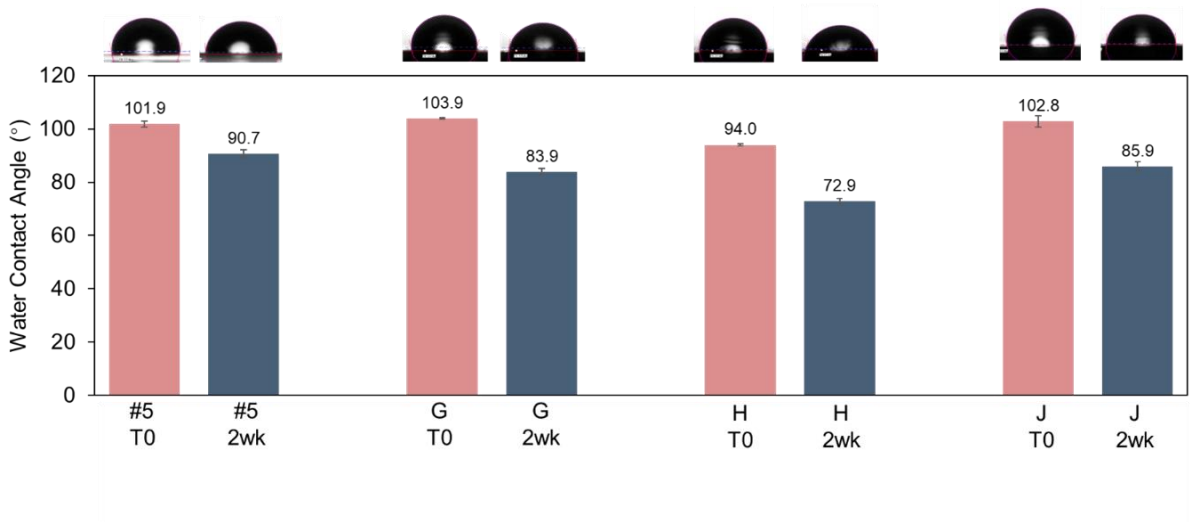


Figure 5.8 Water contact angle measurement results of PE surfaces without and with two weeks of simulated solar exposure.

5.3.1.2 Raman Spectroscopy

Before interpreting the data, Raman spectra underwent collection and processing steps. These steps involved baseline correction, standard normal variate transformation, and normalization using the intensity of the CH_2 twisting band at 1298 cm^{-1}. The peaks observed at 1080 and 1418 cm^{-1} were identified as corresponding to the C-C stretching mode of amorphous chains and the combination of CH_2 bending and wagging vibrational mode of crystalline (orthorhombic) chains, respectively.[59-63]

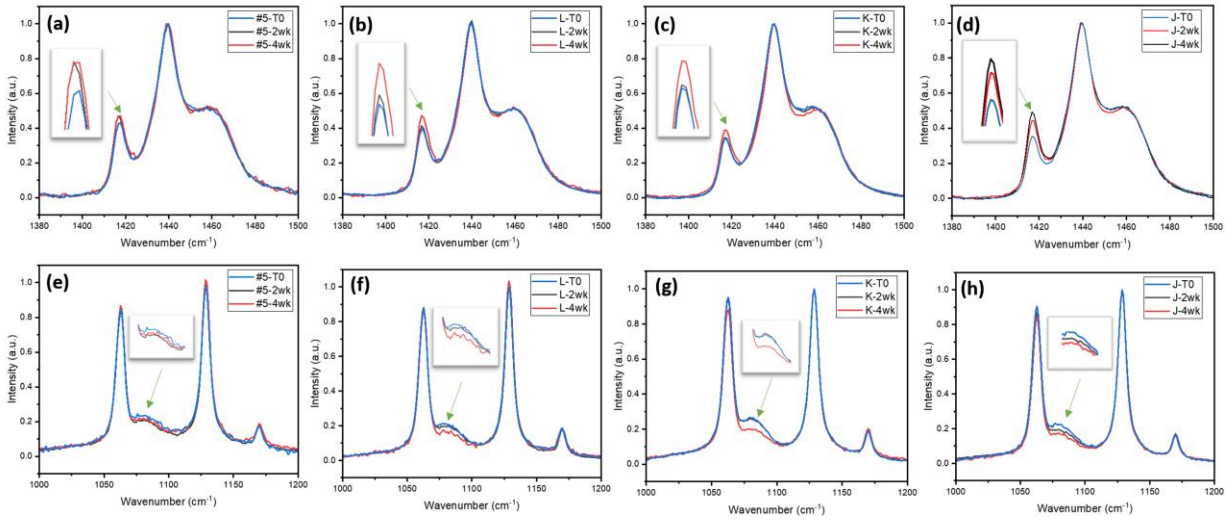


Figure 5.9 Raman results of LLDPE samples in pristine condition (T0), after two and four weeks of simulated solar exposure: a) LLDPE film #5 crystalline region, b) LLDPE plaque L crystalline region, c) LLDPE plaque K crystalline region, d) LLDPE plaque J crystalline region, e) LLDPE film #5 amorphous region, f) LLDPE plaque L amorphous region, g) LLDPE plaque K amorphous region, h) LLDPE plaque J amorphous region.

Figure 5.9 illustrates the findings of LLDPE samples in both the crystalline (a, b, c, d) and amorphous (e, f, g, h) frequency regions. The peak observed at 1418 cm^{-1} corresponds to the crystalline form of PE, demonstrating an increase in intensity from the pristine condition to two weeks and then to four weeks of UV exposure. This indicates a heightened degree of crystallinity

resulting from ongoing photooxidation. Conversely, signals around 1080 cm^{-1}, representing the amorphous region, exhibit a downward trend with increasing UV exposure time, suggesting a reduction in the amorphous region due to aging. This trend aligns well with the findings in the crystalline region.

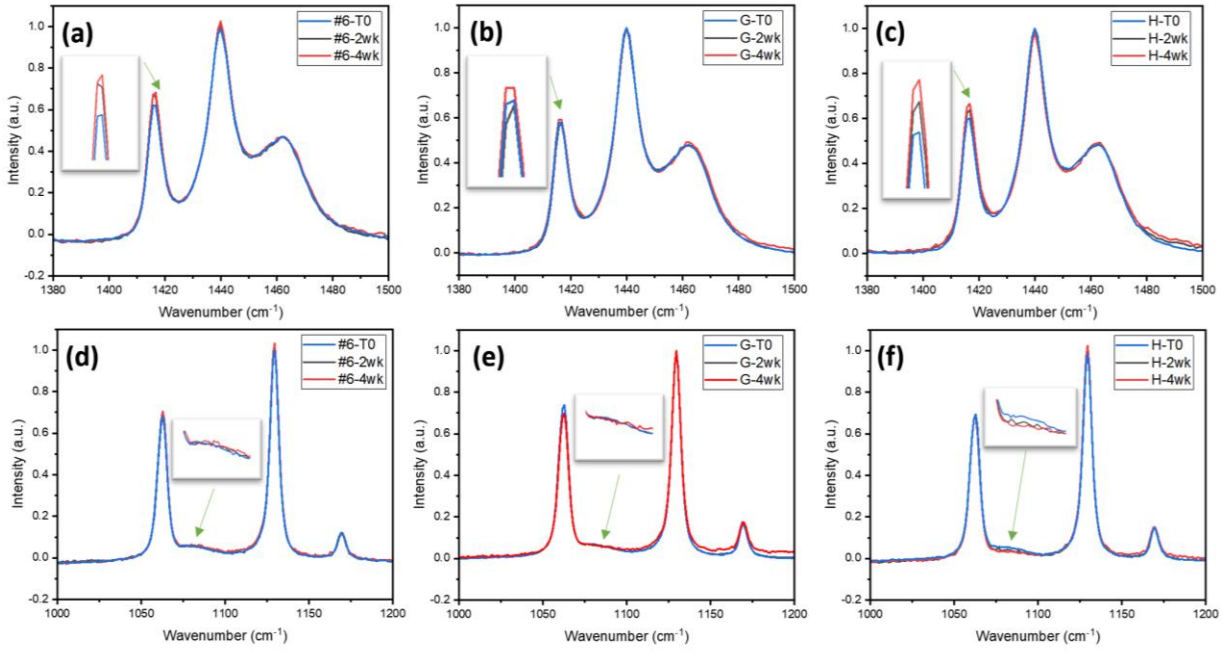


Figure 5.10 Raman results of HDPE samples in pristine condition, after two and four weeks of UV exposure: a) HDPE film #6 crystalline region, b) HDPE plaque G crystalline region, c) HDPE plaque H crystalline region, d) HDPE film #6 amorphous region, e) HDPE plaque G amorphous region, f) HDPE plaque H amorphous region.

Figure 5.10 displays the Raman spectra acquired from HDPE samples in both the crystalline and amorphous regions. The findings derived from these spectra are further consolidated in **Figure 5.11**. Remarkably, the trend of changes observed after UV exposure in the HDPE sample set mirrors that of the LLDPE samples. With prolonged UV exposure, there is a noticeable increase in the crystalline signal at 1416 cm^{-1}, coupled with a corresponding decrease in the amorphous signal at 1080 cm^{-1}.

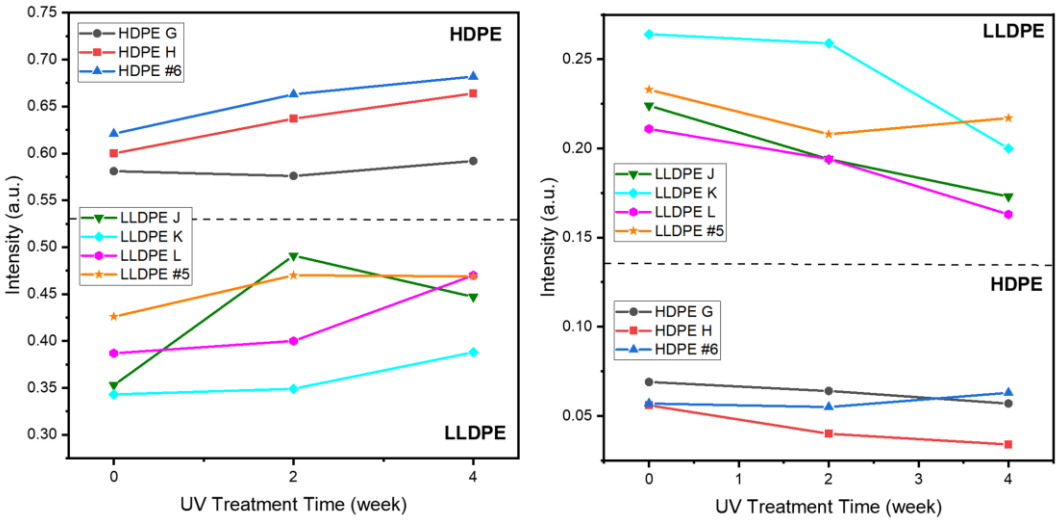


Figure 5.11 Raman intensity changes of samples as a function of the UV exposure time in the crystalline region (left) and the amorphous region (right).

Figure 5.11 provides a quantitative comparison of the Raman signal intensities measured in both the crystalline and amorphous frequency regions across various samples. Generally, the variations in Raman signal intensity in the crystalline region exhibit an opposite trend to those observed in the amorphous region across all samples. Specifically, the changes in crystallinity and amorphous regions are more pronounced in LLDPE compared to HDPE, suggesting that the amorphous domain is more susceptible to UV irradiation, consistent with findings reported by other researchers.[62]

5.3.1.3 Grazing incident X-ray diffraction (GIXRD)

In order to further confirm the extent of crystallinity influenced by UV photodegradation, Grazing Incidence X-ray Diffraction (GIXRD) was utilized to assess the changes in surface crystallinity.

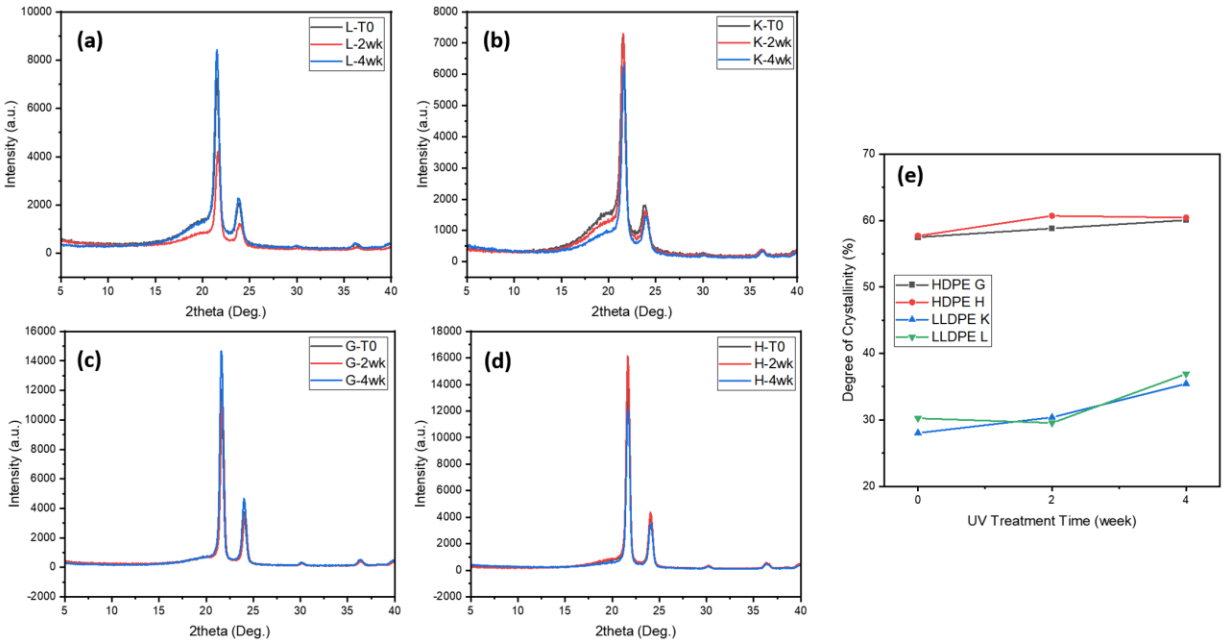


Figure 5.12 GIXRD results of samples in pristine condition, after two and four weeks of UV exposure: a) LLDPE plaque L, b) LLDPE plaque K, c) HDPE plaque G, d) HDPE plaque H, e) Summary of the crystallinity change trend observed through GIXRD analysis.

The XRD patterns were utilized to investigate the impact of different durations of UV photodegradation on various PE samples with different densities. Across all samples, the XRD results consistently revealed two sharp diffraction peaks at 21.6° and 24.5°, indicating the semicrystalline structure present in both HDPE and LLDPE samples. These peaks correspond to the (110) and (200) lattice planes of PE, respectively. Additionally, a broad band diffraction peak centered at 20.2° was observed, attributed to the signal contributed by the amorphous content of PE, which appeared stronger in LLDPE and weaker in HDPE samples. Calculation methods based on XRD results have been extensively validated by previous researchers.[64-66] The degree of crystallinity in various PE samples subjected to different UV treatments was calculated using established methods. The trend of crystallinity observed in PE samples through GIXRD analysis, as illustrated in **Figure 5.12**, mirrors the trends observed in Raman results: there is a progressive

increase in crystallinity in both LLDPE and HDPE with increasing UV treatment duration. Notably, the change in crystallinity is more pronounced in LLDPE compared to HDPE, consistent with findings from Raman analysis. This observation can be attributed to the higher amorphous content in LLDPE, rendering it more susceptible to UV-induced photodegradation reactions, including chain scission.[67] Oxygen, essential for photodegradation reactions, can readily diffuse across amorphous domains but is constrained within the more condensed crystalline domain. Consequently, polymer chains previously entangled in amorphous domains are liberated and tend to crystallize in close proximity to existing crystals.

5.3.1.4 Nanoindentation

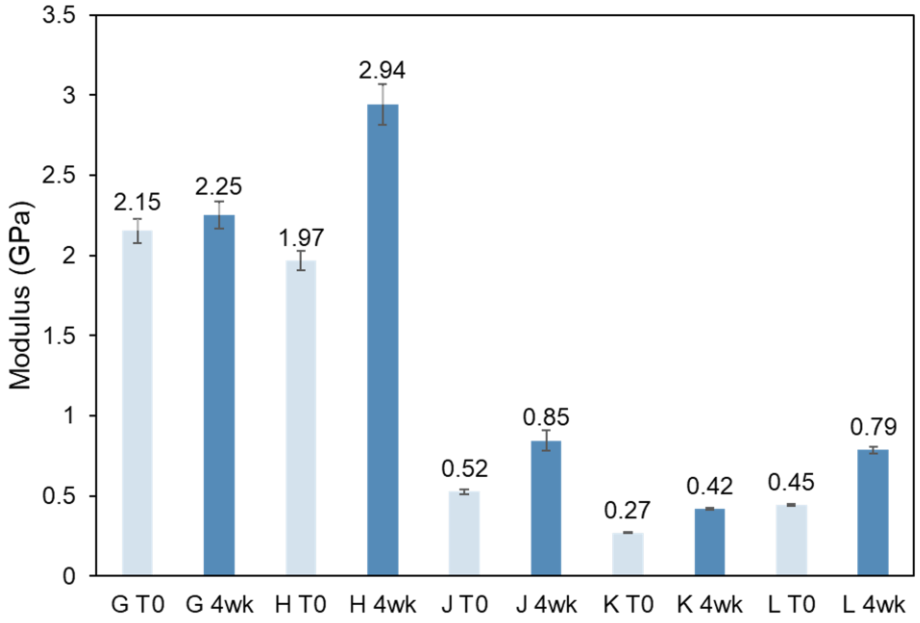


Figure 5.13 Nanoindentation results: plaques G, H, J, K, and L in pristine condition and after four weeks of simulated solar exposure.

The mechanical properties of polyethylene plaques before and after four weeks of simulated solar exposure were measured by nanoindentation tests (**Figure 5.13**). The values shown

in the figure are averaged based on 18 data sets with error bars presented. By comparing HDPE and LLDPE samples, the moduli of all HDPE plaques G and H are around 2 GPa and above, much greater than the three types of LLDPE plaques tested J, K, and L, which is likely because of the difference in their crystalline regions. Specifically, HDPE molecules with little branching are easier to pack and tend to form more crystalline regions, and therefore contributed to higher modulus values. According to our XRD results, both HDPE and LLDPE samples are dominated by the signals contributed from crystal (110) and (200) lattice planes, indicating that the crystal forms are the same for the two types of polyethylene samples while the main difference is only on the degree of crystallinity. Compared to the untreated samples, those experiencing four weeks of UV aging generally show an increasing trend in modulus, except for sample G with no significant increase. In general, the increased moduli could be explained by the increased crystallinity of polyethylene caused by UV treatment, as UV irradiation led to chain scission of polyethylene with shorter chains formed and facilitated the formation of crystalline regions. However, sample G is possibly less affected by simulated solar exposure than others likely due to its highest density. The change is subtle that it did not show an obvious increase on nanoindentation tests. This corresponds to **Figure 5.6** of ATR-FTIR data, where sample G shows the smallest change in carbonyl groups in comparison to the other three types of plaques. The trend is also similar to the trend in the Raman results regarding the change in crystallization. **Figure 5.11** shows that sample G has the least crystallinity change among all the PE plaques.

5.3.1.5 Further Discussion

As previously discussed, our study extensively examined the simulated weathering impact on different polyethylene samples utilizing a variety of analytical tools. It is worth noting that these

analytical tools possess varying surface sensitivities, potentially probing different regions of the samples. Nevertheless, despite these differences, consistent trends emerged across the various analytical techniques employed. Consequently, we aim to provide a detailed comparison of the results obtained from different analytical methods. To facilitate comprehension of the weathering effects, we will solely compare the samples at time zero and after four weeks.

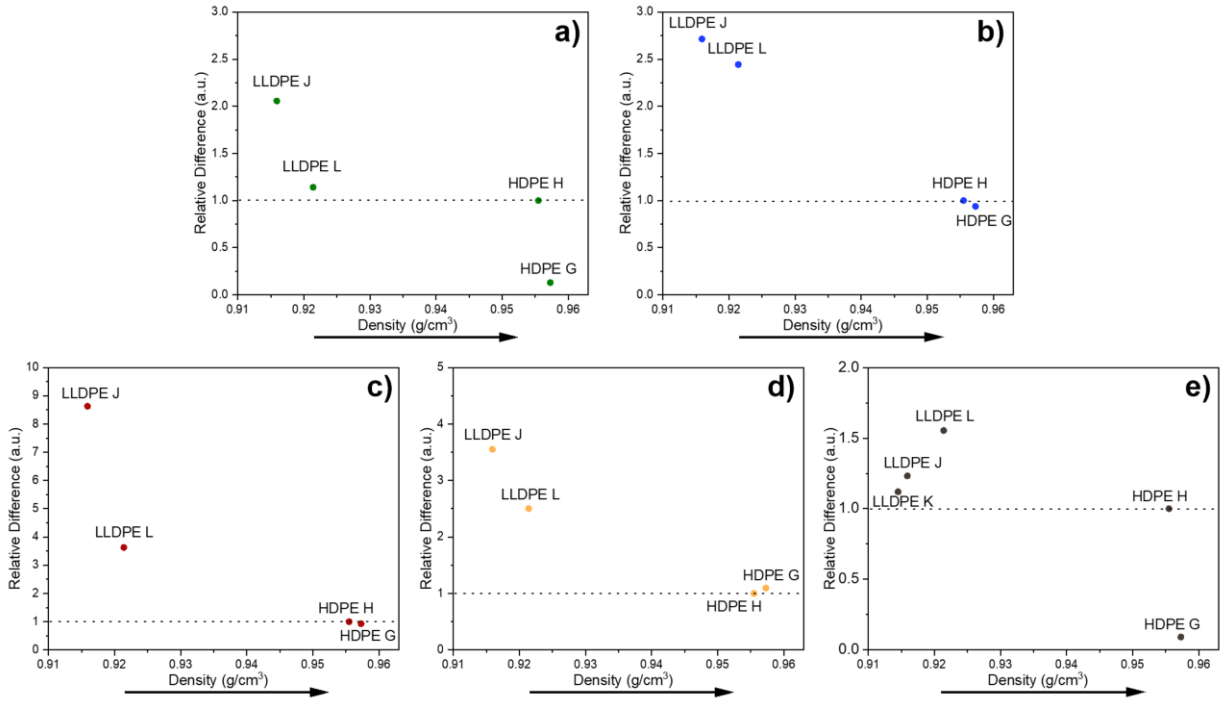


Figure 5.14 Summary of the normalized difference between 4-week aged and pristine samples: a) Raman deduced crystallinity, b) GIXRD deduced crystallinity, c) Carbonyl index, d) Vinyl index, e) Nanoindentation.

Figure 5.14 illustrates the disparities between the polyethylene samples aged for four weeks and their pristine counterparts, aiming to establish a more detailed relationship among the different techniques employed in this study to depict a more comprehensive degradation process of polyethylene. In order to better represent the relative differences across various polyethylene samples, all data were normalized using the following approach: the difference value between the 4-week aged sample H and its time zero counterpart was set as the benchmark and normalized to

1. Subsequently, the results of all other samples were calculated relative to this benchmark. It is important to note that the data normalization in **Figures 5.14a-d** was based on the difference between the 4-week aged and time zero data, whereas in **Figure 5.14e**, the difference between the 4-week data and time zero data was compared against the time zero data for each sample.

Observations from **Figure 5.14** reveal that the LLDPE samples, across all analytical techniques employed in this study, demonstrate higher difference values compared to the HDPE samples. As previously mentioned, HDPE samples have a relatively limited number of branches, whereas LLDPE samples undergo a polymerization process that introduces a greater number of branches. This difference results in a substantial decrease in density and crystallinity for LLDPE. The increased presence of tertiary carbons and higher levels of amorphous content in LLDPE contribute to higher oxygen permeability and comparatively lower stability in LLDPE. Consequently, LLDPE is more susceptible to the effects of photooxidation, as evidenced by the elevated levels of carbonyl C=O groups and vinyl C=C bonds, resulting in an increase in both the carbonyl index and vinyl index. Additionally, this phenomenon was evidenced by the increased crystallinity caused by chain scission, as observed through the increased signal from the crystalline phase in Raman scattering and the augmented crystallinity measured by GIXRD. The increase in crystallinity aligns with the increased modulus observed from the nanoindentation experiments. Notably, sample J with the lowest density exhibits the most distinct changes in **Figures 5.14a-d**. in the nanoindentation test, Sample J did not demonstrate the largest change when the parameters were relatively close. It is plausible that this nanoindentation setup may require a more extended aging period to better discern differences between LLDPE samples, or perhaps the sensitivity of the nanoindentation method is insufficient to detect microstructural changes. Additionally, it's

important to note that **Figure 5.14e** compares the modulus change ratio. When comparing the modulus change value instead of the ratio, samples J and L exhibit similar values.

Quantitatively, the effect of simulated solar exposure can be correlated to the density of polyethylene. As depicted in **Table 5.1**, the density of various PE samples follows the trend of G (0.9573) > H (0.9555) >> L (0.9214) >J (0.9159). **Figure 5.14** reflects that the Raman scattering results follow G < H < L < J. The GIXRD, carbonyl index, and vinyl index changes all suggest G ≈ H < L < J, while the nanoindentation data indicates G < H < L > J. Clearly, except for the nanoindentation result of sample J, which was discussed above, all the results suggest that the effect of simulated solar exposure on PE increases as PE density decreases. For HDPE samples G and H, similar changes in the GIXRD, carbonyl index, and vinyl index results imply that solar exposure likely leads to a similar effect on these samples. However, Raman results, which reflected both the surface and bulk changes, adhere to the established pattern: the lower the density, the greater the change. Further discussions on the PE crystallinity measured by Raman and GIXRD are presented below.

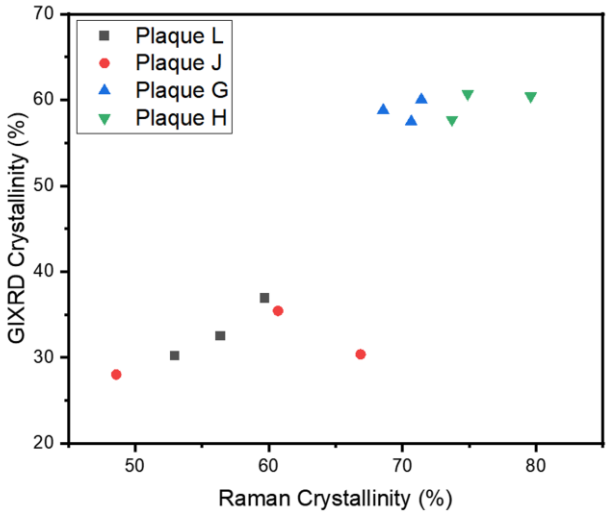


Figure 5.15 Correlations of the crystallinities measured from different samples with GIXRD and Raman spectroscopy.

Figure 5.15 illustrates the correlations between crystallinities measured using GIXRD and Raman spectroscopy for different samples. The crystallinity determination method for GIXRD data was presented above in the experimental section. A published method was utilized for determining the crystallinities from Raman spectra.[68-71] This method uses the peak intensities of the 1418 cm^{-1} peak and the twist band at around 1300 cm^{-1}.[71] **Figure 5.15** shows that the crystallinities deduced by GIXRD are lower than those determined by Raman. This is because the amorphous broad peaks overlap with the crystalline peaks, the crystalline signal is inevitably underfit leading to an underestimation of the crystallinity phase region. Furthermore, Raman and GIXRD exhibit different sensitivities in distinguishing crystallinity changes in the sample. In **Figure 5.15**, the difference in Raman crystallinity on the same set of samples is greater than that measured with GIXRD. Therefore, Raman may work as a better technique to analyze the crystallinity change by photodegradation. On the other hand, GIXRD offers superior surface sensitivity which probes the surface crystallinity. Despite these differences, the overall trend observed by both techniques is relatively similar, which indicates an increased degree of crystallinity in PE samples after a longer photodegradation treatment.

The intensity and shape of XRD signals can be influenced by both the amount of crystalline regions and the sizes of the crystals. It is plausible that the crystalline domains underwent alterations during the simulated weathering process, though this aspect falls outside the scope of the current research.

5.3.2 Phase 2

5.3.2.1 ATR-FTIR

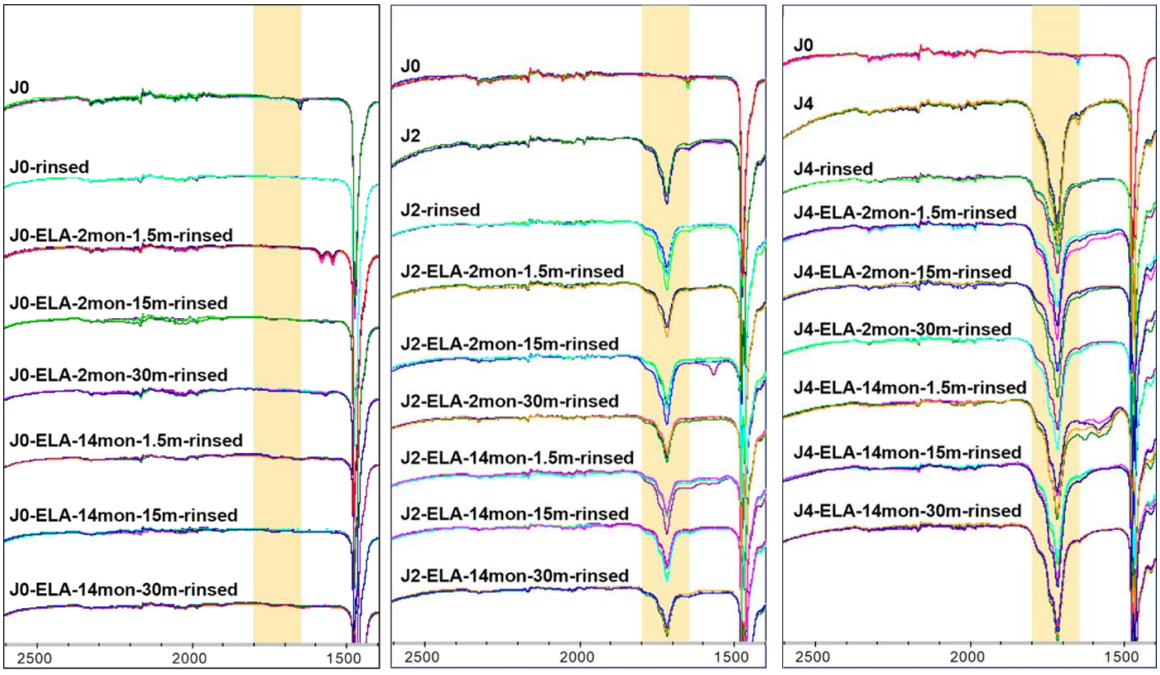


Figure 5.16 ATR-FTIR spectra of pristine LLDPE plaque J, samples after simulated solar exposure and/or lake deployment. "J0", "J2", and "J4" refer to the samples with 0, 2, and 4 weeks of simulated solar exposure. The sample names containing "rinse" refer to the samples rinsed using the rinsing method presented above. "ELA-2mon" and "ELA-14mon" refer to the samples with 2 and 14 months of lake deployment, respectively. "1.5m", "15m", and "30m" refer to the sample lake deployment depth for 1.5, 15, and 30 meters from the water surface respectively. The peaks centered at 1713 cm^{-1} (marked in the shaded orange area) are carbonyl C=O stretching signals.

ATR-FTIR monitors the change in functional groups of polyethylene samples. Emphasis is laid on the changes in the carbonyl C=O stretching wavenumber regions around 1713 cm^{-1} (highlighted) in response to the treatments. Earlier in this chapter, the polyethylene changes were studied after UV aging. We have studied such changes using a variety of analytical techniques including ATR-FTIR. It was found that the PE samples showed apparent increases in carbonyl groups upon UV aging for 2 and 4 weeks, indicating that polyethylene molecular chains underwent photooxidation. The extent of photooxidation was related to PE density. Plaque J, the LLDPE sample with the lowest density among all, showed the most noticeable change in carbonyl intensity

after UV aging. Unlike crystalline domains, amorphous regions in PE sample are more prone to photooxidation due to feasible oxygen permeability. Hence, the HDPE plaque G showed the least degree of photooxidation after 4 weeks of UV aging, while the increase in carbonyl signal intensity from 0 to 4 weeks could still be distinguished. It was also found that the PE crystallinity and mechanical properties changed accordingly as measured using Raman scattering, grazing incidence X-ray analysis, and nano-indentation.

Figure 5.16 shows the ATR-FTIR spectra of sample J as an example (without and with simulated solar exposure or UV aging for two and four weeks) deployed in the lake for different times (2 and 14 months) at different depths (1.5, 15, 30 meters from the water surface). A preliminary investigation was conducted on samples with and without rinse. The rinsing process was found to effectively remove biofilms, and importantly do not introduce any noticeable impact on the IR spectra. ATR-FTIR results of other samples with the same treatments are shown in **Figure 5.17**. From these spectra, it is apparent that the carbonyl C=O stretching signal increased for each sample after UV aging before the lake deployments, as reported previously. On the other hand, from these spectra, it can be seen that the effects of in situ lake exposure time and water columns are not as clearly reflected in the spectra as those of the UV aging. The difference between samples deployed in the lake for 2 months and 14 months is not significant, and from the spectra, change was minimal when samples were deployed at the three depths for the same duration. In order to better evaluate the results, the carbonyl index calculated based on ATR-FTIR results was applied as an indicator to quantify the change. The way to calculate the carbonyl index was described in the experimental section above.

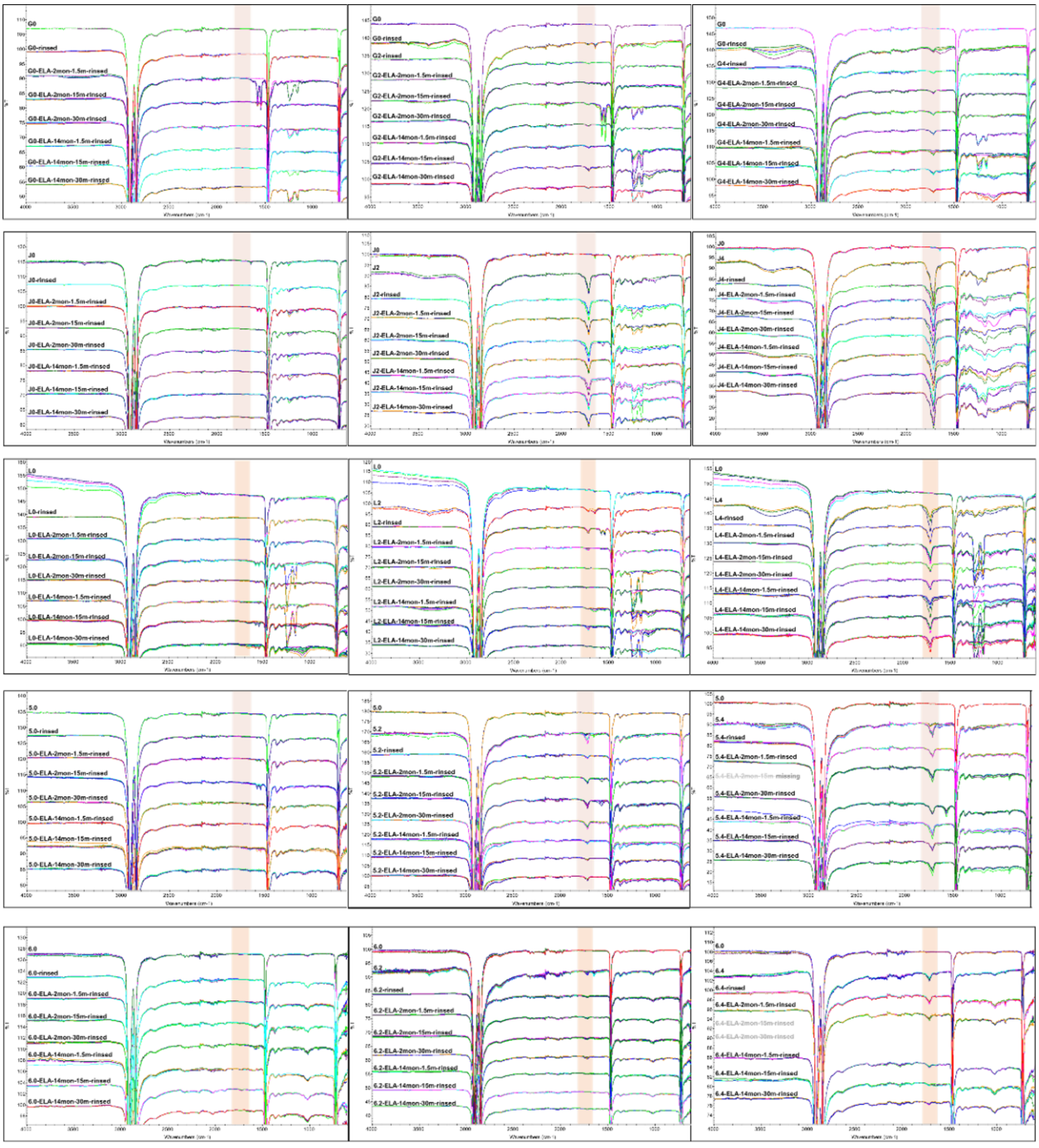


Figure 5.17 ATR-FTIR spectra of all pristine samples, samples after simulated solar exposure, lake deployment, or both.

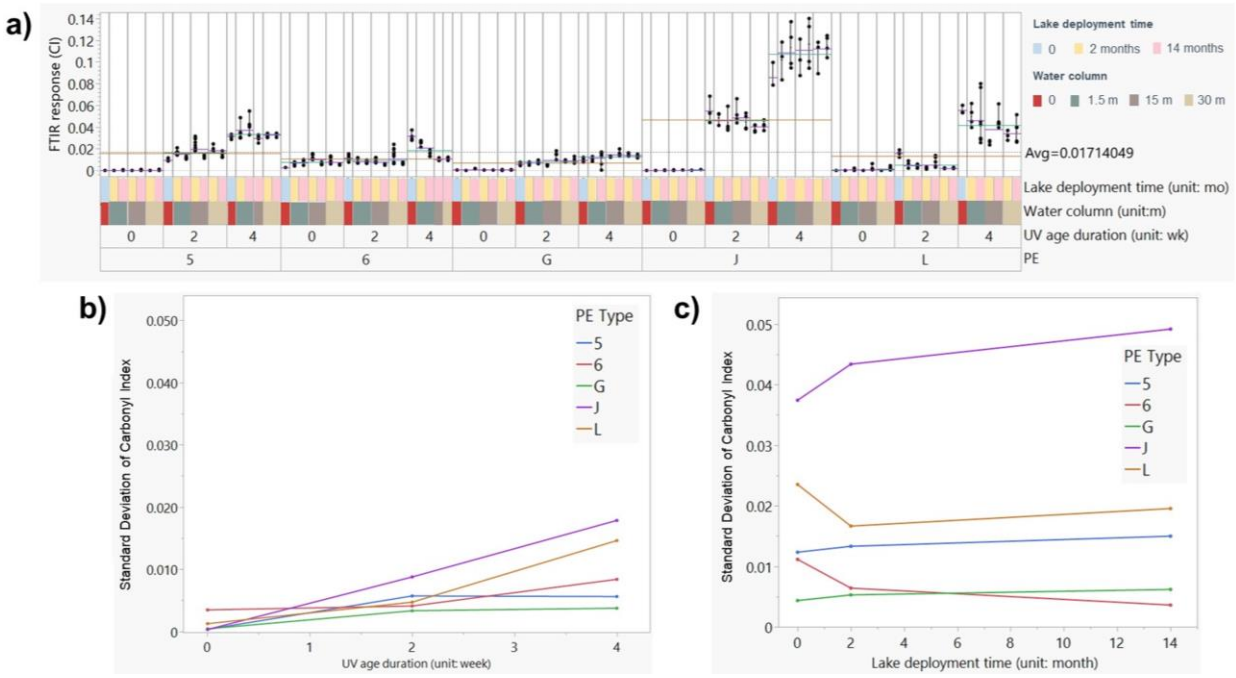


Figure 5.18 a) Summary of calculated carbonyl indices (CI) based on samples before and after different treatments. b) Plot of standard deviation of carbonyl indices for samples under different UV aging conditions. c) Plot of standard deviation of carbonyl indices for samples with different deployment times.

To better visualize the UV aging and lake deployment results of all the samples, we summarized the variability of the data sets based on the carbonyl indices of samples versus the experimental and sample conditions including four variables (PE type or sample name, UV aging time, lake deployment duration, and lake deployment depth), as shown in **Figure 5.18a**. The first row shows the carbonyl indices. The second, third and fourth rows present the experimental conditions for lake deployment time, depth of the sample location (water column), and UV aging duration. The fifth row presents PE types. **Figures 5.18b** and **5.18c** illustrate the standard deviations of carbonyl indices of different UV aging durations and deployment times, respectively. **Figure 5.18** shows that the PE type has a significant impact on the carbonyl index. Meanwhile, UV aging duration also contributed substantially to the carbonyl index difference. Interestingly,

little difference could be observed from the change in the water column levels or lake deployment times. Without UV pretreatment, negligible CI changes in response to water column and lake deployment duration were observed. The data visualization indicates that the polyethylene properties and the duration of simulated solar exposure are both key factors that affect the polyethylene degradation results, while the lake deployment impact is not obvious. Additionally, it is observed that the variability of most samples tends to rise with the duration of UV aging, with types J and L experiencing the most significant increase, approximately 0.015. On the other hand, during lake deployment from 0 to 14 months, the variability of PE types J and L changes less than 0.005. To further assess variable effects to CI, linear mixed model (LMM) that accounts for sample variability from repeated measurement is implemented. Details of LMM methodology were described in the statistical approach section above.

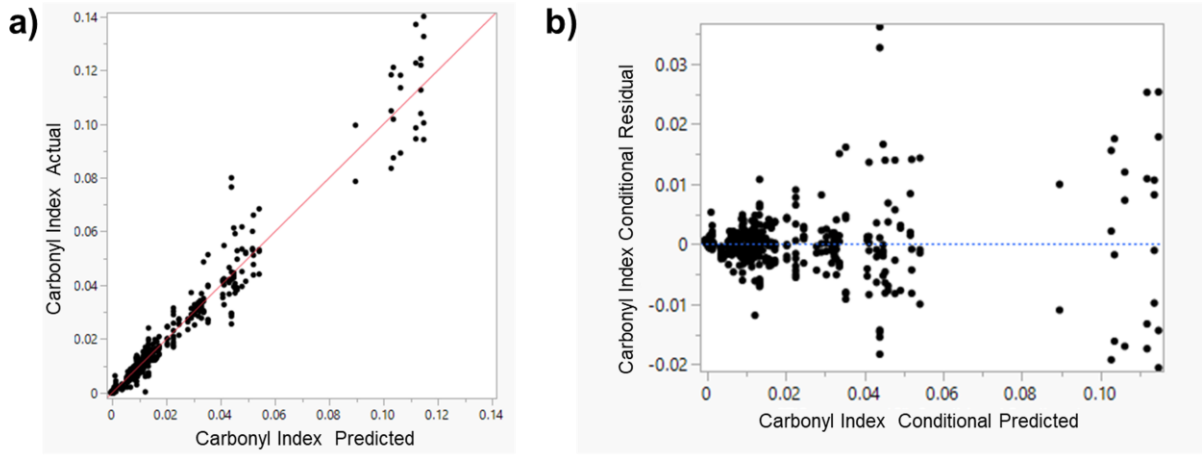


Figure 5.19 a) Linear mixed model of predicted CI (x-axis) vs. observed CI (y-axis) ; b) Conditional residual by the predicted plot.

The LMM and model residual plot are presented in **Figure 5.19**. The results show that most data points fall around the fitted line as well as a random pattern presented in the residual plot. Both of these indicate the selected LMM is a good model fit to describe the carbonyl index.

Fixed Effects Tests

Source	Nparm	DFNum	DFDen	F Ratio	Prob > F
PE	4	4	85.9	144.53335	<.0001*
UV age duration (unit: wk)(0,4)	1	1	86.6	631.17865	<.0001*
Water column (unit:m)	3	3	86.2	0.250888	0.8605
Lake deployment time (unit: mo)(0,14)	1	1	85.3	0.0262995	0.8716
PE*UV age duration (unit: wk)	4	4	86.5	116.368	<.0001*

Table 5.4 Fixed effect tests

The fixed effects tests in **Table 5.4** summarize the main effects and their interaction with p value. There are four main effects consisting of PE type (categorical), UV age duration (continuous numerical), water column (categorical), and lake deployment time (continuous numerical), and one interaction between PE type and UV age duration is included as fixed effect tests. It turns out PE type, UV age duration, and their interaction have a statistically significant ($p < 0.05$) impact on CI while water column and lake deployment duration up to 14 months are statistically insignificant. In other words, it indicates that the degradation of plastics was notably influenced by the types of PE, the duration of UV aging and their interaction, while deployment in the water column and lake environments appeared to have a less pronounced impact on degradation.

Fixed Effects Parameter Estimates

Term	Estimate	Std Error	DFDen	t Ratio	Prob>|t|
Intercept	0.0204778	0.0006856	86.9	29.87	<.0001*
PE[5]	-0.003879	0.0012967	82.4	-2.99	0.0037*
PE[6]	-0.008966	0.0013316	82.6	-6.73	<.0001*
PE[G]	-0.013256	0.0012972	89.3	-10.22	<.0001*
PE[J]	0.0306512	0.0013044	91.4	23.50	<.0001*
UV age duration (unit: wk)(0,4)	0.0202756	0.000807	86.6	25.12	<.0001*
Water column (unit:m)[0]	0.0005421	0.0015665	88.1	0.35	0.7301
Water column (unit:m)[1.5]	0.0004735	0.0011041	85.8	0.43	0.6691
Water column (unit:m)[15]	-0.000126	0.0011401	85.5	-0.11	0.9123
Lake deployment time (unit: mo)(0,14)	0.0001333	0.0008221	85.3	0.16	0.8716
PE[5]*UV age duration (unit: wk)	-0.003582	0.0016113	83.3	-2.22	0.0289*
PE[6]*UV age duration (unit: wk)	-0.014943	0.0016778	84.2	-8.91	<.0001*
PE[G]*UV age duration (unit: wk)	-0.014207	0.0015924	89.2	-8.92	<.0001*
PE[J]*UV age duration (unit: wk)	0.0327789	0.001603	91.7	20.45	<.0001*

Table 5.5 Fixed effects parameter estimates in the linear mixed model

Table 5.5 shows the fixed effects parameter estimates in the linear mixed model for carbonyl indices. The column "Estimate" is the estimate of coefficients. A larger absolute value of coefficients leads to larger effects on CI. In this table, sample L and the deployment at 30 m are used as a benchmark to help compare the relative difference among samples. For example, the estimate of the coefficient of PE[G] is -0.013256 meaning that the CI of PE type G is estimated to be 0.013256 lower than that of PE type L.

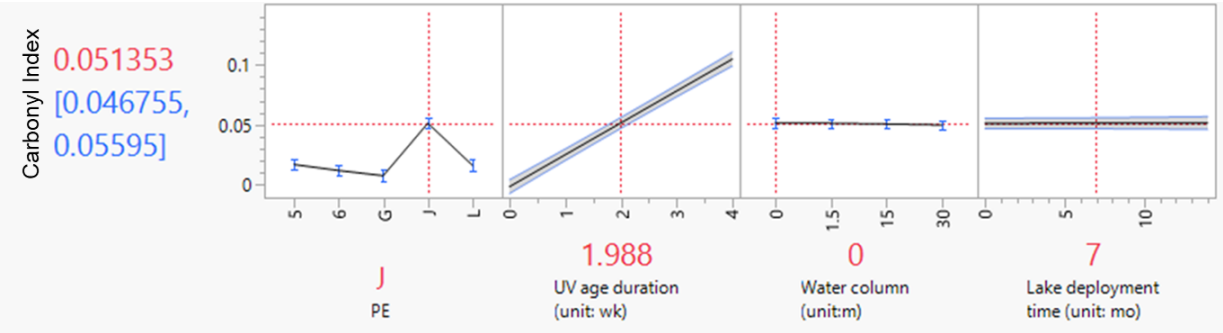


Figure 5.20 Model profiler plot when PE type is J.

Profiler in **Figure 5.20** is an interactive tool in JMP to visualize model-predicted CI trends by changing factor levels after fitting linear mixed model. Each of the plots shows how the CI changes with the four variables in X axis. As PE types and water columns are categorical factors, the error bars depicted in the figure are independent. In contrast, error bars associated with UV aging duration and lake deployment time are continuous, reflecting their continuous numerical nature. The current plot shows the predicted CI trends when the independent variables are set to PE type J, 1.988 weeks of UV age duration, 0 water column (no deployment) and 7-month lake deployment as an example. A large slope refers to a stronger effect, while a relatively flat trend means the variable is statistically insignificant. These slopes can be realized as the estimated effects described in **Table 5.5**. For example, plaque J shows a large slope in the figure of carbonyl index versus UV aging duration, meaning that the carbonyl index results of J could be greatly affected by the UV duration time. The slopes in the water column figure and lake deployment time figure are almost flat, therefore their effects are considered insignificant. This profiler plot shows that longer UV age duration will dramatically increase CI when PE type J is used. Due to the significant interaction effect between PE and UV age duration, changing PE or UV age duration in the profiler will result in a different trend compared to the plot shown here. For example, when PE type is 6 or G, the slope of UV age duration becomes flat in the profiler.

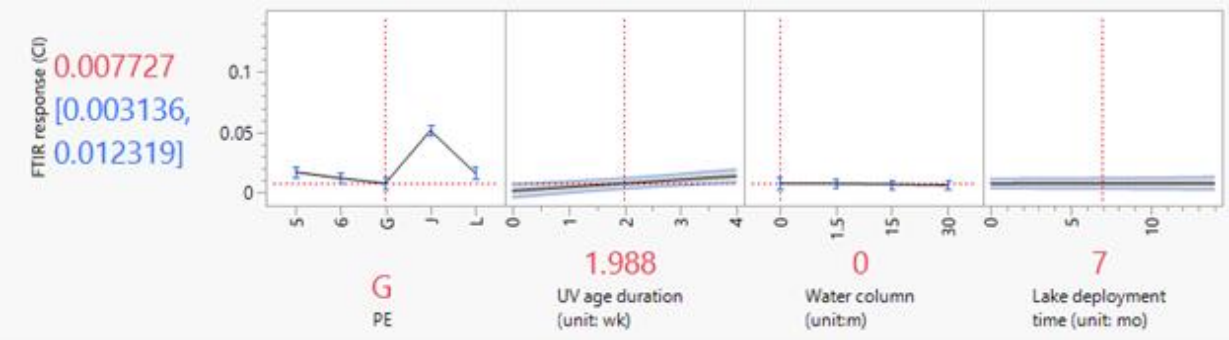


Figure 5.21 Model profiler plot when PE type is G.

Compared to the large sensitivity of plaque J, when plaque G is selected in the first panel, the slope in the second panel of carbonyl index versus UV aging duration is relatively small, as shown in **Figure 5.21**, indicating the carbonyl index of G would not be largely impacted by the UV aging duration time. Thus, the PE type affects the impact of UV aging duration on the PE carbonyl index change, which is the interaction effect. This interaction effect can also be further reflected in **Figure 5.22** below.

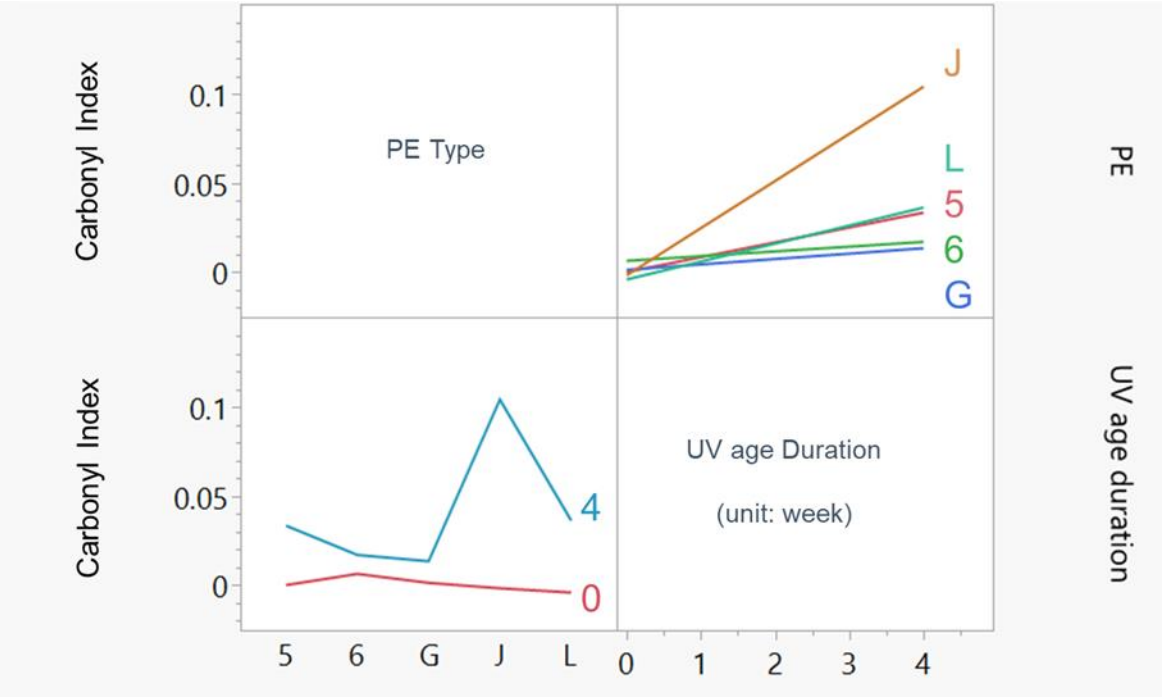


Figure 5.22 Interaction plot.

The results indicate that environmental polyethylene degradation deep in the lake on site is likely much slower than direct UV exposure. It may be due to the blocking of sunlight by the water body for the deep lake site, which inhibits the proceeding of PE photooxidation. The heat and energy from sunlight stored on the plastic surfaces, if any, will also be dissipated by lake water

during deployment. On the other hand, the biodegradation of polyethylene at the IISD Experimental Lakes Area in Canada is possibly minimal, according to our results. Overall, a longer deployment period in an environment greater than 14 months would be helpful to observe the difference, and laboratory UV aging with a much shorter treatment duration showed great impacts on polyethylene surfaces.

It is not rare to see minimal PE degradation from previous literature. For example, Arias-Villamizar et al. conducted a natural weathering study on polyethylene in not only freshwater (Magdalena River), but also in the equatorial zone of the Caribbean Sea and outdoor terrestrial settings in Colombia.[72] Our lake deployment spanned durations of 2 and 14 months, contrasting with their deployment of 180 days, equivalent to approximately 6 months. Notably, they utilized floating traps for deployment, causing plastics to predominantly reside at the water surface. In contrast, our deployment extended across depths ranging from 1.5 m to 30 m from the water surface, allowing for a more comprehensive exploration of plastic behavior across varying aquatic conditions. However, this depth range in our experiments also had the effect of obstructing sunlight from reaching the surfaces of the plastics. The results from the literature showed that the carbonyl index in both marine and river environments tended to be extremely low, even after an extended period of 180 days.[72] This pattern aligned with our findings well, where, after 2 or 14 months, detecting carbonyl peaks in samples without UV pre-aging remained challenging. However, a notable distinction emerged when comparing these outcomes with those of samples subjected to outdoor aging in dry conditions.[72] In the dry condition scenario, the carbonyl index exhibited a noticeable increase within the initial 60 days, steadily increasing to a high value by the end of the 180-day period. This suggests that outdoor-exposed samples underwent faster degradation compared to those placed in an aqueous medium. Researchers attributed this difference to

environmental variations, primarily influenced by temperature and increased exposure to UV radiation. Given that our samples were deployed in a Canadian lake at deeper depths, where temperatures and UV irradiation are expected to be lower compared to tropical regions in the literature, it is plausible that the degradation process is even slower. Thus, it is very likely that the degradation of polyethylene in the lake in our study requires a longer term of deployment.

5.4 Conclusion

In this study, individual and combined treatments of simulated solar exposure and *in situ* lake deployment were applied to study the weathering effects of a series of PE plaques and films with various parameters. The research is divided into two phases, which are sole simulated solar exposure (phase 1) and the analysis of combined treatments (phase 2).

In phase 1, various polyethylene samples subjected to simulated solar exposure were analyzed using a range of analytical methods. ATR-FTIR data indicated that samples with lower densities exhibited higher degradation rates, as evidenced by increased carbonyl and vinyl indices over time. The presence of unsaturated structures and polar groups, such as hydroxyl and carbonyl groups, also increased with exposure duration. Furthermore, variations in the degree of photooxidation from surface to core structures of plaques were observed, possibly due to differences in oxygen permeability between HDPE and LLDPE. Water contact angle measurements revealed increased hydrophilicity in both HDPE and LLDPE samples following UV exposure, suggesting the generation of more polar groups through degradation. Raman spectroscopy demonstrated an increase in crystallinity and a decrease in amorphous domains in polyethylene samples over time, indicative of susceptibility to degradation. GIXRD provided evidence of crystallinity changes at the surface, with more significant alterations observed in

LLDPE samples compared to HDPE, attributable to differences in their amorphous regions before exposure. Nanoindentation revealed a higher modulus increase rate in all LLDPE samples compared to HDPE, indicating greater embrittlement from crystalline regions due to photooxidation, though challenges are present in reflecting differences between closely related LLDPE parameters. The observed trend in mechanical results at the macroscopic level corresponded to Raman and GIXRD findings at the molecular level, indicating the progression of degradation on the polyethylene surfaces. Overall, the research of phase 1 demonstrates that the combined analytical techniques facilitated a more comprehensive depiction and comparison of degradation behaviors across different polyethylene materials, providing valuable perspectives for future manufacturing and development endeavors.

In phase 2, samples were treated using a combination of simulated solar exposure and in situ freshwater lake deployment. PE type, UV aging duration, lake deployment time, and water columns are four primary factors of interest to investigate their individual and interaction effects on PE degradation. ATR-FTIR monitored the intensity change of carbonyl groups, and carbonyl indices were calculated to quantify the results, followed by statistical analysis which enabled correlations between different variables. The results indicate that PE type, UV aging duration, and their interactions are key factors that led to the change in carbonyl indices, while water columns (depths at 1.5 m, 15 m, and 30 m) and lake deployment time ($\leqslant$ 14 months) show insignificant effects. Therefore, compared to a 14-month-long in situ lake exposure, exposure to the simulated solar source in the short term without the block of the water body, primarily through photooxidation, is more effective in weathering polyethylene. It is expected that more obvious PE degradation in the environment may be observed if the lake deployment duration is extended.

5.5 References

1. Lestari, P.; Trihadiningrum, Y.; Warmadewanthi, I. Simulated degradation of low-density polyethylene and polypropylene due to ultraviolet radiation and water velocity in the aquatic environment. *Journal of Environmental Chemical Engineering* **2022,** 10 (3),
2. Skariyachan, S.; Patil, A. A.; Shankar, A.; Manjunath, M.; Bachappanavar, N.; Kiran, S. Enhanced polymer degradation of polyethylene and polypropylene by novel thermophilic consortia of Brevibacillus sps. and Aneurinibacillus sp. screened from waste management landfills and sewage treatment plants. *Polym. Degrad. Stab.* **2018,** 149, 52-68.
3. Heimowska, A. Environmental Degradation of Oxo-Biodegradable Polyethylene Bags. *Water* **2023,** 15 (23),
4. Zbyszewski, M.; Corcoran, P. L. Distribution and Degradation of Fresh Water Plastic Particles Along the Beaches of Lake Huron, Canada. *Water, Air, & Soil Pollution* **2011,** 220 (1-4), 365-372.
5. Gauthier, E.; Nikolić, M.; Truss, R.; Laycock, B.; Halley, P. Effect of soil environment on the photo-degradation of polyethylene films. *J. Appl. Polym. Sci.* **2015,** 132 (39),
6. Martínez-Romo, A.; Mota, R. G.; Bernal, J. S.; Reyes, C. F.; Candelas, I. R. In *Effect of ultraviolet radiation in the photo-oxidation of High Density Polyethylene and Biodegradable Polyethylene films*, Journal of Physics: Conference Series, 2015; IOP Publishing: 2015; p 012026.
7. Menzel, T.; Meides, N.; Mauel, A.; Mansfeld, U.; Kretschmer, W.; Kuhn, M.; Herzig, E. M.; Altstadt, V.; Strohriegl, P.; Senker, J.; Ruckdaschel, H. Degradation of low-density polyethylene to nanoplastic particles by accelerated weathering. *Sci. Total Environ.* **2022,** 826, 154035.
8. Rabek, J. F., *Photodegradation of polymers: physical characteristics and applications*. Springer Science & Business Media: 2012.
9. Rodriguez, A. K.; Mansoor, B.; Ayoub, G.; Colin, X.; Benzerga, A. A. Effect of UV-aging on the mechanical and fracture behavior of low density polyethylene. *Polym. Degrad. Stab.* **2020,** 180, 109185.
10. Tidjani, A. Comparison of formation of oxidation products during photo-oxidation of linear low density polyethylene under different natural and accelerated weathering conditions. *Polym. Degrad. Stab.* **2000,** 68 (3), 465-469.
11. White, J. R.; Shyichuk, A. V. Macromolecular scission and crosslinking rate changes during polyolefin photo-oxidation. *Polym. Degrad. Stab.* **2007,** 92 (7), 1161-1168.
12. Pelegrini, K.; Maraschin, T. G.; Brandalise, R. N.; Piazza, D. Study of the degradation and recyclability of polyethylene and polypropylene present in the marine environment. *J. Appl. Polym. Sci.* **2019,** 136 (48), 48215.
13. Gauthier, E.; Nikolić, M.; Truss, R.; Laycock, B.; Halley, P. Effect of soil environment on the photo‐degradation of polyethylene films. *J. Appl. Polym. Sci.* **2015,** 132 (39),
14. Geetha, R.; Torikai, A.; Nagaya, S.; Fueki, K. Photo-oxidative degradation of polyethylene: Effect of polymer characteristics on chemical changes and mechanical properties. Part 1—Quenched polyethylene. *Polym. Degrad. Stab.* **1987,** 19 (3), 279-292.
15. Martin, L. K.; Yang, C. Q. Infrared spectroscopy studies of the photooxidation of a polyethylene nonwoven fabric. *Journal of environmental polymer degradation* **1994,** 2, 153-160.

16. Bonhomme, S.; Cuer, A.; Delort, A. M.; Lemaire, J.; Sancelme, M.; Scott, G. Environmental biodegradation of polyethylene. *Polym. Degrad. Stab.* **2003,** 81 (3), 441-452.
17. Gardette, M.; Perthue, A.; Gardette, J.-L.; Janecska, T.; Földes, E.; Pukánszky, B.; Therias, S. Photo- and thermal-oxidation of polyethylene: Comparison of mechanisms and influence of unsaturation content. *Polym. Degrad. Stab.* **2013,** 98 (11), 2383-2390.
18. Therias, S.; Rapp, G.; Masson, C.; Gardette, J.-L. Limits of UV-light acceleration on the photooxidation of low-density polyethylene. *Polym. Degrad. Stab.* **2021,** 183,
19. Xingzhou, H. Wavelength sensitivity of photo-oxidation of polyethylene. *Polym. Degrad. Stab.* **1997,** 55 (2), 131-134.
20. Ghosh, S. K.; Pal, S.; Ray, S. Study of microbes having potentiality for biodegradation of plastics. *Environmental Science and Pollution Research* **2013,** 20, 4339-4355.
21. Restrepo-Flórez, J.-M.; Bassi, A.; Thompson, M. R. Microbial degradation and deterioration of polyethylene–A review. *International Biodeterioration & Biodegradation* **2014,** 88, 83-90.
22. Roy, P.; Titus, S.; Surekha, P.; Tulsi, E.; Deshmukh, C.; Rajagopal, C. Degradation of abiotically aged LDPE films containing pro-oxidant by bacterial consortium. *Polym. Degrad. Stab.* **2008,** 93 (10), 1917-1922.
23. Sanniyasi, E.; Gopal, R.; Gunasekar, D.; Raj, P., Biodegradation of low-density polyethylene (LDPE) sheet by microalga. Uronema africanum Borge Sci Rep 11 (1): 17233. 2021.
24. Sarmah, P.; Rout, J. Efficient biodegradation of low-density polyethylene by cyanobacteria isolated from submerged polyethylene surface in domestic sewage water. *Environmental Science and Pollution Research* **2018,** 25, 33508-33520.
25. Sen, S. K.; Raut, S. Microbial degradation of low density polyethylene (LDPE): A review. *Journal of Environmental Chemical Engineering* **2015,** 3 (1), 462-473.
26. Wróbel, M.; Szymańska, S.; Kowalkowski, T.; Hrynkiewicz, K. Selection of microorganisms capable of polyethylene (PE) and polypropylene (PP) degradation. *Microbiol. Res.* **2023,** 267, 127251.
27. Kim, M. Evaluation of degradability of hydroxypropylated potato starch/polyethylene blend films. *Carbohydr. Polym.* **2003,** 54 (2), 173-181.
28. Lee, B.; Pometto III, A. L.; Fratzke, A.; Bailey Jr, T. B. Biodegradation of degradable plastic polyethylene by Phanerochaete and Streptomyces species. *Applied and Environmental Microbiology* **1991,** 57 (3), 678-685.
29. Shah, A. A.; Hasan, F.; Hameed, A.; Ahmed, S. Biological degradation of plastics: a comprehensive review. *Biotechnol. Adv.* **2008,** 26 (3), 246-265.
30. Sivan, A.; Szanto, M.; Pavlov, V. Biofilm development of the polyethylene-degrading bacterium Rhodococcus ruber. *Appl. Microbiol. Biotechnol.* **2006,** 72, 346-352.
31. Upreti, M.; Srivastava, R. A potential Aspergillus species for biodegradation of polymeric materials. *Current science* **2003,** 84 (11), 1399-1402.
32. Aboulkas, A.; El Bouadili, A. Thermal degradation behaviors of polyethylene and polypropylene. Part I: Pyrolysis kinetics and mechanisms. *Energy Convers. Manage.* **2010,** 51 (7), 1363-1369.
33. Arnett, R. L.; Stacy, C. J. Kinetics of the thermal degradation of linear polyethylene. *Polymer Engineering & Science* **1966,** 6 (4), 295-298.
34. Jellinek, H. Thermal degradation of polystyrene and polyethylene. Part III. *Journal of Polymer Science* **1949,** 4 (1), 13-36.

35. Murata, K.; Sato, K.; Sakata, Y. Effect of pressure on thermal degradation of polyethylene. *J. Anal. Appl. Pyrolysis* **2004,** 71 (2), 569-589.
36. Ranzi, E.; Dente, M.; Faravelli, T.; Bozzano, G.; Fabini, S.; Nava, R.; Cozzani, V.; Tognotti, L. Kinetic modeling of polyethylene and polypropylene thermal degradation. *J. Anal. Appl. Pyrolysis* **1997,** 40, 305-319.
37. Zong, R.; Wang, Z.; Liu, N.; Hu, Y.; Liao, G. Thermal degradation kinetics of polyethylene and silane‐crosslinked polyethylene. *J. Appl. Polym. Sci.* **2005,** 98 (3), 1172-1179.
38. Lomakin, S.; Rogovina, S.; Grachev, A.; Prut, E.; Alexanyan, C. V. Thermal degradation of biodegradable blends of polyethylene with cellulose and ethylcellulose. *Thermochim. Acta* **2011,** 521 (1-2), 66-73.
39. Hakkarainen, M.; Albertsson, A.-C. Environmental degradation of polyethylene. *Long term properties of polyolefins* **2004**, 177-200.
40. Biber, N. F.; Foggo, A.; Thompson, R. C. Characterising the deterioration of different plastics in air and seawater. *Marine pollution bulletin* **2019,** 141, 595-602.
41. Elkori, R.; Lamarti, A.; Salmi, H.; Hachim, A.; El had, K. Degradation of high density polyethylene packaging by accelerated aging in sea water. *Polymer Engineering & Science* **2023,** 63 (7), 2241-2250.
42. Ma, Y.; Wu, S.; Xu, Y.; Zhou, X.; Ruan, A. Degradation characteristics of polyethylene film by microorganisms from lake sediments. *Environ. Pollut.* **2023,** 333, 122115.
43. Sudhakar, M.; Trishul, A.; Doble, M.; Kumar, K. S.; Jahan, S. S.; Inbakandan, D.; Viduthalai, R.; Umadevi, V.; Murthy, P. S.; Venkatesan, R. Biofouling and biodegradation of polyolefins in ocean waters. *Polym. Degrad. Stab.* **2007,** 92 (9), 1743-1752.
44. Çavdar, A. D.; Tomak, E. D.; Torun, S. B.; Arpaci, S. S. Accelerated weathering resistance of high-density polyethylene composites reinforced with microcrystalline cellulose and fire retardants. *Journal of Building Engineering* **2021,** 39, 102282.
45. Forsgren, L.; Noyan, E. C. B.; Vega, A.; Yarahmadi, N.; Boldizar, A. The thermo-oxidative durability of polyethylene reinforced with wood-based fibres. *Polym. Degrad. Stab.* **2020,** 181, 109374.
46. Sönmez, H. E.; Bodur, M. S.; Baysan, A. A.; Bakkal, M.; Serhatli, E. Photostabilizers performance on the surface analysis of green composites. *Polym. Polym. Compos.* **2021,** 29 (1), 57-64.
47. Pertin, T.; Minatchy, G.; Adoue, M.; Flory, A.; Romana, L. Investigation of nanoindentation as a fast characterization tool for polymer degradation study. *Polym. Test.* **2020,** 81, 106194.
48. Tavares, A. C.; Gulmine, J. V.; Lepienski, C. M.; Akcelrud, L. The effect of accelerated aging on the surface mechanical properties of polyethylene. *Polym. Degrad. Stab.* **2003,** 81 (2), 367-373.
49. Tranchida, D.; Piccarolo, S.; Loos, J.; Alexeev, A. Mechanical characterization of polymers on a nanometer scale through nanoindentation. A study on pile-up and viscoelasticity. *Macromolecules* **2007,** 40 (4), 1259-1267.
50. Oliver, W. C.; Pharr, G. M. An improved technique for determining hardness and elastic modulus using load and displacement sensing indentation experiments. *J. Mater. Res.* **2011,** 7 (6), 1564-1583.
51. Jee, A.-Y.; Lee, M. Comparative analysis on the nanoindentation of polymers using atomic force microscopy. *Polym. Test.* **2010,** 29 (1), 95-99.

52. Prasad, K.; Nikzad, M.; Doherty, C. M.; Sbarski, I. Predicting trends in structural and physical properties of a model polymer with embedded natural fibers: Viability of molecular dynamics studies for a bottom up design. *J. Appl. Polym. Sci.* **2019,** 136 (45), 48189.
53. Rajeshwari, P.; Dey, T. K. Novel HDPE nanocomposites containing aluminum nitride (nano) particles: Micro-structural and nano-mechanical properties correlation. *Mater. Chem. Phys.* **2017,** 190, 175-186.
54. Littell, R. C.; Milliken, G. A.; Stroup, W. W.; Wolfinger, R. D.; Schabenberger, O., SAS for mixed models. Cary, NC: SAS Institute. Inc: 2006.
55. Akaike, H. A new look at the statistical model identification. *IEEE transactions on automatic control* **1974,** 19 (6), 716-723.
56. Grause, G.; Chien, M.-F.; Inoue, C. Changes during the weathering of polyolefins. *Polym. Degrad. Stab.* **2020,** 181, 109364.
57. Bayo, J.; Rojo, D.; Olmos, S. Weathering indices of microplastics along marine and coastal sediments from the harbor of Cartagena (Spain) and its adjoining urban beach. *Mar. Pollut. Bull.* **2022,** 178, 113647.
58. Celina, M. C. Review of polymer oxidation and its relationship with materials performance and lifetime prediction. *Polym. Degrad. Stab.* **2013,** 98 (12), 2419-2429.
59. Bailey, R.; Hyde, A.; Kim, J. J.; McLeish, J. Raman studies on oriented, high modulus, polyethylene. *Spectrochimica Acta Part A: Molecular Spectroscopy* **1977,** 33 (12), 1053-1058.
60. Gall, M.; Hendra, P.; Peacock, C.; Cudby, M.; Willis, H. Laser-Raman spectrum of polyethylene: Part 1. Structure and analysis of the polymer. *Polymer* **1972,** 13 (3), 104-108.
61. Gall, M.; Hendra, P.; Peacock, O.; Cudby, M.; Willis, H. The laser-Raman spectrum of polyethylene: the assignment of the spectrum to fundamental modes of vibration. *Spectrochimica Acta Part A: Molecular Spectroscopy* **1972,** 28 (8), 1485-1496.
62. Hiejima, Y.; Kida, T.; Takeda, K.; Igarashi, T.; Nitta, K.-h. Microscopic structural changes during photodegradation of low-density polyethylene detected by Raman spectroscopy. *Polym. Degrad. Stab.* **2018,** 150, 67-72.
63. Schachtschneider, J.; Snyder, R. Vibrational analysis of the n-paraffins—II: normal co-ordinate calculations. *Spectrochim. Acta* **1963,** 19 (1), 117-168.
64. Patel, A. K.; Bajpai, R.; Keller, J. M.; Kumari, B.; Vatsal, V.; Saha, A. Structural, morphological and micromechanical studies on fly ash reinforced PMMA composites. *Microsystem Technologies* **2011,** 17 (12), 1755-1762.
65. Statton, W. Hand book of X-ray diffraction, emission, absorption and microscopy. *Chapter-21, McGraw-Hill, New York* **1967**, 21.21-21.19.
66. Wu, Q.; Chen, N.; Wang, Q. Crystallization behavior of melt-spun poly (vinyl alcohol) fibers during drawing process. *Journal of polymer research* **2010,** 17 (6), 903-909.
67. Craig, I. H.; White, J. R.; Kin, P. C. Crystallization and chemi-crystallization of recycled photo-degraded polypropylene. *Polymer* **2005,** 46 (2), 505-512.
68. Lin, W.; Cossar, M.; Dang, V.; Teh, J. The application of Raman spectroscopy to three-phase characterization of polyethylene crystallinity. *Polym. Test.* **2007,** 26 (6), 814-821.
69. Mutter, R.; Stille, W.; Strobl, G. Transition regions and surface melting in partially crystalline polyethylene: A raman spectroscopic study. *J. Polym. Sci., Part B: Polym. Phys.* **1993,** 31 (1), 99-105.
70. Rull, F.; Prieto, A. C.; Casado, J. M.; Sobron, F.; Edwards, H. G. M. Estimation of crystallinity in polyethylene by Raman spectroscopy. *Journal of Raman Spectroscopy* **1993,** 24 (8), 545-550.

71. Strobl, G. R.; Hagedorn, W. Raman spectroscopic method for determining the crystallinity of polyethylene. *Journal of Polymer Science: Polymer Physics Edition* **1978,** 16 (7), 1181-1193.
72. Arias-Villamizar, C. A.; Vázquez-Morillas, A. Degradation of conventional and oxodegradable high density polyethylene in tropical aqueous and outdoor environments. *Revista internacional de contaminación ambiental* **2018,** 34 (1), 137-147.

Chapter 6 Conclusion and Outlook

6.1 Conclusion

This thesis research presents studies on various polymer materials for industrial applications. Through the developed methodologies, fundamental mechanisms were explored at the molecular level to elucidate the phenomena for practical use.

For polymer materials applied in the field of adhesion, SFG served as a primary tool to probe buried interfaces and surfaces, investigating the molecular behaviors influencing adhesion performance in different conditions.

In Chapter 2, research was conducted to understand adhesion enhancement facilitated by the primer. The buried interface between the adhesion promoter and the potting compound was successfully examined by SFG in situ and nondestructively. A noticeable decrease in isocyanate signal from primer was detected, suggesting the possibility of an interfacial reaction occurring during the adhesion process. Following this observation, a series of SFG experiments were designed to exclude other potential factors that could contribute to this interfacial change. Furthermore, the functional groups from the potting compound that can react with isocyanate groups were identified. Subsequently, the presence of urea groups, which are the product of the reaction, was observed at the interface after curing, further providing evidence of interfacial bonding. The results were correlated with the mechanical testing findings to establish a connection between interfacial molecular behavior and macroscopic adhesion performance. The results

indicate that the enhancement of adhesion was driven by interfacial chemical bonding. Based on that, future formulation efforts can leverage this understanding of interfacial bonding to explore avenues for enhancing overall adhesion performance. Furthermore, this study marks the first observation of chemical reactions in situ non-destructively at the buried solid/solid interface of the isocyanate family. Additionally, it presents a general approach demonstrating the potential of SFG for probing interfacial chemical reactions across various materials applications in the future.

In Chapter 3, the atmospheric moisture effect on adhesion was systematically investigated based on diminished adhesion efficiency after prolonged exposure of the primer surface to air by SFG analysis. Given the significance of isocyanate groups in facilitating interfacial bonding and adhesion enhancement, the change in these groups was monitored across various environmental conditions. The results indicate that higher relative humidity levels and longer exposure times resulted in the consumption of isocyanate groups. Subsequent SFG studies focused on the C=O and N-H regions to verify the reaction between isocyanate groups and moisture at the primer surface. Due to the complexity of primer composition, a model compound is examined under similar conditions to assess comparative trends. Mechanical tests are employed to validate the influence of moisture on adhesion, with results aligning closely with molecular-level investigations. This study represents the first utilization of SFG to explore the isocyanate hydrolysis reaction on surfaces and examine its impact on adhesion strength under atmospheric conditions. It demonstrates the capability of SFG to discern subtle changes at the surface of coatings induced by environmental factors, suggesting its utility in exploring a broader range of material responses to environmental exposure in the future.

Chapter 4 explores the effects of saltwater immersion on a model fuel tank sealant and adhesion promoter system using SFG. This investigation mimics real-world exposure to fluids to

evaluate their potential negative impacts on adhesion. Various sample geometries were designed to investigate structural changes at the buried interface. The results suggest that saltwater immersion is the primary factor altering the sample over time, while elevated temperature does not notably affect interfacial molecular structures. The structural change reaches completion within the first day of immersion. Additionally, as the formulated adhesion promoter involves both amino silane and vinyl silane, an investigation was conducted to determine whether specific silanes within 6111 exerted a predominant influence at the sealant interface. The results revealed that the amino silane APTES tended to aggregate more at the interface and exhibited interaction with the sealant. The research indicates that the saltwater immersion likely caused disorder at the interface of the adhesion promoter, potentially resulting in weaker interfacial interactions with the sealant. This suggests potential implications for the effectiveness of adhesion.

For polymer materials employed in packaging applications, a combination of analytical techniques and statistical analysis were introduced to explore the degradation behaviors of materials caused by environmental weathering.

In Chapter 5, various polyethylene plaques and films underwent individual and combined treatments of simulated solar exposure and in situ freshwater lake deployment. Phase 1 involved subjecting samples to simulated solar exposure to examine changes in polyethylene structures and properties, aiming to deepen understanding of its degradation behavior. The results indicate that the increase in polar groups, hydrophilicity, crystallinity, and higher elastic modulus depends on the dynamic structural changes observed in various polyethylene samples under UV irradiation over time. In phase 2, both simulated solar exposure and in situ lake deployment are involved in treating polyethylene samples. The primary factors of interest include PE type, UV aging duration, lake deployment time, and water columns (lake depths). These factors are analyzed individually

and in interaction to study their effects on PE degradation. The chemical structural change was monitored using ATR-FTIR, and the results were quantified and analyzed using advanced statistical methods to establish relationships between different variables. The findings suggest that PE type, UV aging duration, and their interactions are significant factors influencing the change in carbonyl indices. Conversely, water columns (depths at 1.5 m, 15 m, and 30 m) and lake deployment time ($\leqslant$ 14 months) have negligible effects. In comparison to a 14-month-long in situ lake exposure, short-term exposure to the simulated solar source without the obstruction of a water body, primarily through photooxidation, proves to be more effective in weathering polyethylene. It is anticipated that extending the duration of lake deployment may result in more noticeable PE degradation in the environment.

6.2 Outlook

This thesis research introduces developed methodologies aimed at establishing a fundamental understanding of polymer materials for real-world applications. It is hoped that these approaches will inspire further investigations into a broader range of materials and preparation methods, ultimately leading to advancements in the development of future materials.

For sealing materials, the fundamental molecular information helps to understand their adhesion mechanisms at the interfaces. As covered in the preceding chapters, adhesion can be affected by various factors. For example, the use of the primer promotes the adhesion of the potting compound on the substrate, while different operation conditions may reduce the adhesion efficiency. In addition, exposure to fluids such as saltwater, as detailed in Chapter 4, can alter interfacial molecular structures, and therefore impacts the adhesion. There remain several factors to be explored to optimize adhesion performance and extend the lifespan of these materials.

Here are some potential ways to explore for future research. The primer and potting compound examined in this study are formulated products with specific component ratios. Now that the interfacial reaction is confirmed to contribute to the enhanced adhesion between isocyanate groups from primer and amino groups from potting compound, future studies can focus on adjusting the formulation to determine the optimal component ratio. This can be based on further interfacial studies aimed at increasing interfacial bonding while preserving cohesive strength. Furthermore, formulation optimization can be achieved by integrating additional types of interfacial bonding mechanisms to enhance adhesion. The success of forming these interfacial bonds can also be assessed using SFG analysis. In terms of refining procedures, exploring various surface treatment methods may offer potential ways to improve interfacial adhesion. Therefore, leveraging SFG techniques can elucidate interfacial behaviors, offering valuable insights for optimizing surface treatment conditions. In other scenarios, identical formulated products may exhibit markedly distinct adhesion outcomes on various substrates owing to variations in substrate surface structures. SFG has the capability to detect such differences via interfacial molecular interactions, and the information obtained from these observations can guide strategies to expand the application of products. To understand the changes of reactive groups on the surface, the percentage of surface coverage by functional groups induced by the environment can be determined based on parameters calculated by modeling in the future. The established model may then be utilized to predict how these changes would affect the adhesion performance.

Chapter 4 demonstrates that saltwater immersion induces changes in the interfacial molecular structure of the sealant and adhesion promoter. Future studies will extend to examining exposure to other fluids present in service environments. For instance, immersion in jet fuel presents a different chemical environment compared to saltwater due to its organic composition.

Therefore, model fuel immersion experiments will be conducted to investigate how sealant and adhesion promoter behaviors differ in such conditions. Functional adhesion tests will complement these experiments, allowing for a connection between structural understanding and adhesion performance. Moreover, the polyurethane potting compound system and thiol-epoxy system represent just two examples among the wide range of adhesives and sealants. In the future, SFG will provide valuable insights for a broader array of applications, addressing practical challenges as more complex products with diverse components are developed.

For the study of environmental degradation of packaging materials, we introduced a combination of analytical techniques and statistical analysis. However, there are still numerous aspects that can be explored using these developed methods to contribute to a more sustainable future. In Chapter 5, we primarily discussed polyethylene samples with various parameters treated by simulated solar exposure and in situ lake deployment. Environmental degradation encompasses not only photooxidation but also microbial activities and other factors. Therefore, further investigations can expand to different waterways (freshwater vs. seawater) and biodegradation using a variety of microorganism species. For instance, analysis can be conducted on samples pre-incubated with microbes and then deployed in lakes to compare degradation behaviors with those observed in this study. Meanwhile, in addition to polyethylene as a primary packaging plastic, other commonly used plastic types for packaging could be investigated. By comparing degradation results and considering factors such as cost and manufacturing time, the selection of material species for recycling could be optimized.

Also, alternative material options for further degradation studies could include modified polyethylene (e.g., blended with thermoplastic starch) or biodegradable polymers as substitutes (e.g., polylactic acid, PLA). This expanded scope may provide a better understanding of

degradation comparisons and contribute to informed decisions regarding material selection for sustainable packaging solutions.

Furthermore, exploring the impact of additives on degradation can be another research direction. Investigating how different pigments or antioxidants influence the degradation process can provide valuable insights into material stability and potential environmental impact. Additionally, the influence of geographic regions on degradation outcomes can be further studied. For instance, deploying samples in tropical areas with different light conditions and microbial communities may yield varied results compared to samples deployed in higher latitude regions like North America. Understanding these geographical influences can contribute to a more comprehensive understanding of plastic degradation mechanisms in diverse environmental contexts.